Vibration analysis in machining of thin-walled workpieces using Hilbert-Huang Transform

（Hilbert-Huang Transformによる薄肉加工物の機械加工における振動の解析）

This dissertation is submitted in partial fulfillment of the requirements for the
Doctor of Engineering degree at Department of Mechanical Systems Engineering,
Graduate School of Engineering, Hiroshima University, Japan.

by

Agus Susanto

Thesis Supervisor: Professor Dr. Eng. Keiji Yamada

March 2019

ABSTRACT OF DISSERTATION

Agus Susanto

Vibration analysis in machining of thin-walled workpieces using Hilbert-Huang Transform

（Hilbert-Huang Transformによる薄肉加工物の機械加工における振動の解析）

Thin-walled mechanical parts are widely used in industries in order to develop the light-weight structure of machine such as turbine blade, impeller, and aerospace frame. And they are often processed by machining operation, such as turning and milling. However, machining of these mechanical parts are more challenging than rigid ones. The main reason of this is that the dynamic properties, such as stiffness and damping, are very low. Therefore, machining of thin-walled mechanical parts can induce chatter vibration, accelerate tool wear, and lead machining error easily which are major obstacles in order to achieve desired products.

In machining process, those negative phenomena are often monitored by analysis of vibration, cutting force, and temperature which are often measured by such kinds of sensors. The advanced sensors would exert their potential with an appropriate signal processing technique to extract the features of measured signals which provide an important information about machining states. Another word, signal processing is important to guarantee reliable results.

In vibration analysis, researchers use many kinds of signal processing techniques for machining process monitoring. Fast Fourier transform (FFT) is commonly used for vibration analysis in frequency domain to detect chatter and tool wear in turning and milling. Vibration analysis method in energy-time-frequency domain is also used for machining process monitoring. The time-frequency analysis (TFA) includes short time Fourier (STFT) and wavelet transforms. However, they are not suitable for analyzing of nonlinear and non-stationary vibration signals just like signal obtained in machining processes.

A recent TFA method which deals with nonlinear and non-stationary signals is Hilbert-Huang transform (HHT). HHT is applied for detecting fault in mechanical transmission, such as gear and rotating machinery. However, the use of HHT to analyze signal in turning and milling is limited. Therefore, HHT is applied in this study for machining process monitoring by means analyzing vibrations obtained in machining. In this study, machining process monitoring is including chatter detection, sudden change of machining stability caused by lubrication, sudden change of machining stability caused by obstacle in machining, and tool condition monitoring. In order to achieve the goals of this research, extensive experiments were conducted under various cutting conditions. Signals obtained in machining tests were analyzed by FFT, STFT, and HHT.

The results showed that the empirical mode decomposition (EMD) decomposed complex vibration into simple components, and each one of them contained a unique vibration mode caused in machining. EMD can sift out the signal containing chatter frequency from others. In chatter detection in milling based on HHT spectrum, the energy in stable milling was concentrated in particular frequency. Besides, the energy in unstable milling (occurring chatter) was chaotic and the frequency was not constant. And, the HHT can reveal the difference excitation among cutting edges. HHT can reveal the effect of cutting fluid on the stability of milling which was pointed out in Hilbert spectrum. In Hilbert spectrum, the energy appeared in certain frequency range for dry cutting, and energy vanished when tool entered in the wet area. Besides, the energy in Hilbert spectrum displayed a chaotic spectrum when milling was unstable caused by obstacle. And, Hilbert spectrum of the stable milling showed that the energy was distributed in particular frequency. HHT can be utilized for tool condition monitoring. Based on the Hilbert spectrum, milling using worn and chipped tools can be distinguished from milling using normal tool. FFT was not suitable for analyzing stationary vibration signal which frequency changes over cutting periode. STFT spectra gave blurry and blocked spectra because of its time-frequency resolution. Besides, HHT spectra showed a significant improvement of time-frequency resolution making the frequency components easier to be identified.

Key words: machining process monitoring, Hilbert-Huang transform, chatter vibration, sudden change of machining stability, tool condition monitoring.

SUMMARY OF DISSERTATION

Agus Susanto

Vibration analysis in machining of thin-walled workpieces using Hilbert-Huang Transform

（Hilbert-Huang Transformによる薄肉加工物の機械加工における振動の解析）

Thin-walled mechanical parts are widely used in industries in order to develop the light-weight structures of machine such as turbine blade, impeller, and aerospace frame. However, machining of these mechanical parts are more challenging than rigid ones. The main reason of this is that the dynamic properties, such as stiffness and damping, are very low. Therefore, machining of thin-walled mechanical parts can induce chatter vibration, accelerate tool wear, and lead machining error easily which are major obstacles in order to achieve desired products.

In vibration analysis, researchers use many kinds of signal processing techniques for machining process monitoring for example fast Fourier transform (FFT), short time Fourier transform (STFT) and wavelet transform. However, the disadvantages of them are the trade-off between time and frequency resolutions, i.e. the higher of frequency signal resolution, the lower of time resolution is, and vice versa. And, difficult to find fit amplitude in frequency spectrum because FTT averages the signal amplitude in its spectrum. Therefore, FFT is hammered to be applied for signal with change in amplitude. A recent TFA method which deals with nonlinear and non-stationary signals is Hilbert-Huang transform (HHT). And, HHT is applied in this study for machining process monitoring by means analyzing vibrations obtained in machining.

All signals obtained in the above machining tests were analyzed by FFT, STFT, and HHT. The results showed that FFT was not suitable for analyzing transient vibration, whose frequency changes over cutting periode. STFT spectrum provides low time and frequency resolution. Therefore, STFT presented blurry, overlapped, and disjointed blocks spectrum. Besides, EMD of HHT decomposed signal into a series of components called intrinsic mode functions (IMFs). And each IMF contains individual mode oscillation, amplitude, and frequency. The first IMF is the component with highest frequency, otherwise the last IMF is the component with lowest frequency and monotonic residue has no physical meaning because it was just residue. From IMFs, complex signal containing slight and severe chatter could be sifted out from other signals. Therefore, EMD makes it easy to recognize chatter growing as the cutting depth was increased both in turning and milling. Besides, Hilbert spectra of HHT shows a significant improvement of the frequency resolution making the frequency components easier to be identified. In Hilbert spectrum, the energy level for unstable milling (occurring chatter) was greater than stable milling. And, the energy in unstable milling was chaotic and the frequency was not constant over the cutting period. It was caused by cutting with fluctuating radial cutting depth and each cutting edge excited the vibration of the workpiece. The important note that HHT could reveal the difference excitation among cutting edges. Besides, the energy for stable milling was concentrated in certain frequency. On the other hand, the cutting fluid enhanced the attenuation of vibration in milling, which was pointed out in Hilbert spectrum. In Hilbert spectrum, the energy appeared in certain frequency for dry cutting, and energy was vanished when tool entered in wet area. In milling with obstacle, the Hilbert spectrum displayed chaotic spectrum of energy. Besides, milling using normal tool could be distinguished from milling using worn or chipped tool. When the cutting tool was getting wear, the energy of Hilbert spectrum appeared at spindle rotational frequency. When cutting tool was getting chipping, the energy appeared in spindle rotational, tooth passing, and unidentified frequencies. Besides, strain signal provided useful signal for machining process monitoring. Because strain signal worked well with HHT as shown in Hilbert spectrum

List of Contents

Chapter 6. Result and Discussion

6.1. Chatter Detection in Turning of Thin-Tubular Workpieces

6.2. Chatter Detection in Thin-Walled Milling

6.3. Sudden Change of Machining Stability caused by Lubrication

6.4. Sudden Change of Machining Stability Caused by Obstacle in Thin-walled Milling

6.5. Tool Condition Monitoring Using HHT

Appendix

List of Tables

List of Figures

Nomenclatures

English symbols

A	Amplitude of simulation signal [m/s^2]
A_a	Axial cutting depth [mm]
A_{lim}	Maximum axial depth of cut for chatter free machining [mm]
A_r	Radial cutting depth [mm]
c	Damping coefficient [N-s/m]
$c_j(t)$	j^{th} Component of IMF
f_c	Chatter frequency [Hz]
f_n	Natural frequency [Hz]
f_p	Tooth passing frequency [Hz]
f_s	Spindle rotational frequency [Hz]
f_{sam}	Sampling frequency [Hz]
F_y	Cutting force in y-direction [N]
$G_{yy}(\omega)$	Direct frequency response function (FRF) which represents the correlation between response in y-axis with excitation force in y-direction [m/N]
$\lvert G_{yy}(\omega)\rvert$	Magnitude parts of the FRF [m/N]
h	Uncut chip thickness [mm]
h_o	Controlled uncut chip thickness [mm]
h_i	Proto-IMF
$H(t)$	Hilbert transform
i	Imaginary value ($= \sqrt{-1}$)
$Im[G_{yy}(\omega)]$	Imaginary parts of FRF [m/N]
k	Spring stiffness [N/m]
K_t	Tangential milling force coefficient [N/m^2]
K_r	Radial milling force coefficient [N/m^2]
l_b	Integer number
$l(t)$	Lower envelope
m	Mass [kg]
n	Spindle rotational speed [min^{-1}]
N	Data length
N_k	Number of modes
N_t	Number of teeth
P	Tooth passing period (second)
r	Frequency ratio of ω/ω_n
r_a	Tool radius [mm]
$r_{Nk}(t)$	Monotonic residue
$r(t)$	Residue
R_a	Surface roughness (μm)
$Re[G_{yy}(\omega)]$	Real parts of FRF [m/N]
SD	Threshold value (= 0.2)
t	Time [s]

$u(t)$	Upper envelope
V_f	Feed rate [mm/min]
$x(t)$	Discrete data
y	Workpiece deflection [mm]
$\odot$	Machining under stable condition
$\times$	Machining under unstable condition

Greek symbols

$\alpha(t)$	Instantaneous amplitude [$(\mathrm{m/s}^2)^2$]
α_{yy}	Directional dynamic milling coefficient in the y direction [$\mathrm{N/m}^2$]
Δf	Frequency resolution [Hz]
ϕ_e	Exit angle [deg.]
ϕ_s	Start angle [deg.]
$\emptyset(t)$	Phase function
ω_c	Chatter frequency [rad/second]
$\omega(t)$	Instantaneous frequency [Hz]
Ω	Forcing frequency [Hz]
ψ	Phase parts of the FRF
ζ	Damping ratio

Abbreviations

EMA	Experimental modal analysis
EMD	Empirical mode decomposition
FFT	Fast Fourier transform
FRF	Frequency response function
HHT	Hilbert–Huang transform
IMF	Intrinsic mode functions
LQL	Little quantity lubrication
SDOF	Single-degree-of-freedom
SLD	Stability lobe diagram
STFT	Short-time Fourier transform
TFA	Time–frequency analysis

Chapter 1

Introduction

1.1. Background and Motivation

Thin-walled mechanical parts, for example; turbine blade, impeller, and aerospace frame as shown in **Fig. 1.1**, are extensively used in industrial and academia fields [1-3]. They are often processed by machining operation such as turning [4-6] and milling [7-9]. Thin-walled mechanical parts are usually machined from blank blocks [10,11] which allows to get high quality and precise parts in less time [12]. However, for machining thin-walled mechanical parts are more challenging than rigid ones. The main reason for this is that the dynamic properties of those mechanical parts, namely stiffness and damping, are very low. Therefore, machining thin-walled mechanical parts can induce negative effects such as chatter [4,5], tool wear [7], and machining error [8, 9] which are major obstacles to achieve desired products. Therefore, machining process monitoring is needed to make better products.

In machining thin-walled mechanical parts, those negative effects are often monitored by measurement and analysis acceleration, displacement, cutting force, and sound signals. Huang et al. [7] measured cutting forces using dynamometer and analyzed them to monitor tool wear in down-milling of thin-walled aerospace components. Feng et al. [13] measured cutting forces using dynamometer and analyzed them to detect chatter in milling of thin-walled parts and found the correlation to the surface finish. Ren et al. [14] measured the displacement signals of workpiece using displacement sensor to monitor machining states in pocket milling of the thin-walled components. Kolluru and Axinte [15] used accelerometer sensor to measure the acceleration signals of workpiece and analyzed them to monitor chatter in milling of circular thin-walled components. Shi et al. [16] measured and analyzed the sound signals using microphone to monitor chatter and evaluated the machined surface finish.

Based on those studies, they informed that the sensors were one of the key elements for machining process monitoring. The advanced sensor would exert its potential with an appropriate signal processing technique to extract the features of the measured signal which provide an important information about machining states. In other words, the signal processing is important to guarantee the reliable results of machining process monitoring.

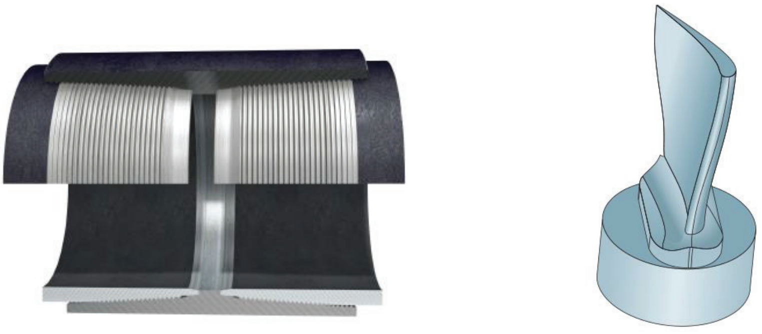

(a) Pipeline [17] (b) Turbine blade for jet engine [18]

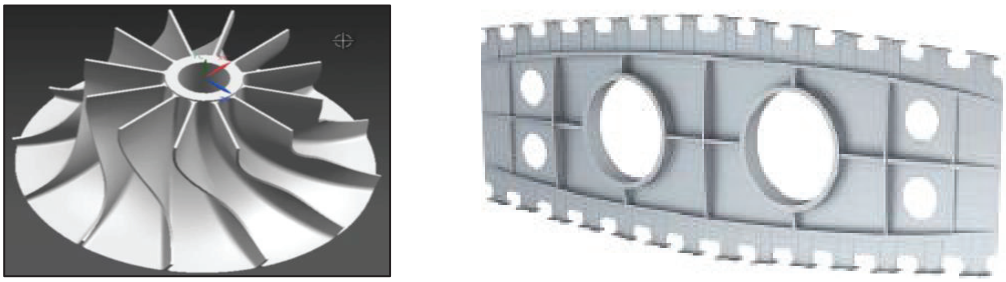

(c) Impeller for automotive engine [19] (d) Aerospace frame [20]

Fig. 1.1. Thin-walled mechanical parts; pipeline, turbine blade, impeller and aerospace frame.

The aim of this study is applying Hilbert–Huang transform (HHT) for analyzing measured signals to monitor machining states. Because the HHT is an advanced method of energy-time-frequency analysis nowadays which is specially applied for nonlinear and non-stationary signals like vibrations occurring in machining processes. And the vibration analysis is one of the easy ways to monitor machining process. Machining states are monitored to detect chatter, to analyze sudden change of machining stability caused by lubrication, to analyze sudden change of machining stability caused by obstacle in thin-walled milling, and to monitor tool condition. In this study, extensive machining tests are conducted under various machining parameters.

1.2. Organization of Dissertation

This research has been carried out in the Laboratory of Machining and Machining Systems under the supervision of Professor Keiji Yamada for machining process monitoring through vibration analysis. The dissertation is organized as follows:

- In Chapter 2, conventional spectral analysis tools, namely; fast Fourier (FFT), short-time Fourier (STFT), and wavelet transforms, are explained. Simulation signal is created to show the performance of each spectral analysis. Several types of previous researches which utilized these spectral analysis tools are also provided. Furthermore, the drawback of those spectral analysis tools is also given based on the previous researchers' findings.
- Chapter 3 describes the widespread use of HHT to detect damage of the transmission element in mechanical system and limited use of HHT in machining fields. In this chapter, HHT is also explained theoretically and simulation signal is created to explain HHT.
- In Chapter 4, the dynamic models for turning and milling are derived first. Following, stability lobe diagram (SLD) is introduced for determining cutting parameters. Here, theory of experimental modal analysis (EMA) method is also discussed briefly. EMA is needed for determining the dynamic modal parameters, such as; stiffness, and damping ratio.
- Chapter 5 explains the experimental methods of this study, including; hammering and machining tests. After hammering tests, SLDs introduced in Chapter Four are generated to determine the cutting parameters prior to machining tests; both turning and milling.
- Chapter 6 explains experimental results and discussions. The discussions are including chatter detection in turning and milling, analysis of sudden change of machining stability caused by lubrication and analysis of sudden change of machining stability caused by obstacle in thin-walled milling, and tool condition monitoring.

- In the last of this dissertation, some important conclusions are considered in Chapter 7.

Chapter 2

Conventional Signal Analysis Tools

In this chapter, conventional spectral analysis tools are explained. They are including fast Fourier (FFT), short-time Fourier (STFT), and wavelet transforms. Simulation signal is created to show the performance of each spectral analysis. The previous studies which utilized these spectral analysis tools are also provided.

2.1. Fast Fourier Transform

In machining process monitoring through vibration analysis, fast Fourier transform (FFT) is widely used to detect chatter and tool wear. Altintas et al. [21] modeled the dynamics of half immersion down-milling to get stability lobe diagram. Their model was then proved by milling tests, and measured cutting forces were analyzed by FFT. Comak and Budak [22] designed the geometry of ball end-mill for optimizing the chatter stability limit through selecting the pitch of cutting edge and the helix angle, and they experimentally verified their model through milling. Then, they employed FFT for analyzing sound signals to recognize chatter frequency. On the other hand, FFT was also utilized to analyze the acoustic emission signal for tool condition monitoring in turning by Govekar et al. [23].

FFT provides an efficient algorithm for transforming data from the time domain into the frequency domain. Typically, the time-domain data x_j to be transformed to frequency-domain consists of data length N. The discrete Fourier transform (DFT) can be commonly expressed as [24]:

$$X = \sum_{j=0}^{N-1} x_j \exp(-2\pi i \frac{j}{N} k) \qquad (2.1)$$

where $k = -{}^{N}\!/_{2}$, …, -1, 0, 1, …, ${}^{N}\!/_{2}$ and x_j represent the time-domain data.

It should be noted that the frequency resolution Δf is defined as the ratio of sampling frequency f_{sam} to the data length N, i.e. $\Delta f = f_{sam}/N = 1/T$.

To show the time and frequency resolution of FFT, we simulate the signal $x(t) = A\sin(2\times\omega_x t)$, where; A, ω_x, and t are amplitude, frequency signal, and time, respectively. After simulating that signal, FFT method is applied to analysis it. In this simulation, we are trying three trials of simulation signal $x(t)$ with different parameter input. And, we calculate computational time of the program.

For the first trial of simulation, the parameters are shown in **Table 2.1**. Based on this table, the frequency signal ω_x, amplitude A, sampling frequency f_{sam} and data length N are set 200 Hz, 1 m/s^2, 10 kHz, and 1000 points, respectively. And the simulation result is shown in **Fig. 2.1**. **Figure 2.1(a)** is full waveform of simulation signal in time-domain. As can be seen from **Fig. 2.1(a)**, the amplitude of signal is A = 1 m/s^2. On the other hand, **Fig. 2.1(b)** shows frequency spectrum obtained by FFT. As can be seen from the figure, frequency signal shows 200 Hz and the amplitude of spectrum is 1 m/s^2. In this first trial, the computational time was 0.13001 seconds.

Table 2.6. Parameter of simulation signal for first simulation.

Frequency of signal ω_x	200 Hz
Amplitude A	1 m/s^2
Sampling frequency f_{sam}	10 kHz
data length N	1000 points

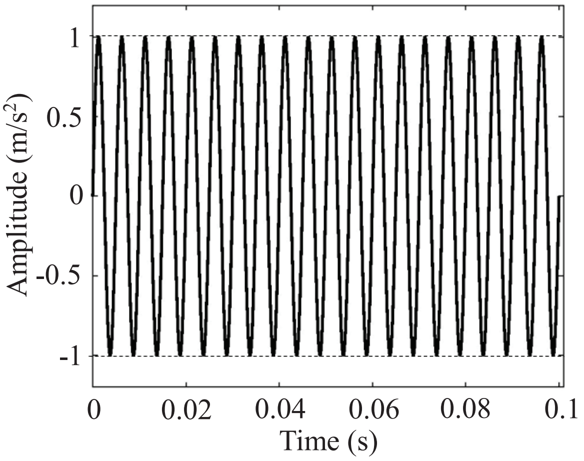

(a) Full waveform in time-domain.

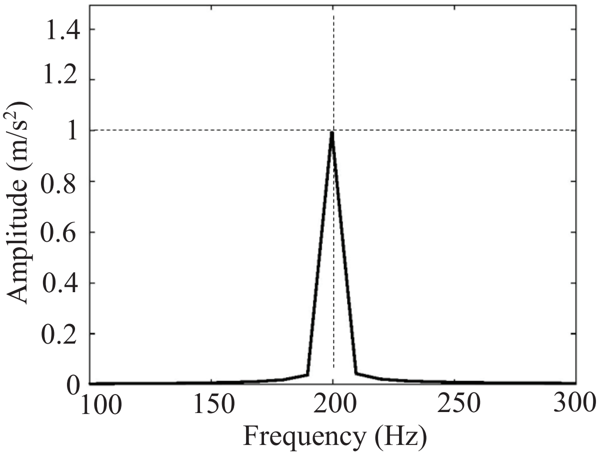

(b) Frequency spectrum obtained by FFT.

Fig. 2.1. Result of simulation signal for first trial.

Now the parameter is changed for the second trial of simulation, new parameters are shown in **Table 2.2**. Based on this table, the sampling frequency f_{sam} is decreased becoming 1 kHz (10 kHz to be 1 kHz) and other parameters are same as **Table 2.1**.

Table 2.7. Parameter of simulation signal for second simulation.

Frequency of signal ω_x	200 Hz
Amplitude A	1 m/s^2
Sampling frequency f_{sam}	1 kHz
data length N	1000 points

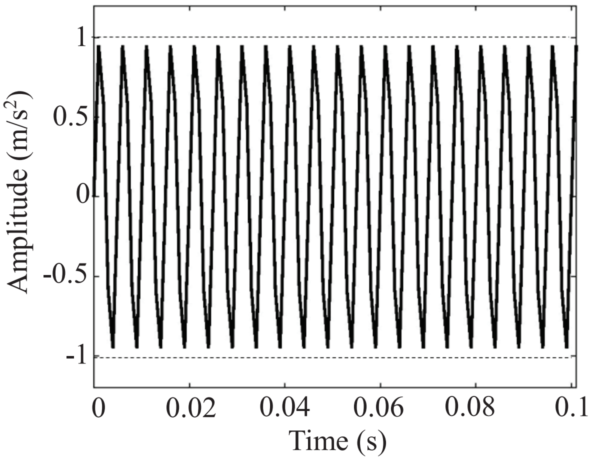

(a) Full waveform in time-domain.

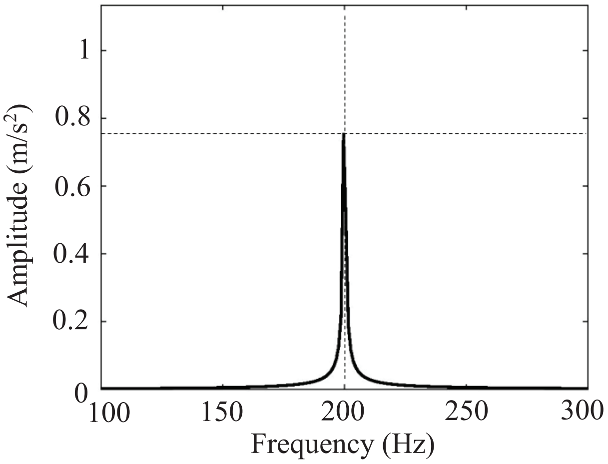

(b) Frequency spectrum obtained by FFT.

Fig. 2.2. Result of simulation signal for second trial.

The simulation result of second simulation is shown in **Fig. 2.2**. **Figure 2.2(a)** is full waveform of simulation signal in time-domain. On the other hand, **Fig. 2.2(b)** shows frequency spectrum obtained by FFT. Let us compare the result shown in **Fig. 2.2** to the result in **Fig. 2.1**. As can be seen from **Fig. 2.2**, both time-domain and frequency spectrum do not show similar result to **Fig. 2.1**. The time-domain signal in **Fig. 2.2(a)** is deferent from **Fig. 2.1(a)**. As shown in the figure, time-domain signal in **Fig. 2.1(a)** is smoother than in **Fig. 2.2(b)**. Instead, time-domain signal in **Fig. 2.2(b)** is distorted comparing with **Fig. 2.1(b),** consequently the amplitude cannot reach 1 m/s^2. On the other hand, the frequency spectrum shown in **Fig. 2.2(b)** is smoother than **Fig. 2.1(b)**. The resolution of frequency spectrum in **Fig. 2.2(b)** is becoming high, but the amplitude cannot reach 1 m/s^2. Therefore, if the sampling frequency f_{sam} becomes low, then time resolution in time-domain signal is becoming low, otherwise frequency resolution is becoming high. In this second trial, the computational time was 0.87905 seconds.

The parameter is changed for the third trial of simulation; new parameters are shown in **Table 2.3**. Based on this table, the data length N is decreased becoming 500 points (1000 points to be 500 points) and other parameters are same as **Table 2.1**.

Table 2.8. Parameter of simulation signal for third simulation.

Frequency of signal ω_x	200 Hz
Amplitude A	1 m/s^2
Sampling frequency f_{sam}	10 kHz
data length N	500 points

The result is shown in **Fig. 2.3**. **Figure 2.3(a)** is full waveform of simulation signal in time-domain. On the other hand, **Fig. 2.3(b)** shows frequency spectrum obtained by FFT. Let us compare the result shown in **Fig. 2.3** to the result shown **in Fig. 2.1**. The time-domain signal in **Fig. 2.3(a)** is deferent from **Fig. 2.1(a)**. Even though each amplitude signal shown 1 m/s^2, but signal in **Fig. 2.3(a)** is only 0.05 seconds, whereas the signal in **Fig. 2.1(a)** is 0.1 seconds. On the other hand, the frequency spectrum as shown in **Fig. 2.3(b)** is more bad than in **Fig. 2.1(b)** because frequency resolution of **Fig. 2.3(b)** is becoming lower than one in **Fig. 2.1(b)**. Therefore, if the data length N becomes short, then the frequency resolution is becoming low. In this third trial, the computational time was 0.88105 seconds.

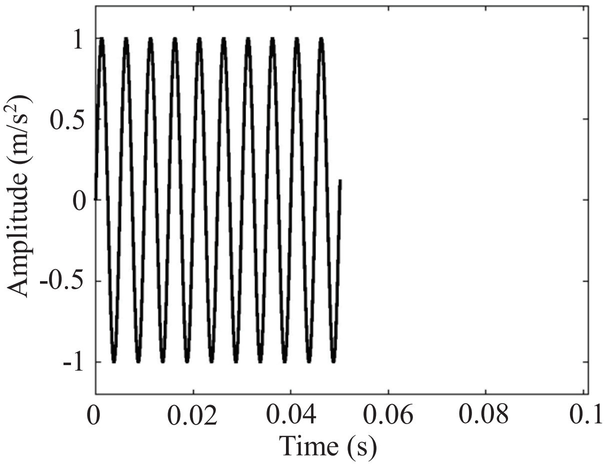

(a) Full waveform in time-domain.

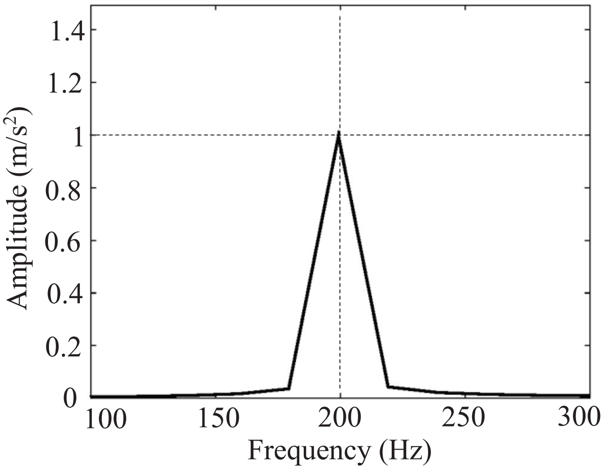

(b) Frequency spectrum obtained by FFT.

Fig. 2.3. Result of simulation signal for third simulation.

Next, we simulate signal with increasing amplitude over the time and applying FFT to simulated signal. The simulation signal is $w(t) = \exp(30t) \times \sin(2\pi \times \omega_x t)$. Parameter input in this simulation signal is shown in **Table 2.4**.

Table 2.9. Parameter of simulation signal $w(t)$.

Frequency of signal ω_x	200 Hz
Sampling frequency f_{sam}	10 kHz
data length N	1000 points

Figure 2.4 shows the result of simulation signal. **Fig. 2.4(a)** is full simulation signal in time-domain. As can be seen from **Fig. 2.4(a)**, the amplitude is exponentially growing up as function of time rather than previous simulation signal in **Fig. 2.1** till **Fig. 2.3**. On the other hand, **Fig. 2.4(c)** shows frequency spectrum obtained by FFT. As can be seen from the figure, frequency signal is 200 Hz which is same as in **Fig. 2.1(b)**. However, the amplitude of frequency spectrum is different, namely 6.4 m/s^2.

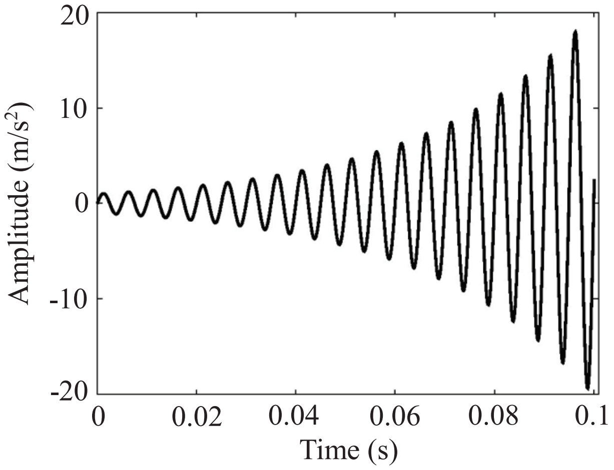

(a) Full waveform in time-domain.

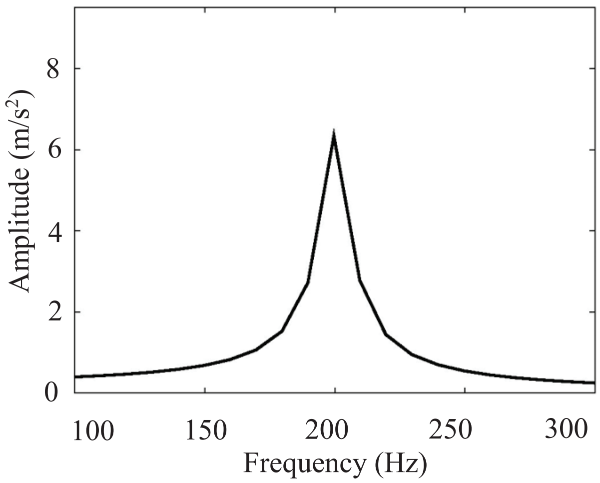

(b) Frequency spectrum obtained by FFT.

Fig. 2.4. Result of simulation signal *w*(*t*).

Following, we also simulate a signal which contains different frequencies over the time but same in amplitude. In this simulation, five simulation signals with different frequency are combined. Those signals are $y_1(t) = \sin(2\pi \times \omega_1 t)$; $y_2(t) = \sin(2\pi \times \omega_2 t)$; $y_3(t) = \sin(2\pi \times \omega_3 t)$; $y_4(t) = \sin(2\pi \times \omega_4 t)$; and $y_5(t) = \sin(2\pi \times \omega_5 t)$. The parameters of those signals are shown in **Table 2.5**.

Table 2.10. Parameter of simulation signal $y(t)$ with different frequency.

Frequency of signal ω_y	$\omega_1 = 100$, $\omega_2 = 300$, $\omega_3 = 190$, $\omega_4 = 150$, and $\omega_5 = 200$ Hz
Amplitude A	1 m/s^2
Sampling frequency f_{sam}	10 kHz
data length N	5000 points

Figure 2.5 shows the result of simulation signal. **Fig. 2.5(a)** is full simulation signal in time-domain. As can be seen from the figure, the amplitude is 1 m/s^2 and the signal contains different frequency over the time. On the other hand, **Fig. 2.5(b)** shows frequency spectrum of simulation signal obtained by FFT. As shown in the figure, all frequencies appear in this spectrum. However, the amplitude of frequency spectrum is different, namely 0.2 m/s^2. Here, the FTT averages the signal amplitude.

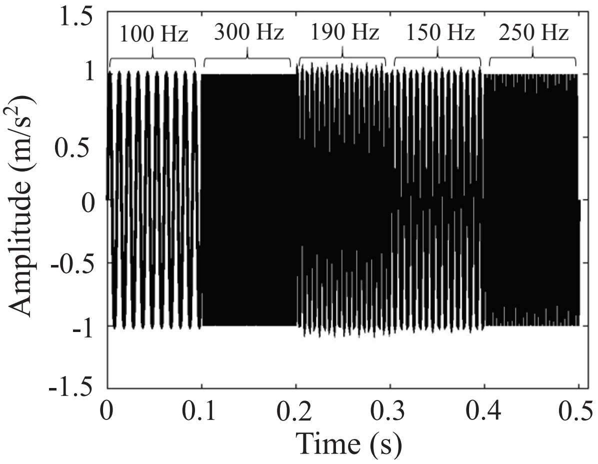

(a) Full waveform in time-domain.

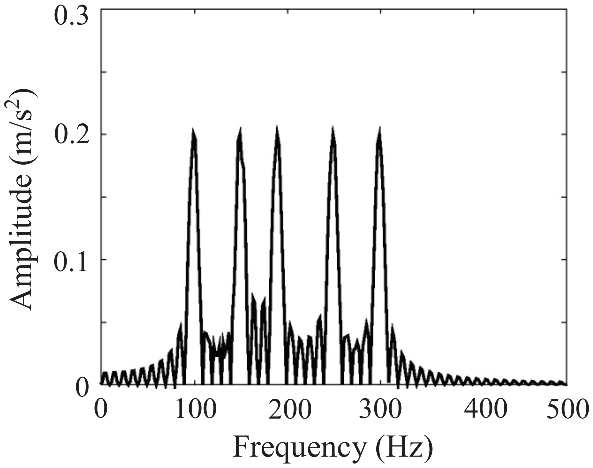

(b) Frequency spectrum obtained by FFT.

Fig. 2.5. Result of simulation signal.

From those simulations results, the advantage of the use of FFT is that FFT is quick method for transforming signal in time-domain to the frequency-domain. However, the disadvantages of the FFT to be applied for signal analysis is the trade-off between time and frequency resolutions, i.e. the higher the frequency signal resolution, the lower the time resolution is, and vice versa as shown in the above result in **Fig. 2.1**, **Fig. 2.2**, and **Fig. 2.3**. And, difficult also to find fit amplitude in frequency spectrum of FFT as shown in **Fig. 2.4** and **Fig. 2.5** because FTT averages the signal amplitude in the frequency spectrum. And, FFT cannot be used to analyze signal both in the time and frequency domains because FFT provides spectrum in just frequency domain.

To overcome the limitation of FFT, time–frequency analysis (TFA) methods which map the one-dimensional signal to a two-dimensional time–frequency plane have a great potential to monitor machining process. Several researchers have used TFA methods for monitoring chatter and tool wear as in refs. [3,25]. Because the TFA methods can provide machining states both in the time and frequency domains. And, short-time Fourier (STFT) and wavelet transforms are widely applied for vibration analysis occurring in machining processes.

2.2. Short-Time Fourier Transform

Short-time Fourier transform (STFT) is one of TFA methods which are widely used to analyze signals obtained in machining. Kolluru and Axinte [3] used STFT for analyzing acceleration signal to detect chatter in milling and was combined with FFT results. In their work, a coupled dynamic response of tool and workpiece was observed both for thin-walled straight cantilever and for ring type casing. STFT was also utilized for analyzing acceleration and cutting force signals to monitor chatter and tool wear in high-speed milling of aluminum alloys [26].

The idea of STFT is computing the Fourier transform in short, successive time windows over the entire time series. Given a data set *x*(*t*), the STFT at time *t* and frequency ω is represented as [24];

$$STFT(t,\omega) = \int_{-\infty}^{\infty} x(s)w(s-t)e^{-j\omega s}ds. \tag{2.2}$$

where *w*(*s*-*t*) is a windowing function sliding along the time axis to characterize the change of frequency components at different time intervals, i.e., a series of the conventional Fourier transforms of finite length time signal are evaluated by applying a windowing function to the original time signal. Here, Hanning window of $w(s-t) = \frac{1}{2}\left[1-\cos\left(\frac{2\pi(s-t)}{N-1}\right)\right]$ are used. *N* is the data length *N* which determines frequency sampling as mention in previous subchapter. And frequency sampling affects on the time-frequency resolution of STFT spectrum. If the frequency sampling in time-domain is high, then time-frequency resolution becomes low and vise-versa.

Following, simulation signal $y(t)$ as given in previous example is demonstrated once more to understand STFT performance for signal analysis. **Figure 2.6** shows the result of simulation signal. **Fig. 2.6(a)** is full waveform of simulation signal in time-domain. As can be seen from the figure, the amplitude is 1 m/s^2 and the signal contains different frequency over the time. Besides, **Fig. 2.6(b)** is the magnification signal of signal in **Fig. 2.6(a)**. On the other hand, **Fig. 2.6(c)** shows STFT spectrum. All frequencies appear in this spectrum, namely; 100, 300, 190, 150, and 250 Hz. However, the STFT spectrum contains poor resolution and frequency is too dilating. Besides that, the STFT spectrum looks like the overlapped and disjointed blocks.

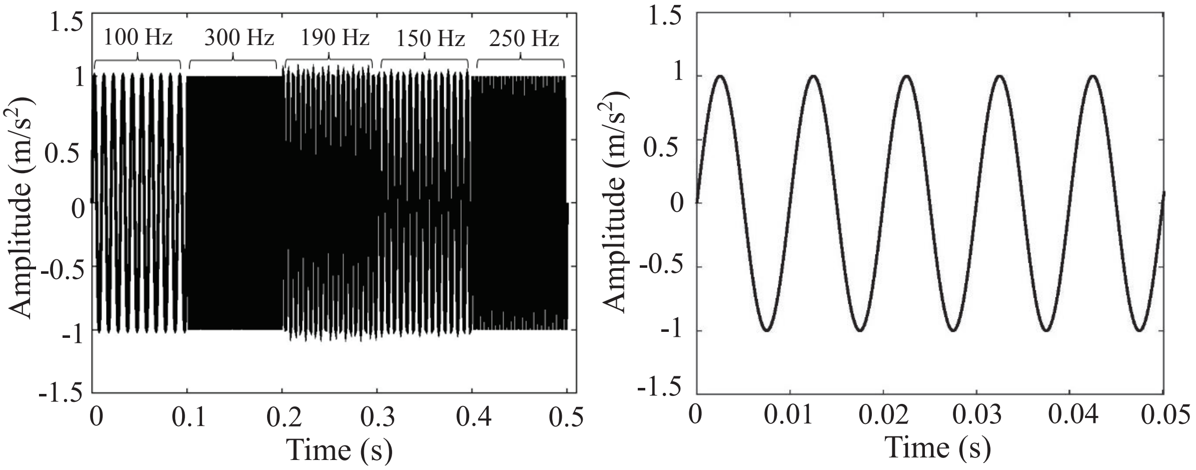

(a) Full waveform in time-domain.

(b) Magnification signal in **Fig. 2.6(a)**.

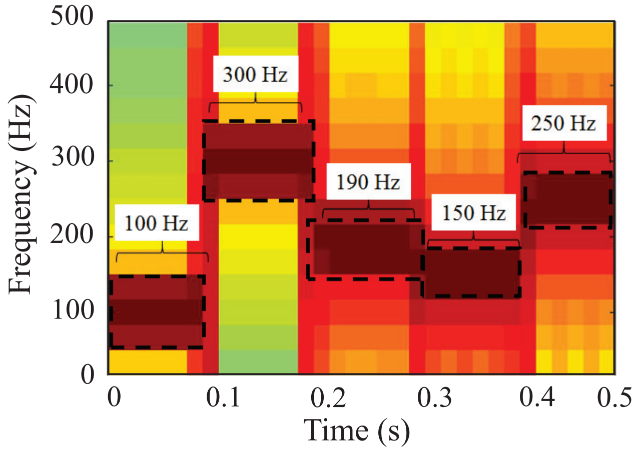

(c) STFT spectrum.

Fig. 2.6. Simulation result in STFT for first trial.

Now the simulation signal is changed its sampling frequency f_{sam} becoming 1 kHz with same other parameters. The result is shown in **Fig. 2.7**. **Fig. 2.7(a)** shows the magnification signal and **Fig. 2.7(b)** is STFT spectrum. As shown in **Fig. 2.7(b)**, the resolution is better than STFT spectrum in **Fig. 2.6(b)**. And, frequency is more compressed than **Fig. 2.6(c)**, therefore we can get more precise frequency. However, the time-domain signal in **Fig. 2.7(a)** shows distorted signal comparing with **Fig. 2.6(b)** or time resolution is becoming low.

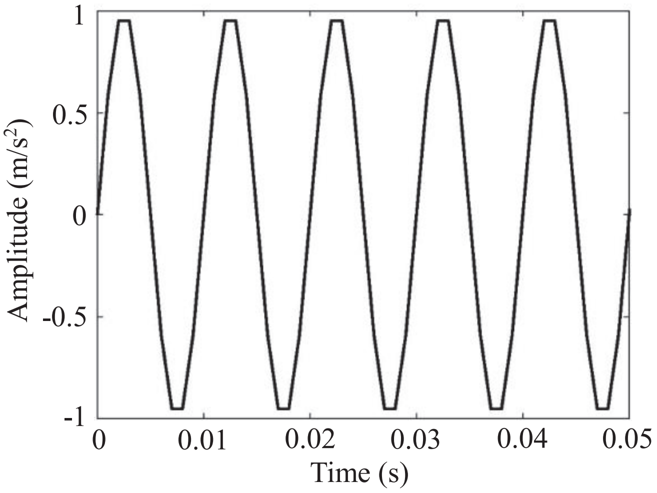

(a) Magnification signal.

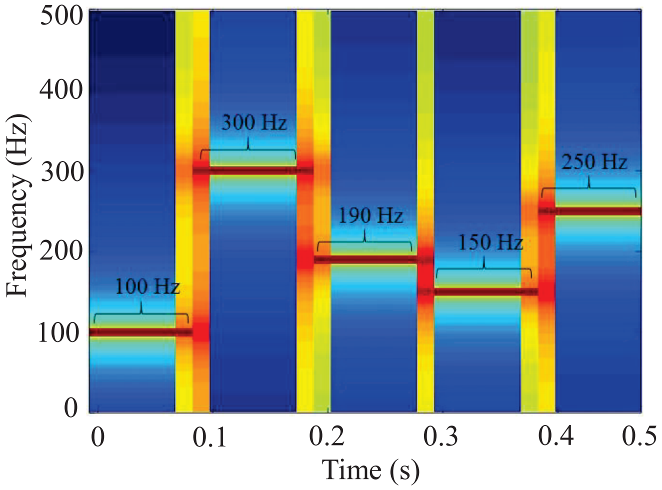

(b) STFT spectrum.

Fig. 2.7. Simulation results in STFT for second trial.

According to the simulation result, STFT cannot provide good time and frequency resolution simultaneously, instead STFT gives the trade-off between time and frequency resolutions, i.e. the higher the frequency signal resolution, the lower the time resolution is, and vice versa. And the STFT provides spectrum with overlapped and disjointed blocks.

2.3. Wavelet Transform

Wavelet Transform is one of powerful TFA methods which widely applied to analyze signals for machining process monitoring. Kamarthi and Pittner [27] used a wavelet transform to analyze the cutting force and acceleration signals obtained in turning to detect flank wear and they compared the wavelet results to the FFT results. Consequently, they recommended FFT to be used in analyzing acceleration signals whereas wavelet transform was acceptable to analyze cutting forces. Xu et al. [28] employed a wavelet transform to analyze the force and torque signals for drill wear estimation.

The wavelet transforms of signal $x(t)$ is defined with respect to an analyzing wavelet, which is complex in general, as

$$X(\tau,s)=\frac{1}{\sqrt{|s|}}\int x(t).\psi\left(\frac{t-\tau}{s}\right)dt \qquad (2.4)$$

To show the time and frequency resolution of wavelet transform, simulation signal $z(t)=A\sin(2\times\omega_x t)\,x(t)$ is demonstrated. The frequency signal ω_1, sampling frequency f_{sam} and data length N were 10 Hz, 100 Hz and 100 points, and the amplitude is 1 m/s^2.

Figure 2.8 shows the result of simulation signal. **Fig. 2.8(a)** is full simulation signal in time domain. As can be seen from the figure, the amplitude is 1 m/s^2 as the signal setting. On the other hand, **Fig. 2.8(b)** shows time-frequency domain of wavelet spectrum. As shown in the figure, the wavelet spectrum is better than STFT spectrum in **Fig. 2.6(c),** but wavelet spectrum contains poor time-frequency resolution. As can be seen from **Fig. 2.8(b)**, the wavelet spectrum looks like the overlapped and disjointed blocks.

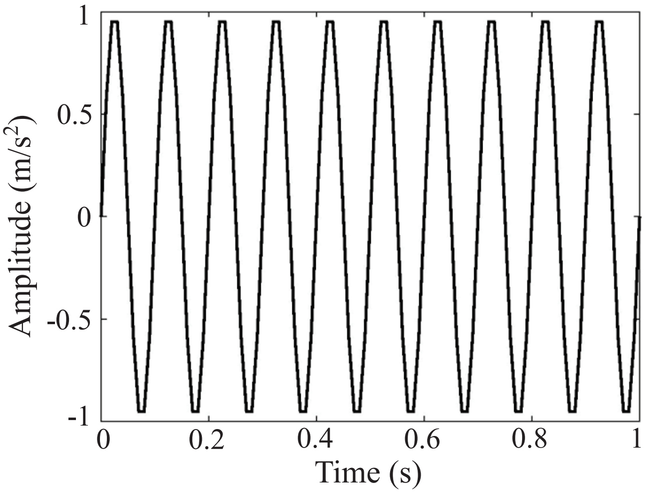

(a) Waveform in time-domain.

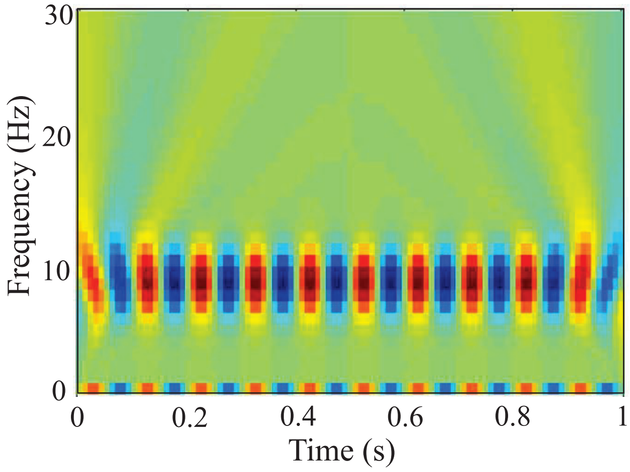

(b) Wavelet spectrum.

Fig. 2.8. Simulation result in wavelet for first trial.

Now the simulation signal is changed its sampling frequency f_{sam} and number of data N becoming 1000 Hz and 1001 with same other parameters. The result is shown in **Fig. 2.9**. Time-domain simulation signal is shown in **Fig. 2.9(a)** and **Fig. 2.9(b)** is wavelet spectrum. As can be seen from the figures, the time-domain signal in **Fig. 2.9(a)** shows smooth oscillation and better than **Fig. 2.8(a)**. And the wavelet spectrum as shown in **Fig. 2.9(b)** shows also better resolution than **Fig. 2.8(b)**.

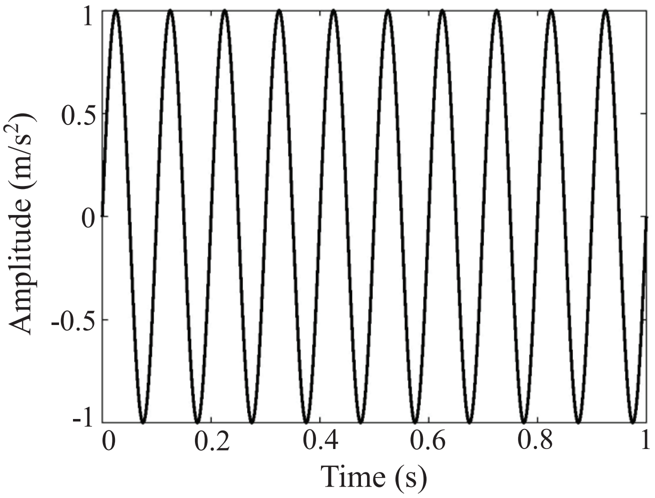

(a) Waveform in time-domain.

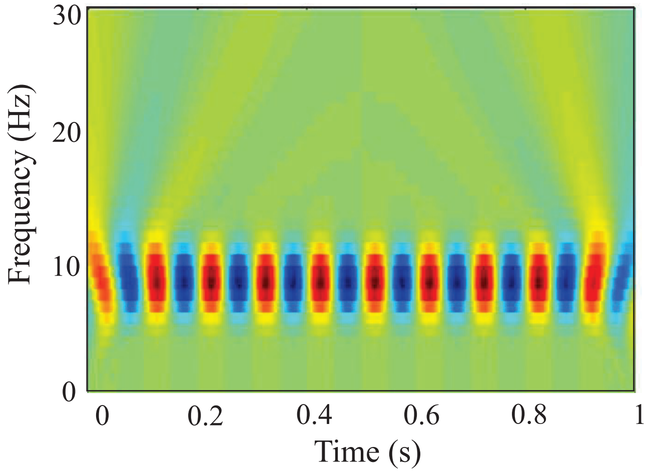

(b) Wavelet spectrum.

Fig. 2.9. Simulation result in wavelet for first trial.

A few people who interesting in signal processing mentioned the drawbacks of conventional spectral analysis techniques above; FFT, STFT, and wavelet transforms, which is due to the FFT. Thus, both time and frequency resolution cannot be arbitrarily high in FFT [25,26,29]. Gu et al. stated that the disadvantage of the STFT to applied for non-stationary signal analysis obtained in machining is the trade-off between time and frequency resolutions [29], i.e. the higher the frequency resolution, the lower the time resolution is, and vice versa. Besides, in wavelet transform, it is difficult to determine the suitable wavelet base functions and decomposition levels which affect on the analysis results significantly [31].

2.4. Summary

In this chapter, conventional spectral analysis tools are explained. They are including fast Fourier (FFT), short-time Fourier (STFT), and wavelet transforms. Simulation signal is created to show the performance of each spectral analysis. From those simulations results,

1. The advantage of the use of FFT is that FFT is quick method for transforming signals in time-domain to the frequency-domain. However, the disadvantages of the FFT to be applied for signal analysis is the trade-off between time and frequency resolutions, i.e. the higher the frequency signal resolution, the lower the time resolution is, and vice versa. And, difficult to find fit amplitude in frequency spectrum because FTT averages the signal amplitude in frequency spectrum.
2. The idea of STFT is computing the Fourier transform in short, successive time windows, rather than once over the entire time series. STFT provides signal analysis in time-frequency rather than FFT. According to the simulation result, STFT cannot provide good time and frequency resolution simultaneously, instead STFT gives the trade-off between time and frequency resolutions, i.e. the higher the frequency signal resolution, the lower the time resolution is, and vice versa. And the STFT provides spectrum with overlapped and disjointed blocks.
3. The wavelet spectrum is better than STFT spectrum, but wavelet spectrum still contains poor time-frequency resolution. The wavelet spectrum looks like the overlapped and disjointed blocks. When the frequency sampling is reduced, the wavelet spectrum shows better time and frequency resolution.

Chapter 3

Hilbert-Huang Transform

3.1. Introduction

Hilbert–Huang transform (HHT) is one of time-frequency analyses (TFA) which was developed by Huang et al. in 1995 [31]. Unlike the traditional signal analysis techniques, such as FFT, STFT, and wavelet transforms, this method was especially used for analyzing nonlinear and non-stationary signal. And, different from other conventional TFA methods, HHT does not involve the concept of frequency resolution or time resolution but introduces the concept of instantaneous frequency. Consequently, a uniform high time and frequency resolution are obtained [32].

HHT is widely used for analyzing signals to detect the damage of the transmission element in mechanical system. HHT was used to analyze acceleration and acoustic emission signals for gear damage detecting [33,34]. HHT was also used for analyzing velocity signal to detect rotor fault of rotating shaft [35]. Peng et al. [36] proposed the combination of wavelet transform and HHT for acceleration signal analysis to detect the fault of a rolling bearing. Wavelet transform worked as the preprocessor of signal analysis and following HHT was applied. The proposed method was compared with the wavelet spectrum through experimental case studies. The comparison results showed that the proposed method had better in time-frequency resolution and computational efficiency than wavelet. Yan et al. [37] investigated the utility of HHT for acceleration signal analysis to monitor the health of bearing machine. The results demonstrated the effectiveness of HHT for signal decomposition and feature extraction in the application of bearing machine health monitoring. Saidi, et al. [38] utilized the advantages of Bi-Spectrum and EMD (BSEMD) for analyzing acceleration signals to detect bearing failures in machine. The proposed method was confirmed with the experimental tests and the results showed that BSEMD techniques can effectively diagnosis bearing failures. Yang and Wu [39] studied the diagnostic effectiveness of the gear deterioration through the feature extraction process by using HHT and was supported by the principal component analysis (PCA) and the artificial neural network (ANN) for the gear deterioration diagnostic. The diagnostic results obtained using showed that the different types and levels of gear malfunctions could be identified effectively by the proposed approach.

However, the use of HHT to analyze the signal obtained in machining is limited. We can classify it into two categories; utilization of HHT for chatter detection [40] and tool wear monitoring [41,42]. Peng [43] used HHT for analyzing cutting force to detect tool breakage in the milling process. Cao et al. [44] combined the benefit of wavelet and HHT for chatter detection. Here, wavelet was used as a preprocessor of signal analysis before employing HHT. The motor current signal was decomposed into IMFs by HHT and extracted energy index and kurtosis index based on those IMFs for chatter detection by Liu et al. [45].

Moreover, HHT has not been implemented for analyzing the vibration occurring in turning operation referring to articles, abstracts or keywords in the Scopus® database [46] using the words “chatter, turning” and considering all types of documents in the subject area of physical sciences, published after 1998, and then refining the search manually to define a more specific subject area. Actually, HHT consists of two consecutive steps, namely; an empirical mode decomposition (EMD) and Hilbert transform. They will be explained in following sections.

3.2. Empirical Mode Decomposition

The first step of Hilbert-Huang transform (HHT) is Empirical Mode Decomposition (EMD) process, which decompose original signal into a series of components called intrinsic mode functions (IMFs = $\{c_1, c_2, \ldots\}$). Each IMF contains individual mode oscillation, amplitude, and frequency as a function of time. The EMD process is shown using the flow chart given in **Fig. 3.1** and the steps are explained using simulation signal as follows:

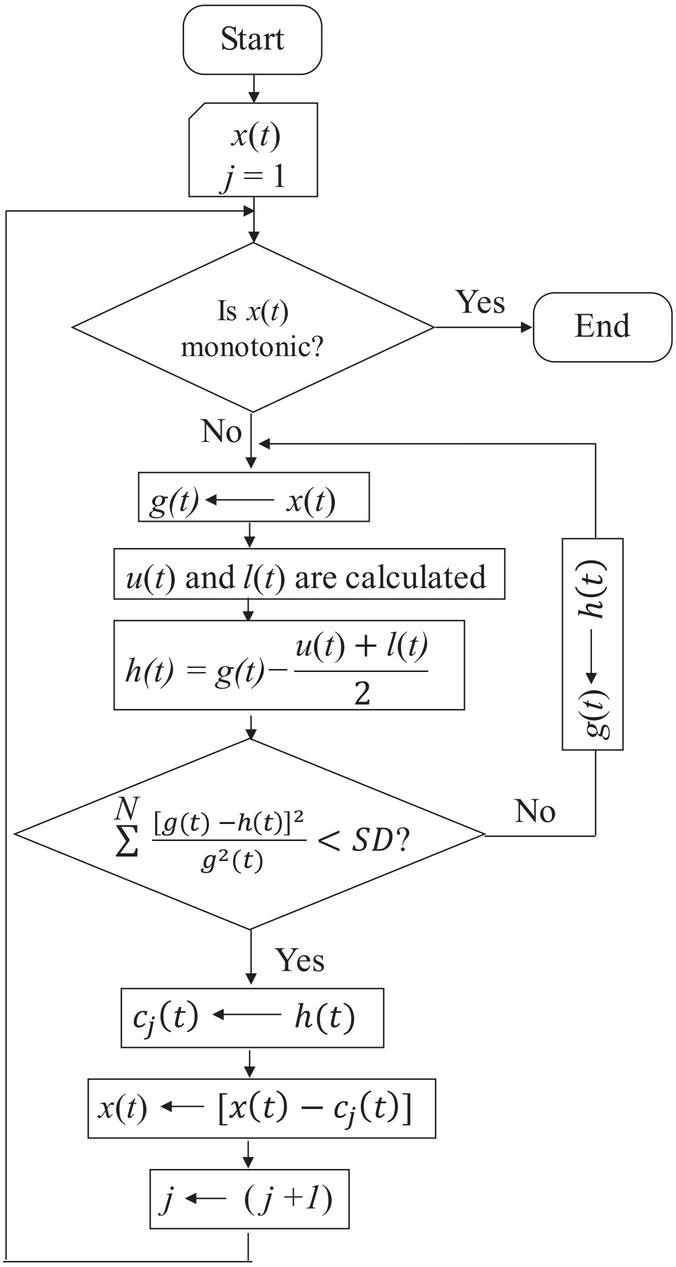

Fig. 3.1. Flow chart of EMD process.

1. Simulation signal, $x(t) = \sin(2\pi\omega_1 t) + 1.3\sin(2\pi\omega_2 t) + 1.1\sin(2\pi\omega_3 t)$, is considered as raw data whose length is $N = 5000$ points and sampling frequency f_s is 10000 Hz. Here, ω_1, ω_2, and ω_3 are signal frequency and they are set 100, 150, and 300 Hz, respectively. And the simulation signal is shown in **Fig. 3.2** as the black curve. This signal is magnification of full signal.
2. The local maxima and minima are identified first, and then they are connected with cubic spline line to form the upper $u(t)$ and the lower $l(t)$ envelopes. These steps are shown in **Fig. 3.2**. The upper $u(t)$ and the lower $l(t)$ envelopes are shown with red and blue curves, respectively.

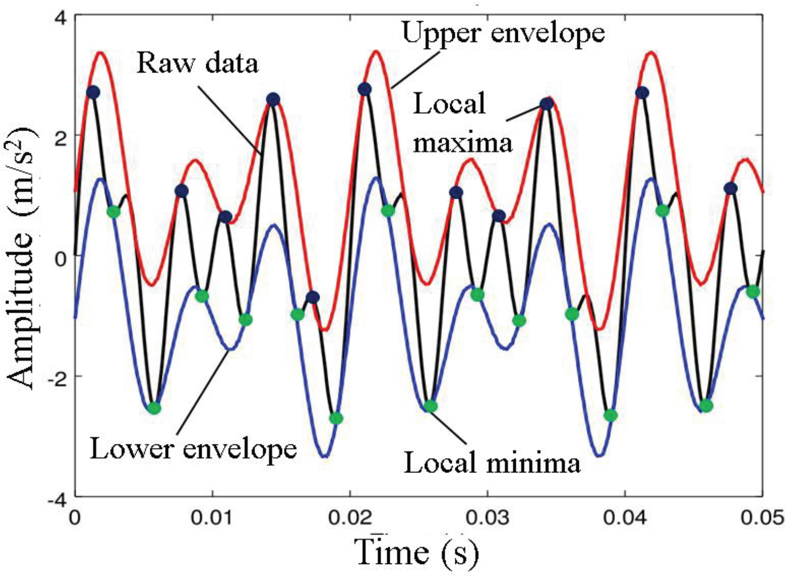

Fig. 3.2. Creating lower and upper envelopes of the signal.

3. Compute the mean of two envelopes and subtract the signal $x(t)$ by the mean of two envelopes to get the proto-IMF h_i.

   $$h_i = x(t) - \left(\frac{u(t)+l(t)}{2}\right) \tag{3.1}$$

   These steps are shown in **Fig. 3.3** and **Fig. 3.4**.

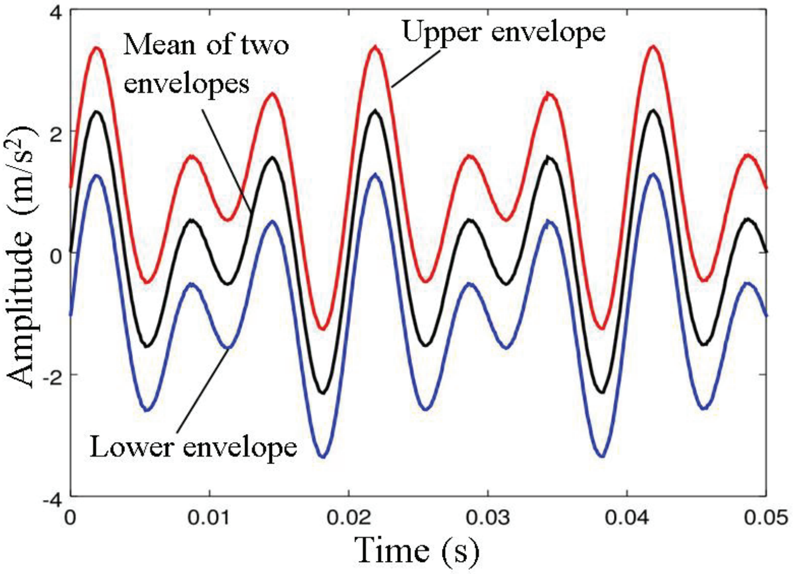

Fig. 3.3. Compute the mean of envelopes.

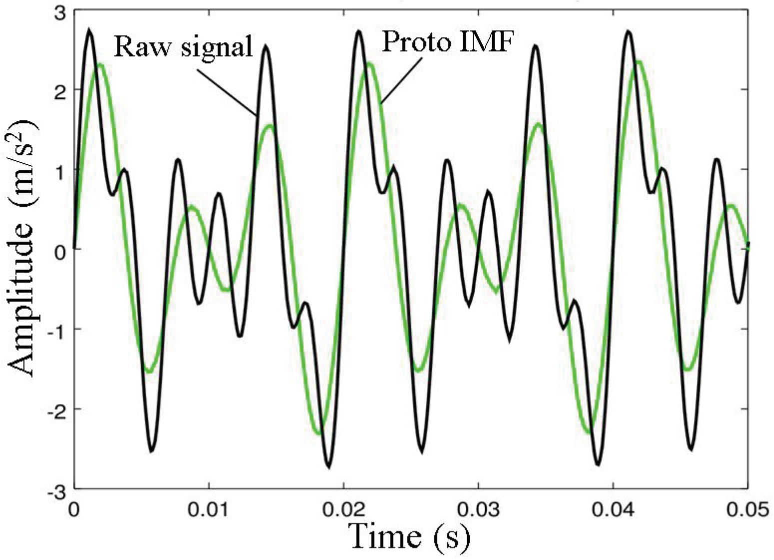

Fig. 3.4. Compute the proto IMF of signal.

4. The $h(t)$ should be checked against the stoppage criterion of IMF as expressed in Eq. (3.2) to determine if it is an IMF or not.

$$\sum^{N} \frac{[h_i - h_{i-1}]^2}{h_i^2} < SD \tag{3.2}$$

   where h_i is the sifting result in the i-th iteration. *SD* is a threshold value and it was set 0.2 in this study.
5. If h_i does not satisfy to the stoppage criterion of IMF, then treat h_i as new input data and iterate steps 2–4 till h_i satisfies the stoppage criterion of IMF.
6. After h_i fulfills the condition as expressed in Eq. (3.2), assign it as a component of IMF $c_j(t)$. And the residue $r(t)$ is defined as; $r(t) = x(t) - c_j(t)$. Repeat the operation step 2 to 6 for extracting the next IMF using the new input data $r(t)$.
7. The operation ends when the extracting result of residue $r(t)$ contains no more than one extremum. Then, the residue is called as monotonic residue $res(t)$.

The output of the EMD process is a set of IMF components $c_j(t)$ (j = 1, 2… N_k), where N_k is a number of modes. In addition, the last mode $c_{Nk}(t)$ is a monotonic residue $res.(t)$. An example of a set of IMF components of simulation signal is shown in **Fig. 3.5**. As can be seen from the figure, the first IMF c_1 is the component with highest frequency, otherwise the last IMF c_6 is the component with lowest frequency and monotonic residue has no physical meaning. In addition, EMD can separate complex signal into simple signal in each IMF and each IMF contains individual mode oscillation, amplitude, and frequency.

The decomposition of the signal *x*(*t*) to be a set of IMF components and a monotonic residue can be achieved mathematically using;

$$x(t) = \sum_{j=1}^{N_k} c_j(t) + r_{Nk}(t) \qquad (3.3)$$

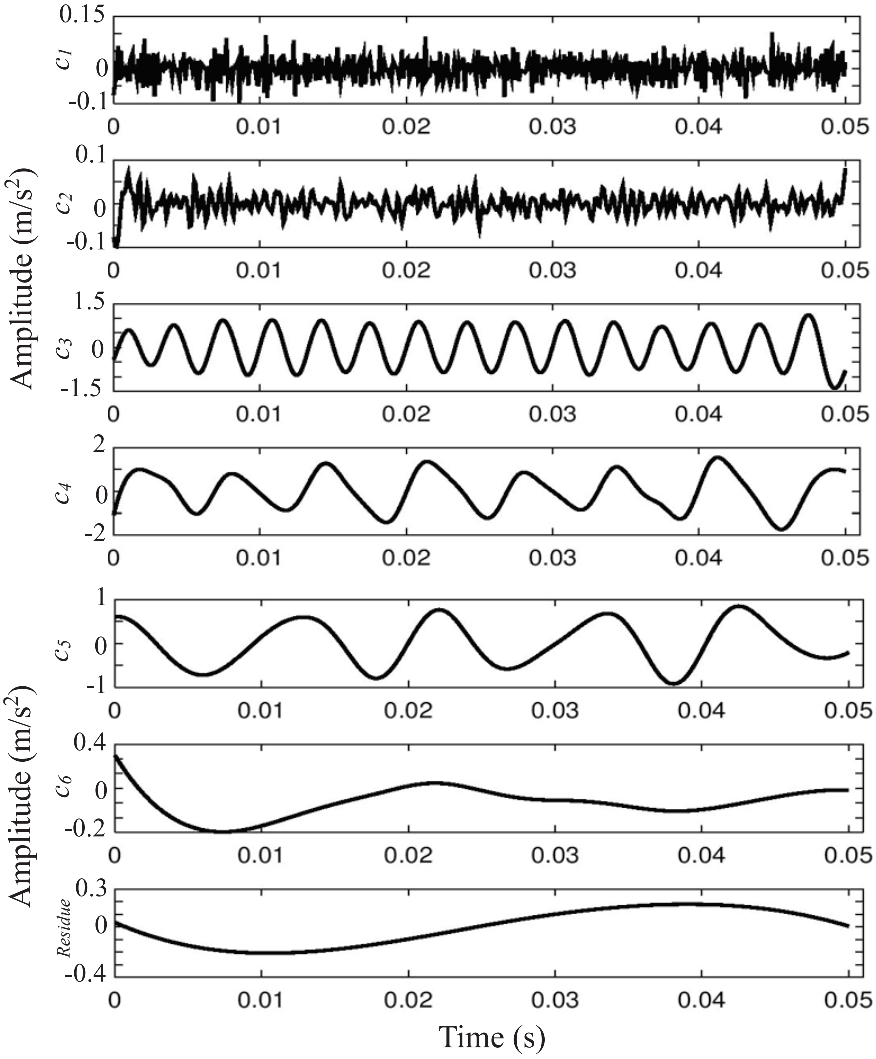

Fig. 3.5. Example of IMF components and monotonic residue obtained by EMD process.

3.3. Hilbert Transform

The next step of HHT is applying Hilbert transform to all IMF components for generating an energy-time-frequency distribution which is called as a Hilbert spectrum. The Hilbert transform of each IMF $c_j(t)$ is defined as [31];

$$H(t) = \frac{1}{\pi}\int_{-\infty}^{+\infty}\frac{c_j(\tau)}{t-\tau}d\tau \tag{3.4}$$

The instantaneous amplitude of Hilbert transform can be calculated by $\alpha(t) = \sqrt{c_j^2(t) + y^2(t)}$, the phase is $\emptyset(t) = tan^{-1}\left(\frac{y(t)}{c_j(t)}\right)$, and the instantaneous frequency can be achieved by $\omega(t) = \frac{d\emptyset(t)}{dt}$.

An example for Hilbert spectrum of simulation signal $x(t)$ obtained by Hilbert transform is shown in **Fig. 3.6**. As can be seen, Hilbert spectrum provides good time and frequency resolution, unlike than STFT and wavelet transform which provide spectrum with overlapped and disjointed blocks as shown in Chapter 2.

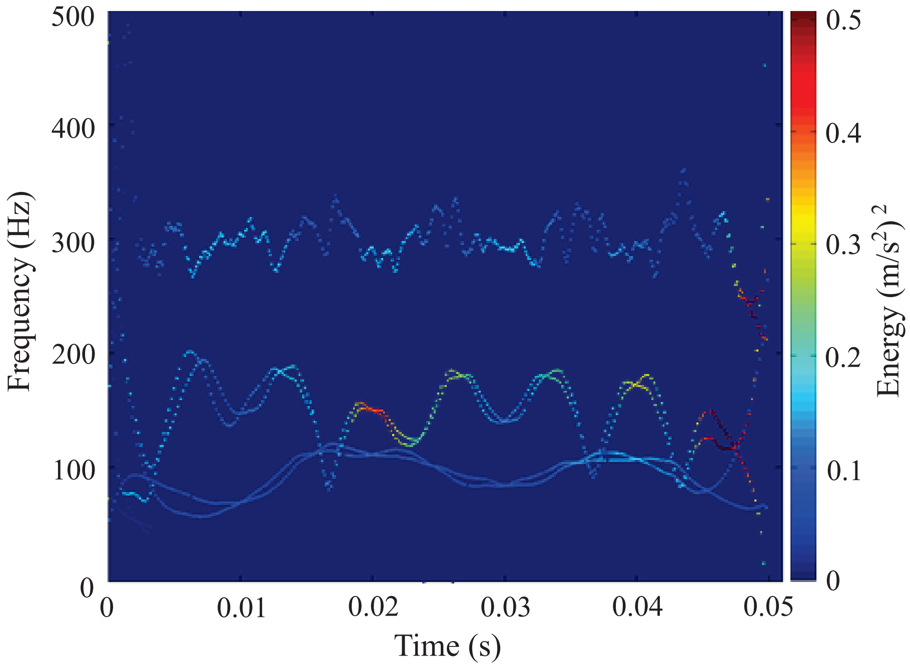

Fig. 3.6. Example of Hilbert spectrum obtained by Hilbert transform.

3.4. Summary

Hilbert-Huang transform (HHT) is widely applied to detect the damage of the transmission element in mechanical system but the use of HHT in machining process is limited. HHT consists of two consecutive steps, namely; an empirical mode decomposition (EMD) and Hilbert transform. By EMD process, raw signal is decomposed into a series of components called intrinsic mode functions (IMFs). Each IMF contains individual mode oscillation, amplitude, and frequency as a function of time. The first IMF is the component with highest frequency, otherwise the last IMF is the component with lowest frequency and monotonic residue has no physical meaning. Besides that, an example of Hilbert spectrum of HHT is provided. Hilbert spectrum provides good time and frequency resolution rather than spectrum of STFT or wavelet transform.

Chapter 4

Vibration Models in Machining

4.1. Review of Chatter Vibration in Machining Process

Chatter vibration can occur during machining operations including turning, milling, grinding and drilling. It has been a topic of industrial and academic interest for many years because it can induce numerous problems like decreasing surface finish, excessive noise, breakage of machine tool components, accelerate tool wear, reduced material removal rate, and productivity. Chatter was first studied by Taylor [47], who carried out extensive studies on metal-cutting processes. And he stated that chatter is the most obscure and delicate of all problems facing the operator. Arnold [48] explained the mechanisms generating chatter during metal cutting process analytically and he confirmed by experimentally turning tests. Koenigsberger and Tlusty [49] examined chatter vibration which was caused by instability in cutting processes, including turning, milling, and grinding. Meritt [50] studied the modeling of the structural response and stability limit aspects of regenerative chatter in orthogonal cutting.

In a machining process, mechanical vibration due to a lack of stiffness of the machine tool system can be classified into three group; free, forced and self-excited or chatter vibrations [51]. Free vibration is induced by shock and forced vibration is due to unbalance effects in machine tool assemblies. Free and forced vibrations can be easily identified and eliminated. But chatter vibration extracts energy to start and grow during machining process from the interaction between the cutting tool–workpiece and brings the system to instability [52]. M. Wiercigroch and E. Budak classified chatter vibration into primary and secondary chatters [53]. Primary chatter is caused by friction between tool–workpiece. Secondary chatter is caused by the regeneration of wavy surface on the workpiece. Regenerative vibration is the most destructive among all other vibrations.

Most of the research has been carried out to avoid this regenerative chatter vibration by predicting.

To avoid chatter vibration by predicting, a stability lobe diagram (SLD) is generated prior to real machining. SLD can be used to determine the cutting parameters, which responsible for machining process instability. Generally, the depth of cut is plotted against spindle speed on the diagram. SLD in machining was early developed by Meritt [50]. This was an important contribution, because it allowed an improvement in material removal rate without chatter by selecting appropriate process parameters. And then, SLD theory was extended by Tlusty [54] in high-speed milling, as well as by Altintas and Budak [55,56]. Furthermore, SLD has been widely applied in several research fields. Bravo et al. [57] used SLD for high-speed milling of monolithic workpieces. Campa et al. [58] proposed a methodology for chatter avoidance in milling of flexible thin floors using a bull-nose end mill by stability diagram. Alan et al. [59] generated SLDs for a multistage milling operation. Altintas et al. [60] presented an SLD with considering the process damping. It was found that accurate prediction of chatter stability at low speeds was dependent on the identification of the cutting force coefficients. The cutting force coefficients were found to be sensitive to the work material properties, cutting edge preparation, tool clearance angle, tool wear, cutting speed, and tool–workpiece contact mechanics. Kurata et al. [60] have also identified the process damping force coefficient from the plunge turning tests. The process damping coefficient was estimated by inverse solution of the stability using the characteristic equation of turning process when it was critically stable during cutting tests. Stability lobes were generated using this identified process damping coefficient. It was found that when tool wear reaches a level that covers the vibration wave left on the surface, process damping becomes fully effective and additional tool wear does not significantly change the damping during the process. Recently, Tunc and Budak [61] have explored the effect of process damping on the stability lobe diagram with considering the effect of cutting conditions and tool geometry. The analytical SLDs were then confirmed by milling tests experimentally.

To generate SLD, the machining system (tool-workpiece-holder-spindle) can be modeled by considering the degree-of-freedom (DoF) of a spring-mass-damper system of machining structure, for example, a single SDoF or 2DoF. Hanna and Tobias [62] presented an SDoF for the milling process. They considered the end mill as the flexible part of the machining system. The model has predicted the chatter stability, which is affected by the width of cut in three ranges like an unconditionally stable range, a conditionally stable range, and an unstable range. Chen and Tsao [63,64] presented 2DoF vibration models of the machining process with considering the workpiece as the flexible part. The effect of workpiece deformation on the stability was studied and the effect of the critical chip width under different spindle speed was also investigated. By considering the deformation of the workpiece, the results showed that the critical chip width of the deformed was always larger than the rigid body cases, especially at lower natural frequencies. And they claimed that 2DoF models were very good for deriving the stability and evaluating the influence of the deformation of the workpiece.

4.2. Vibration Model in Turning of Thin-Tubular Workpiece

In turning of thin-tubular operation, the cutting system is composed by tool, workpiece, and chuck. Especially, the workpiece can be deformed in x and y directions caused by cutting forces as shown in **Fig. 4.1** because the workpiece is considered as the flexible part of this machining system.

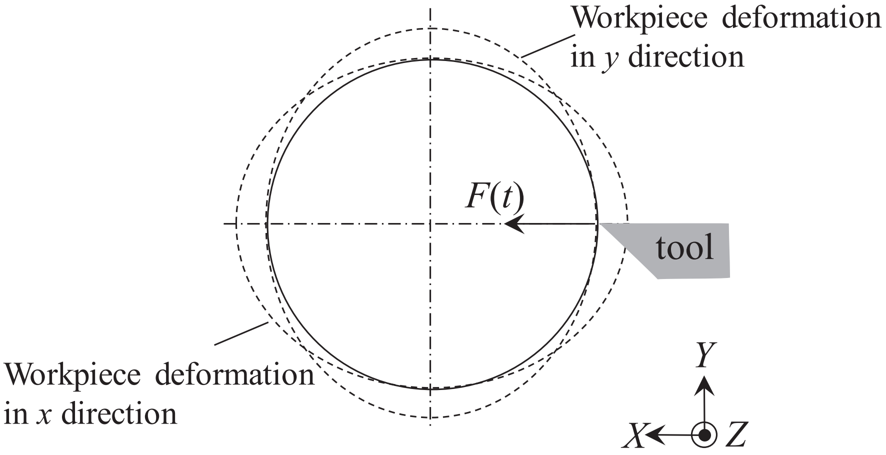

Fig. 4.1. Deformation of thin-tubular workpiece caused by cutting force.

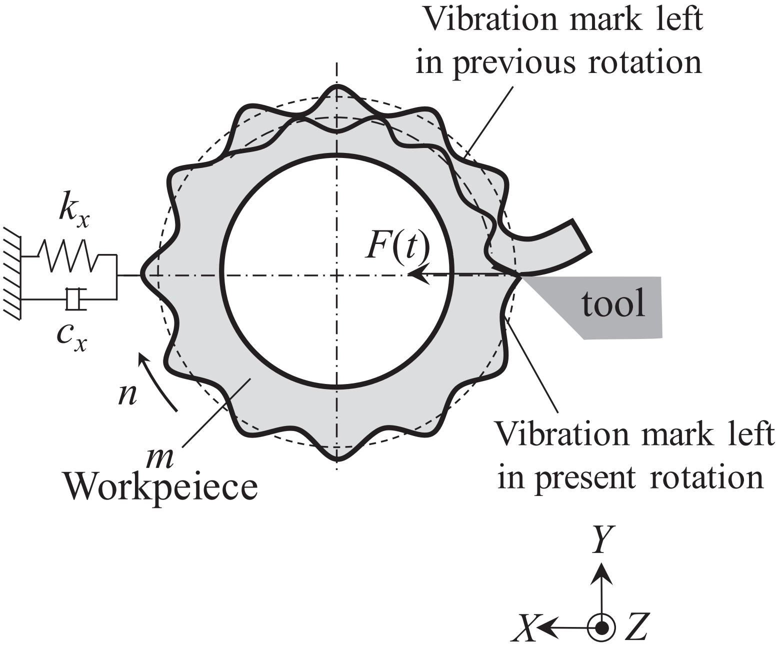

Fig. 4.2. Vibration model in turning of thin-tubular workpiece [54].

On the other hand, **Figure. 4.2** shows vibration model of two-degree-of-freedom (2DOF) system in turning of thin-tubular workpiece. The model consists of modal parameters; mass m, damping coefficient c, and stiffness k, so that the system can be vibrating by cutting force $F(t)$ during removal material. According to **Fig. 4.2**, cutting force is loaded on the workpiece during operation, and it cause vibration which produce wavy profile in workpiece. When the workpiece rotates, the tool encounters that wavy surface and consequently fluctuates the uncut chip thickness at any time. And the uncut chip thickness at any time depends on both the vibration mark left in previous rotation and the vibration mark in present vibration. The vibration subsequently determines whether the turning operation is stable or unstable (chatter occurs).

The equation of motion for vibration model of 2DOF system shown in **Fig. 4.2** can be expressed as follow;

$$[M]\begin{Bmatrix}\ddot{x}\\ \ddot{y}\end{Bmatrix}(t)+[C]\begin{Bmatrix}\dot{x}\\ \dot{y}\end{Bmatrix}(t)+[K]\begin{Bmatrix}x\\ y\end{Bmatrix}(t)=F(t) \qquad (4.1),$$

where [M], [C], and [K] are mass, damping and stiffness matrices. Besides, $\ddot{x}$ and $\ddot{y}$ are acceleration, whose can be represented as velocity and displacement.

On the other hand, the uncut chip thickness is expressed as follows [54];

$$h(t)=h_o(t)-\begin{Bmatrix}x(t)-x(t-\tau)\\ y(t)-y(t-\tau)\end{Bmatrix} \qquad (4.2),$$

in the Laplace domain is expressed as [54];

$$h(s)=h_o(s)+\left(e^{-s\tau}-1\right)\begin{Bmatrix}x(s)\\ y(s)\end{Bmatrix} \qquad (4.3),$$

where h_o is controlled uncut chip thickness and τ is a spindle revolution period.

And the cutting force is expressed as [54]:

$$F(s)=AK_sh(s) \qquad (4.4),$$

where A is width of cut and K_s is cutting force coefficient.

Besides, Eq. (4.1) can be represented as the relationship between the force and the displacement which well-known frequency response function [$G(s)$] as follow;

$$\begin{Bmatrix}x(s)\\ y(s)\end{Bmatrix}=[G(s)]AK_sh(s) \qquad (4.5)$$

Substituting (4.5) into (4.3) yields

$$h(s)=h_o(s)+\left(e^{-s\tau}-1\right)[G(s)]AK_sh(s) \qquad (4.6)$$

From Eq. (4.6), the ratio between controlled chip thickness to uncut chip thickness can be achieved as;

$$\frac{h_o(s)}{h(s)} = \frac{1}{1-\left(e^{-s\tau}-1\right)\left[G(s)\right]AK_s} \qquad (4.7)$$

The stability limit at the chatter vibration frequency ω_c can be determined by;

$$1-\left(e^{-s\tau}-1\right)\left[G(j\omega_c)\right]A_{a\lim}K_s = 0 \qquad (4.8),$$

where A_{alim} is maximum axial depth of cut for chatter free machining and $G(j\omega_c)$ is the frequency response function. This frequency response function can be expressed to other expression with considering the frequency ratio $r = \omega/\omega_c$ and damping ratio ζ, as follows;

$$G\left(j\omega_c\right) = \frac{1}{k}\left(\frac{\left(1-r^2\right)-i2\zeta r}{\left(1-r^2\right)^2+\left(2\zeta r\right)^2}\right) \qquad (4.9)$$

Eq. (4.9) shows a complex equation that can be expressed into real and imaginary parts as follows;

$$\operatorname{Re}\left[G\left(j\omega_c\right)\right] = \frac{1}{k}\left(\frac{1-r^2}{\left(1-r^2\right)^2+\left(2\zeta r\right)^2}\right) \qquad (4.10)$$

$$\operatorname{Im}\left[G\left(j\omega_c\right)\right] = \frac{1}{k}\left(\frac{-2\zeta r}{\left(1-r^2\right)^2+\left(2\zeta r\right)^2}\right) \qquad (4.11)$$

The frequency response functions $G(j\omega_c)$ in Eq. (4.8) determine the stability limit of depth of cut A_{alim} and phase angle ε as follows;

$$A_{a\lim} = -\frac{1}{2K_s \operatorname{Re}[G(j\omega_c)]} \qquad (4.12)$$

$$\varepsilon = \pi - 2\tan^{-1}\left(\frac{\operatorname{Re}[G(j\omega_c)]}{\operatorname{Im}[G(j\omega_c)]}\right) \qquad (4.13)$$

Stability lobes diagram (SLD) can be generated using Eqs. (4.13), (4.14) and calculates the spindle speed $n = \frac{60\omega_c}{lb+\varepsilon}$ with l_b is integer number of lobes ($l_b = 0, 1, 2, \ldots$).

The SLD distinguishes stable and unstable cutting (chatter occurs) operations for different combinations of width of cut and spindle speed. Here, we provide an example of SLD shown in **Fig. 4.3**. As can be seen from the figure, any combination of spindle rotational speed and depth of cut that appears above the lobe indicates unstable cutting, otherwise any combination of spindle rotational speed and depth of cut below of the lobe is stable.

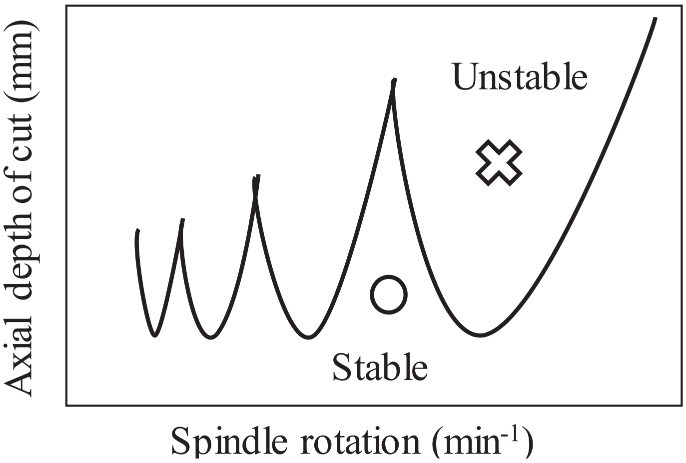

Fig. 4.3. Example stability lobe diagram (SLD).

4.3. Vibration Model in Thin-Walled Milling

Figure 4.4(a) shows side milling of thin-walled part along x-direction with the spindle rotation n, feed rate V_f, and axial cutting depth A_a. The workpiece is clamped at one end and the other sides are free. The cutting force F_y excites different modes of vibration such as bending, torsional, and stretching. In general, coupled vibration is excited in machining and the figure shows a typical workpiece displacement y. On the other hand, **Fig. 4.4(b)** shows cutting edge angle in down-milling. According to this figure, uncut chip thickness h, the radial cutting depth A_r, tool's rotational angle ϕ, start ϕ_s and exit ϕ_e angles are shown.

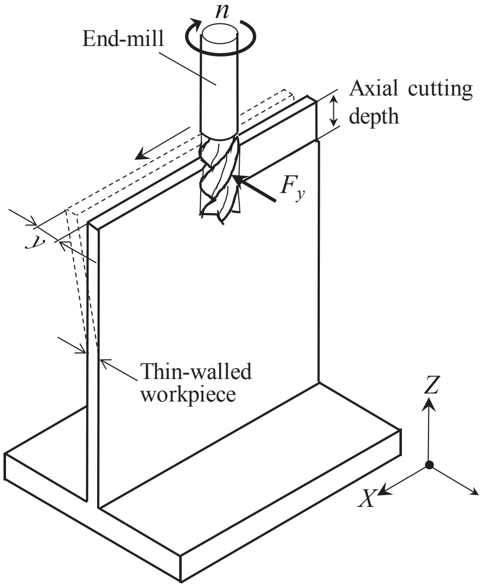

(a) Workpiece displacement of thin-walled workpiece caused by cutting force.

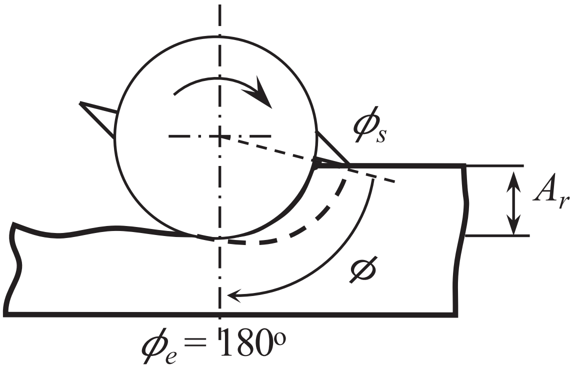

(b) Tool's rotational angle during milling.

Fig. 4.4. Side milling of thin-walled workpiece.

The uncut chip thickness h in milling varies periodically as the function of tool's rotational angle and it can be expressed as [54]:

$$h = f_t \sin(\phi) \tag{4.15}$$

where f_t is the feed per tooth.

Uncut chip thickness is zero when $\phi = 0$ (start angle for up-milling) and 180 deg. (exit angle for down-milling) and maximum when $\phi = 90$ deg. **Figure 4.4(b)** shows variation of chip thickness for down-milling operation. As can be seen from this figure, the chip thickness decreases in down-milling and it is zero for 180 ≤ ϕ ≤ 360 deg. because no cutting occurs between these angles. In down-milling operation, the start angle ϕ_s is a function of the radial cutting depth A_r and tool radius r_a (see **Fig. 4.4(b)**) which can be expressed as;

$$\phi_s = 180 - \cos^{-1}\left(\frac{r_a - A_r}{r_a}\right) \tag{4.16}$$

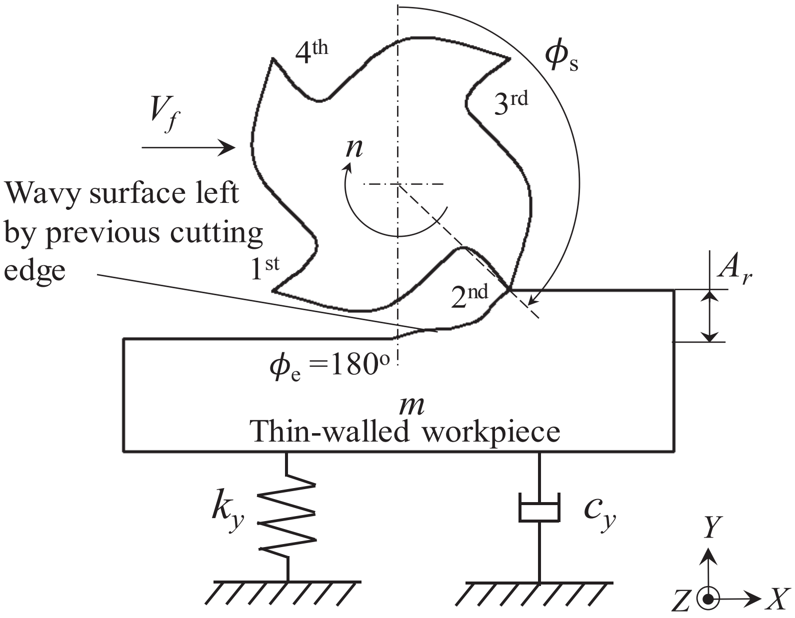

Fig. 4.5. Vibration model for down-milling of thin-walled workpiece [55].

On the other hand, **Figure 4.5** shows a vibration model for thin-walled milling, which is considered in this research. This model is based on the ones in ref. [55] which consists of mass m, spring stiffness k, and damper c of the workpiece. Here, we use their model and assume that the workpiece is to be a flexible part with the vibration mode is a single-degree-of-freedom (SDOF) system because the influence of vibration in width-direction is small.

According to the **Fig. 4.5**, the wavy surface left behind cutting edge is caused by displacement when the cutting force excites the workpiece vibration. This wavy surface is then cut by next cutting edge with fluctuating radial cutting depth A_r. And, these cycles provide a feedback mechanism because the instantaneous chip thickness depends on both the current wave and the wavy surface left by the previous cutting edges. The variable chip thickness determines the cutting force which affects subsequent workpiece displacement.

The stability chatter model as proposed by Altintas and Budak [55] is used in this study. And, the relationship between frequency response function and the stable limit of milling model is summarized below;

$$\mathrm{Re}\left[G_{yy}\left(j\omega_c\right)\right] = \frac{2\pi}{N_t K_t A_{a\lim}\alpha_{yy}} \qquad (4.17)$$

where N_t, K_t, A_{alim} are the number of tooth, tangential cutting force coefficient, and maximum axial depth of cut for chatter free machining, respectively. And, α_{yy} is the directional milling coefficient in the *y*-direction, which is obtained by the integrating between start ϕ_s and exit ϕ_e angles in Eq. 4.16 when the cutting edge enters and exits the cutting zone (see **Fig. 4.6**);

$$\alpha_{yy} = \left[\frac{1}{2}\left(-\cos\left(2\phi\right) - 2K_r\phi - K_r\sin\left(2\phi\right)\right)\right]_{\phi s}^{\phi e} \qquad (4.18)$$

where K_r is the radial milling force coefficient.

Using the real part of FRF and Eq. (4.15), the axial stability limit is obtained as follows:

$$A_{a\lim} = \frac{2\pi k}{N_t K_t \alpha_{yy}}\left(\frac{\left(1-r^2\right)^2 + \left(2.\zeta.r\right)^2}{1-r^2}\right) \qquad (4.19)$$

The spindle speed n (min^{-1}) is expressed by using the tooth passing period P (s) as;

$$n = 60/N_t P = 60\omega/N_t(\pi - 2\Psi + 2l_b\pi) \qquad (4.20),$$

where l_b is integer (= 0, 1, 2, …). In this equation, $\Psi = \tan^{-1}\{-2\zeta r/(1-r^2)\}$ is the phase shift. And substituting it into Eq. (4.20), it yields;

$$n = 60\omega_c/N_t\left\{\pi + 2l_b\pi - 2\tan^{-1}\left(\frac{2\zeta r}{r^2-1}\right)\right\} \qquad (4.21)$$

Calculating Eqs. (4.19) and (4.21) with changing the frequency ratio $r = \omega/\omega_c$ for arbitrary integer l_b, stability limits of the axial cutting depth A_{alim} and spindle rotation n are derived both. On a plane configured with two axes of the axial depth of cut and the spindle rotational speed, we plot the calculated results to obtain a stability lobe for an arbitrary integer l_b. Repeating above procedure in this study, the SLD was obtained.

4.4. Brief Theory of Experimental Modal Analysis Method for Dynamic Cutting System Identification

The dynamic modal parameters (*m, c,* ζ*,* and *k*) discussed in previous sections must be measured through hammering tests to create stability lobe diagram (SLD). SLD was then used to determine the cutting condition of machining tests. The modal parameters can be determined using experimental modal analysis (EMA) technique just after hammering test. So that, the purpose of the EMA is to extract the signals obtained in hammering test to be modal parameters.

Figure 4.6 shows real and imaginary part of FRF obtained by hammering test for milling. This figure is used for demonstrating the EMA method. As shown in figure, the FRF clearly contains single mode within the observed frequency bandwidth. Initially, three frequencies and one peak value for each mode are identified. The frequencies are labeled f_1 and f_2 along the frequency axis in the real part of FRF, and natural frequency f_n correspond to the negative peak value A in imaginary part of FRF.

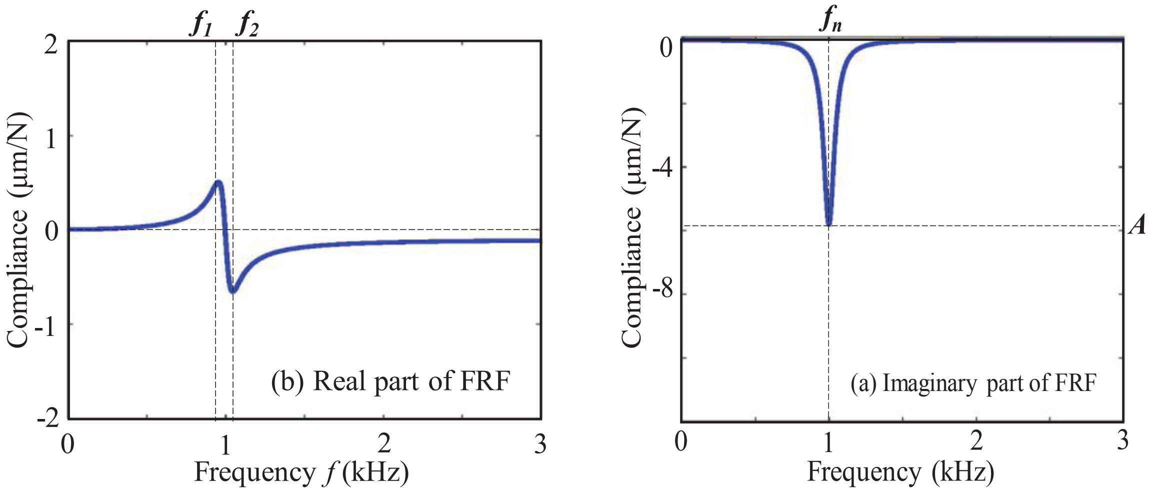

Fig. 4.6. Frequency response function (FRF); (a) Real part and (b) Imaginary part of FRF.

Following, the modal damping ratio ζ can be determined using;

$$\zeta = \frac{f_2 - f_1}{2\,fn} \qquad (4.20)$$

The negative peak value A in the imaginary part of the FRF is then used to find the modal stiffness value k;

$$k = \frac{-1}{2\zeta A} \qquad (4.21)$$

Next, the modal mass m can be determined using modal stiffness and the natural frequency;

$$m = \frac{k}{f_n^2} \qquad (4.22)$$

The modal damping coefficients c are calculated using the modal damping ratio, stiffness, and mass values as follows;

$$c = 2\zeta\sqrt{km} \qquad (4.23)$$

4.5. Summary

In this chapter, analytical methods are presented in stability lobe diagram for turning and end milling operations. The analytical based on the previous study by Altintas et al. In analytical model, the dynamic modal parameters; mass, damping, and stiffness are needed. Therefore, a brief theory of experimental modal analysis method is also provided for extracting those modal parameters from the signal obtained in hammering tests.

Chapter 5

Experimental Methods

5.1. Machine Tool, Workpiece, and Cutting Tool

5.1.a. Turning of thin-tubular workpieces

Machine tool used in turning tests was ANNYANG lathe machine. The work-material was AISI 1045 steel. This work material is widely used in studies and industries [65,66]. The dimension of the workpiece is shown in **Fig. 5.1**. As can be seen in the figure, the workpiece includes solid and thin-tubular structures with 200 mm in total length; 50 mm is solid structure and 150 mm is thin-tubular structure. The outer diameter is 38 mm and the inner diameter d_I depends on the wall-thickness t. And, $t = 3$ and 5 mm were used in turning tests. As shown from the **Fig. 5.1**, workpiece is clamped on solid structure using three-jaw chuck and thin-tubular structure is free clamped. The workpieces were machined using carbide tool in straight turning.

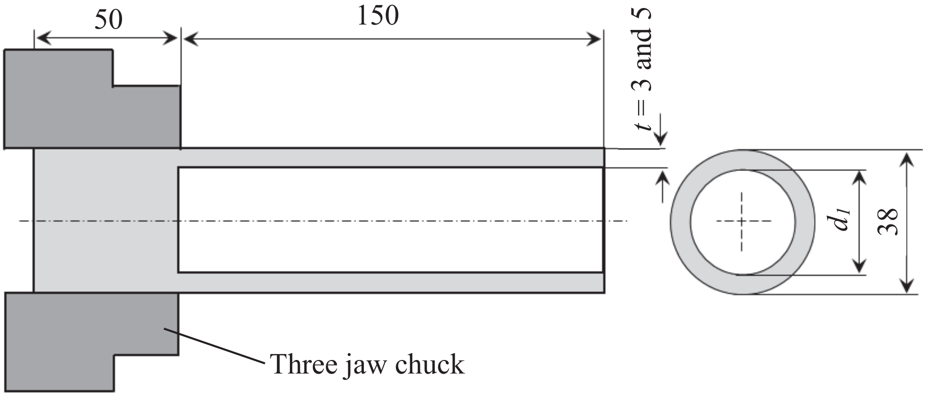

Fig. 5.1. Dimension of thin-tubular workpieces.

5.1.b. Milling of thin-walled workpieces

Machine tool used in milling tests was Shizuoka ST-NR of 3 axes knee type CNC milling machine whose specifications are given in **Table 5.1**. The work materials used were aluminum alloys with chemical composition are given in **Table 5.2**. The material was widely used in researches [67,68] and industries [69,70]. The workpieces were thin-walled plates with dimension of 100 x 100 x 3 (mm), and side milling was performed using square end-mills of HSS-Co. Specifications of end-mill tool used are given in **Table 5.3**. The tool overhang was 45 mm and the tool was more rigid than the workpiece. The thin-walled milling tests were carried out in the Laboratory of Machining and Machining Systems, Graduate School of Engineering, Hiroshima University, Japan.

Table 5.1. Specification of milling machine [71].

Controller	Fanuc CNC control
Maximum speed of rotation n (min^{-1})	6000
Maximum feed rate V_f (m/min)	3000 (X-Y) and 2000 (Z)

Table 5.2. Chemical composition of aluminum alloys [72].

Cu	Mg	Zn	Mn	Si	Fe	Cr	Ti
0.15 – 0.4	0.8 – 1.2	0.25_{max}	0.15_{max}	0.4 – 0.8	0.25_{max}	0.04 – 0.35	0.15_{max}

Table 5.3. Specification of end-mill tool.

Terminology	Dimension
Diameter $\varnothing$ (mm)	12
Total length L (mm)	80
Helix angle b (degree)	45
Number of tooth N_t	4

5.2. Dynamic Cutting System Identification

5.2.1. Hammering test in turning and milling

Figure 5.2 shows the hammering test setup in turning schematically. Here, dynamic behavior of the workpiece was measured because it was the most flexible in mechanical structure of this study. **Figure 5.2(a)** shows the apparatus used in the test. As shown in the figure, the workpiece is excited using a Dytran hammer. The impulse force of hammer is measured by force transducer which is mounted in the tip of hammer. Besides, response signals are measured by B&K accelerometer sensors which are mounted in the workpiece. Both of impulse force of hammer and response signals are acquired by using PICO oscilloscope. The personal computer with Pico-scope shows the waveform of those vibrations which were collected as the data. The impact techniques are conducted as shown in **Fig. 5.2(b)**. Here, workpiece is excited in x and y directions. When hammer excites workpiece in the direction of either x or y, then the response will be measured, namely; $G_{xx}(\omega)$ and $G_{yy}(\omega)$.

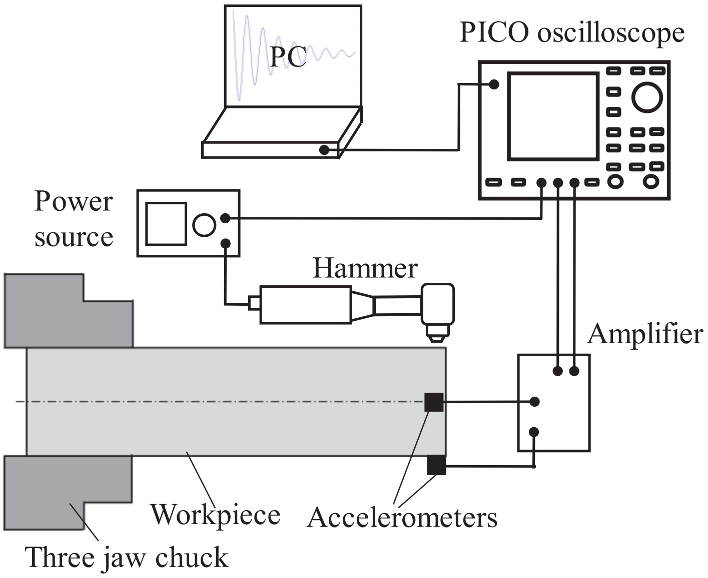

(a) Apparatus used in experimental hammering test.

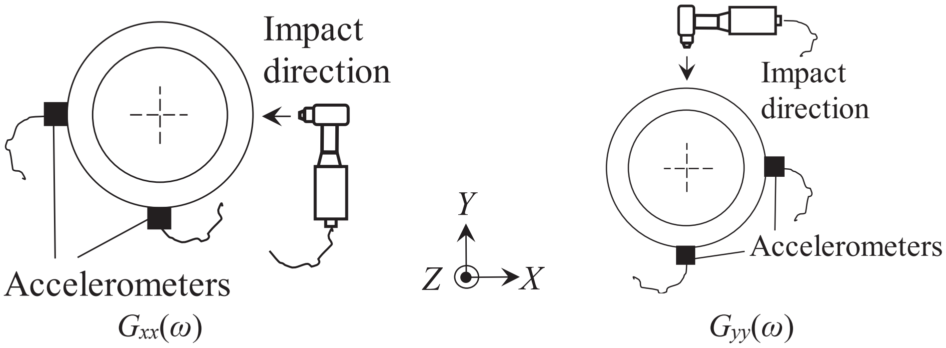

(b) Impact techniques.

Fig. 5.2. Hammering test setup in thin-tubular workpieces.

Besides, in milling of thin-walled workpieces, the dynamic behavior of the workpiece is usually limiting factor for the machining process because they have low stiffness, damping and the most flexible component in the process. Therefore, the thin-walled workpiece needs to be modelled as being flexible. And in this case, FRF is measured in y-direction as shown in **Fig. 5.3**. As can be seen in **Fig. 5.3**, the structure is hit by a Dytran 5850 hammer in y-direction. The acceleration response is measured by the accelerometer sensor and it is acquired by a data storage system; Yokogawa DL750 with sampling rate of 100 kHz.

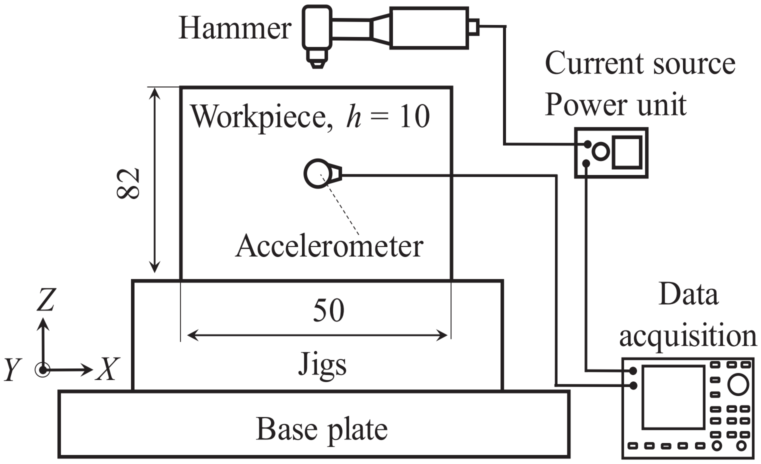

Fig. 5.3. Hammering test setup in thin-walled plate.

In hammering tests, the obtained signals should be examined to identify whether it was a bad or good hit. A hit is considered bad if a multiple hit occurred. This phenomena is called "bouncing effect". It means the hammer bounces, loses contact and hits the structure twice or more. A bouncing effect can easily be detected in oscilloscope and this signal has to be rejected. In this study, FRF was just calculated using signal with good hit. The FRF gave dynamic cutting system information in certain frequency. In calculating FRF, the frequency spectrum of the acceleration signal needs to be integrated twice in order to get displacement.

5.2.2. Identification of dynamic cutting system by EMA method

Figure 5.4 shows the signals in time-domain obtained in hammering test of thin-walled plate. **Fig. 5.4(a)** shows the impulse force and **Fig. 5.4(b)** shows the acceleration response. The signal of the hammer shows no second hit, and therefore no bouncing effect has been occurred.

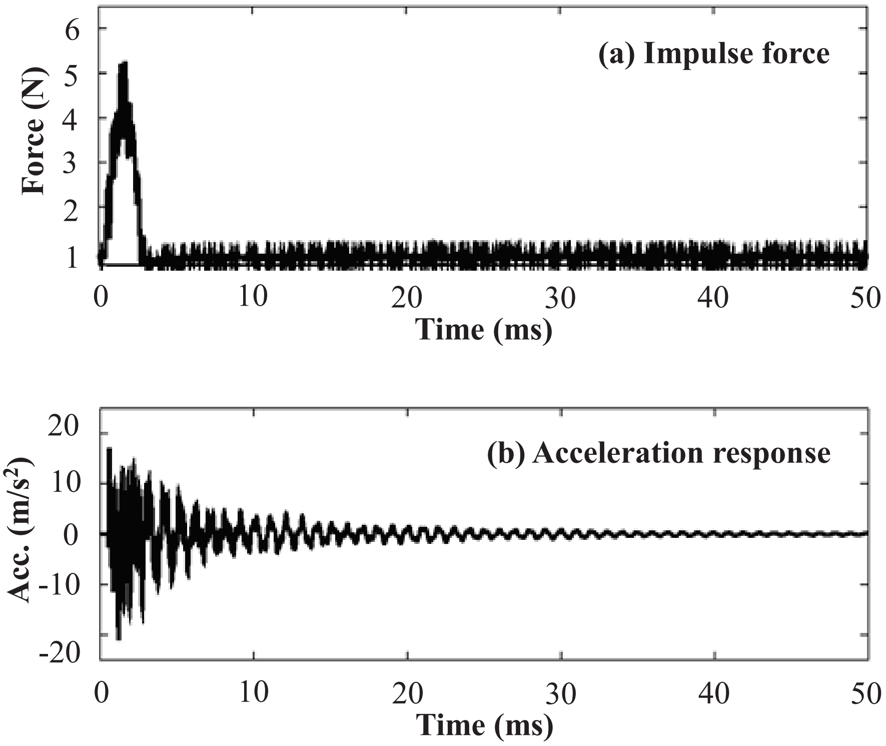

Fig. 5.4. Raw data in time-domain of hammering test; (a) Impulse force and (b) Acceleration response.

On the other hand, **Figure 5.5** shows frequency spectra of hammering test obtained by FFT. The cutting system contains natural frequency of 1 kHz. So that cutting phenomena could be identified in this frequency. Following, the frequency response function (FRF) was determined by combining the Fourier spectra of displacement (**Fig. 5.5(b)**) divided by the impact force (**Fig. 5.5(a)**) [51], and the result is shown in **Fig. 5.6**. The real & imaginary parts of the FRF are shown in these figures. By using these curves, the experimental modal analysis (EMA) technique explained in **Section 4.5** was performed to estimate the modal parameters.

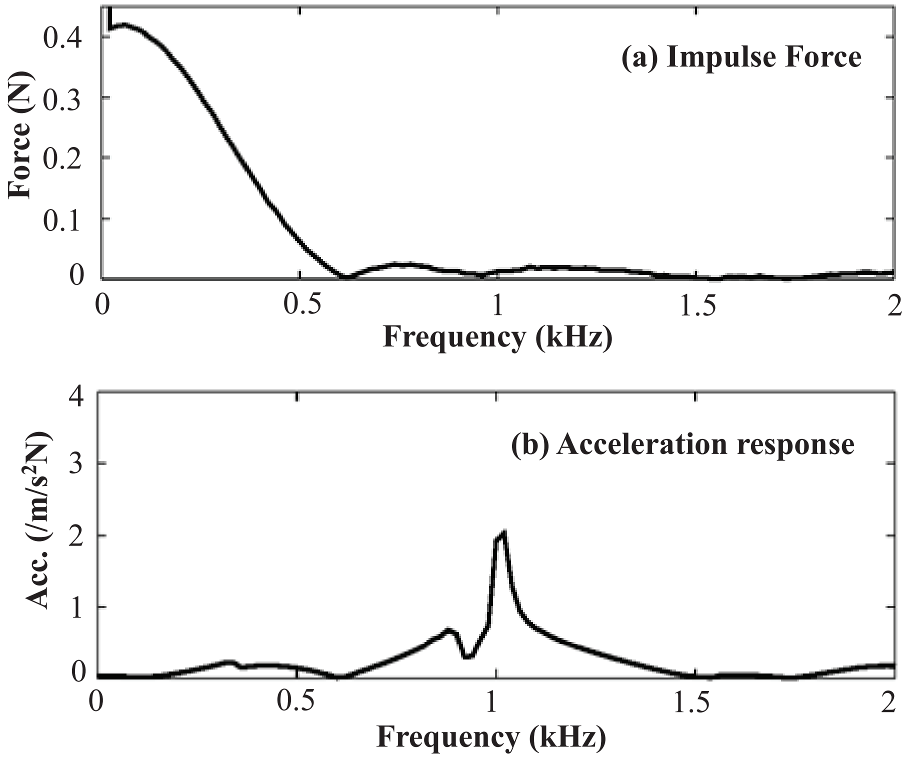

Fig. 5.5. Frequency spectra of hammering test; (a) Impulse force and (b) Acceleration response.

Figure 5.6(a) shows the real part of FRF which contains two the highest peaks at specific frequencies f_1 and f_2. And in **Fig. 5.6(b)** shows imaginary part one which the negative peak value A is identified for natural frequency f_n. According to these values; f_1, f_2, f_n and B, the modal parameters can be determined, including modal damping ratio ζ, stiffness k, mass m, and damping coefficient c of the workpiece. And the dynamics modal parameters for thin-walled plate obtained in above test are shown in **Table 5.4**. On the other hand, **Table 5.5** shows for thin-walled tubular workpiece one.

Table 5.4. Dynamic modal parameters of thin-walled plate.

FRF Direction	Natural frequency f_n (kHz)	Damping ratio ζ (%)	Stiffness k (N/μm)
G_{yy}	1	4.5	1.92

Table 5.5. Dynamic modal parameters of thin-turbular workpieces.

Wall thickness t (mm)	FRF Direction	Natural frequency f_n (Hz)	Damping ratio ζ (%)	Stiffness k (N/μm)
3	G_{xx}	55	6.6	0.25
	G_{yy}	53	1.1	0.266
5	G_{xx}	78	5.6	0.355
	G_{yy}	84	1.05	0.28

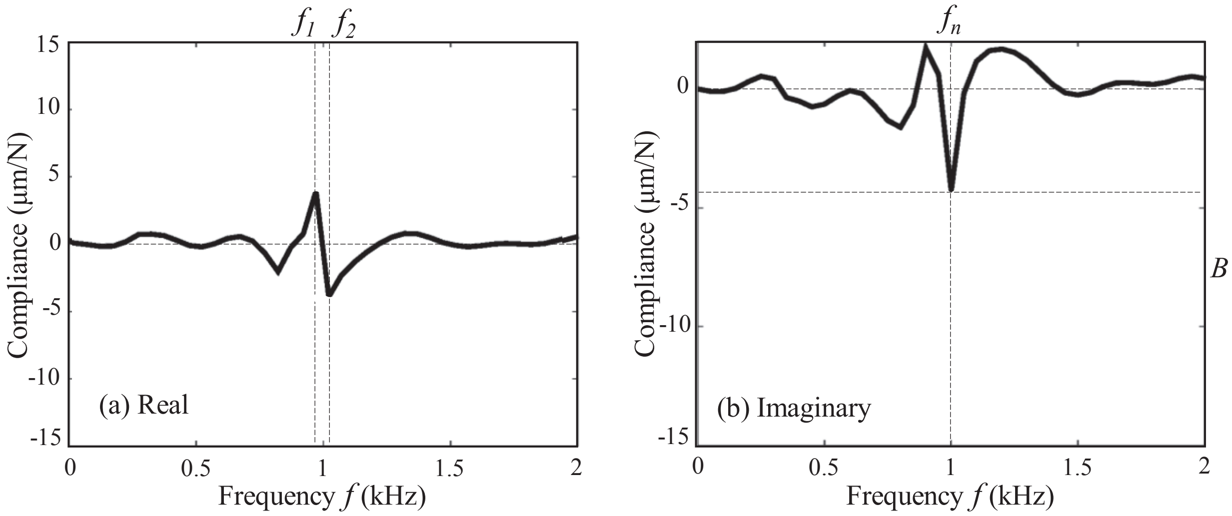

Fig. 5.6. Frequency response function (FRF) of thin-walled plate; (a) Real and (b) Imaginary parts of FRF.

5.2.3. Generating stability lobe diagram for turning and milling

The stability lobe diagrams (SLDs) were generated to determine the cutting conditions prior to machining tests. The SLD shown in **Fig. 5.8** is result for thin-tubular workpiece using modal parameter in **Table 5.5** and cutting force coefficient $Ks = 2600$ N/m^2 [73]. Here, dotted curves are lobes for thickness of thin-tubular $t = 3$ mm. Besides, solid lobes are for $t = 5$ mm. On the other hand, the SLD shown in **Fig. 5.7** is result for down-milling using the modal parameters in **Table 5.4**, tooth number of end-mill $N_t = 4$, and radial cutting depth A_r of 0.5 mm. Besides, the tangential $K_t = 7.96 \times 10^8$ N/m^2 and radial $K_r = 1.68 \times 10^8$ N/m^2 cutting force coefficients which result of Jin et al. was also used [74]. In our analytical SLD, we obtained 26 lobes ($l_b = 0, \ldots 25$) for spindle rotation of 550 to 7000 min^{-1}. **Figure 5.7** shows 14 lobes for spindle rotation of 1000 to 7,000 min^{-1}.

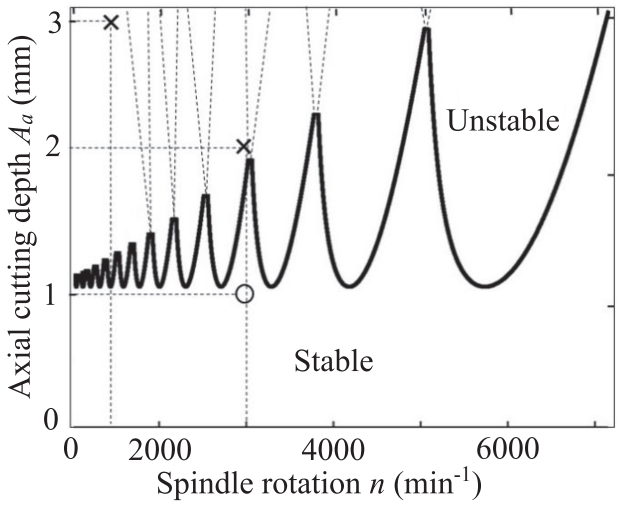

Fig. 5.7. Stability lobe diagram for selecting cutting conditions in milling.

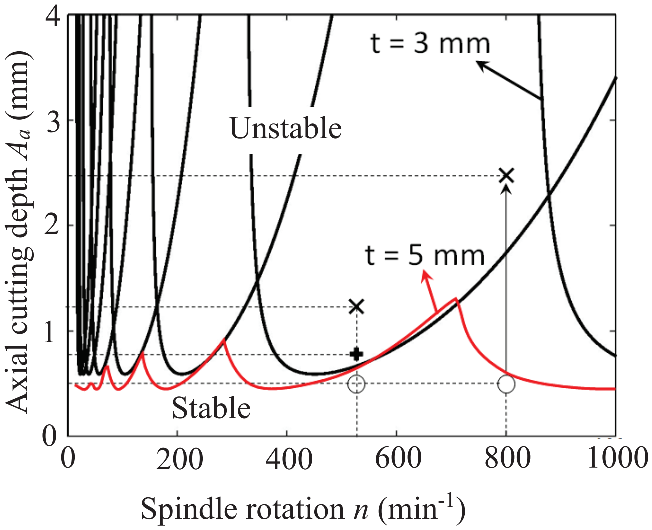

Fig. 5.8. Stability lobe diagram for selecting cutting conditions in turning.

5.3. Tests for Chatter Detection in Turning of Thin-Tubular Workpieces

In experimental turning tests, the cutting parameters were determined using SLDs shown in **Fig. 5.7** for any pair of axial cutting depth A_a and rotational speed of spindle n. In detail, the cutting parameters are shown in **Table 5.6** for turning of thin-tubular workpieces with t = 3 and t = 5 mm. Based on this table, turning tests for thin-tubular workpiece with t = 3 mm will be conducted in the three cutting states, namely; stable (A_a = 0.5 mm), slight chatter (A_a = 0.8 mm), and severe chatter (A_a = 1.2 mm) with the same of spindle rotational speed n = 550 min^{-1} and feed/revolution ft = 0.06 mm/rev. On the other hand, the axial depth of cut for turning test with t = 5 mm will be gradually increasing from A_a = 0.5 – 2.5 mm with constant spindle rotational speed n = 800 min^{-1} and f_t = 0.06 mm/rev.

Besides, **Figure 5.9** shows the experimental turning setup. Based on this figure, the acceleration signal is measured by accelerometer sensor which is mounted in the tool holder and then acceleration was acquired by a data storage system; PICO oscilloscope.

Table 5.6. Cutting condition for observing chatter in thin-tubular turning tests.

No.	t (mm)	f_t (mm/rev)	n (min^{-1})	A_a (mm)	Cutting states
1	3	0.06	550	0.5	Stable
2				0.8	Slight chatter
3				1.2	Severe chatter
4	5	0.06	800	0.5-2.5	Stable to chatter

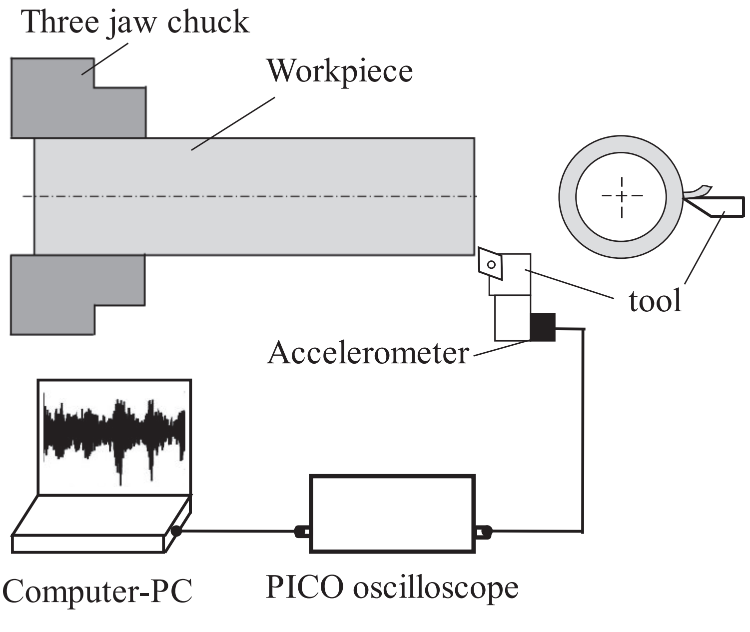

Fig. 5.9. Turning test setup for observing chatter.

5.4. Milling tests

5.4.1. Chatter detection in thin-walled milling

Chatter is important topic in machining dynamic research. Because (1) chatter is a highly complex phenomenon due to the diversity of elements that can compose the dynamic system, i.e. cutting tool, tool holder, work material, and the machine tool structure [75]. (2) The negative effects of chatter which lead to poor surface quality, dimensional error in the machine part and accelerate tool failure too [76]. Therefore, in the first milling tests, this study concerns to monitor the milling states by observing the chatter.

In these tests, the SLD shown in **Fig. 5.7** was used for determining the cutting conditions; both of axial cutting depth A_a and spindle rotation n. According to the diagram, $A_a = 1$ mm and $A_a = 2$ mm correspond to $n = 3000$ min^{-1} were chosen to conduct the tests under stable ("⊙" symbol) and unstable ("×" symbol) conditions. The experimental setup is shown in **Fig. 5.10** and cutting conditions are in **Table 5.7**. Based on the **Fig. 5.10**, the acceleration signal was measured by accelerometer sensor and then acceleration signal was acquired by a data storage system; Yokogawa DL750 in down-milling.

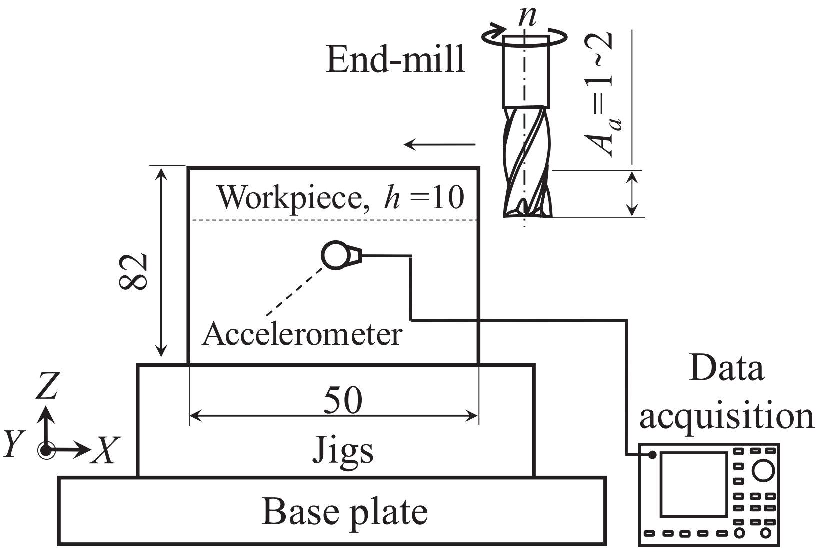

Fig. 5.10. Milling test setup for observing chatter.

Table 5.7. Cutting conditions for observing chatter thin-walled milling.

No.	Spindle rotation n (min^{-1})	Feed rate V_f (mm/min)	Depth of cut (mm)	
			Axial A_a	Radial A_r
1	3000	960	1	0.5
2	3000	960	2	0.5

5.4.2. Sudden change of machining stability caused by lubrication in thin-walled milling

Cutting fluid improves the surface finish quality of workpieces and extends tool life. Many scholars have investigated the effect of cutting fluid on machining process [77-80] but few focused to the effect of cutting fluid on vibration and especially for flexible part. Therefore, in the second experiment, we conducted dry and wet milling test to compare the results of vibration analysis for signals obtained in both conditions.

This test was conducted in unstable condition shown in **Fig. 5.8** which was A_a = 3 mm and n = 1200 min^{-1} (see "×" symbol in **Fig. 5.8**). In this test, some oil was put on the cutting path of the workpiece and it allowed reducing the cutting resistance during milling process to inhibit the cutting instability. The oil areas are shown in **Fig. 5.11**. As can be seen from the figure, the vibration is measured using accelerometer sensor and strain-gauge and then they are acquired by data storage, Yokogawa oscilloscope. Besides, **Table 5.8** shows cutting conditions for this milling test in detail.

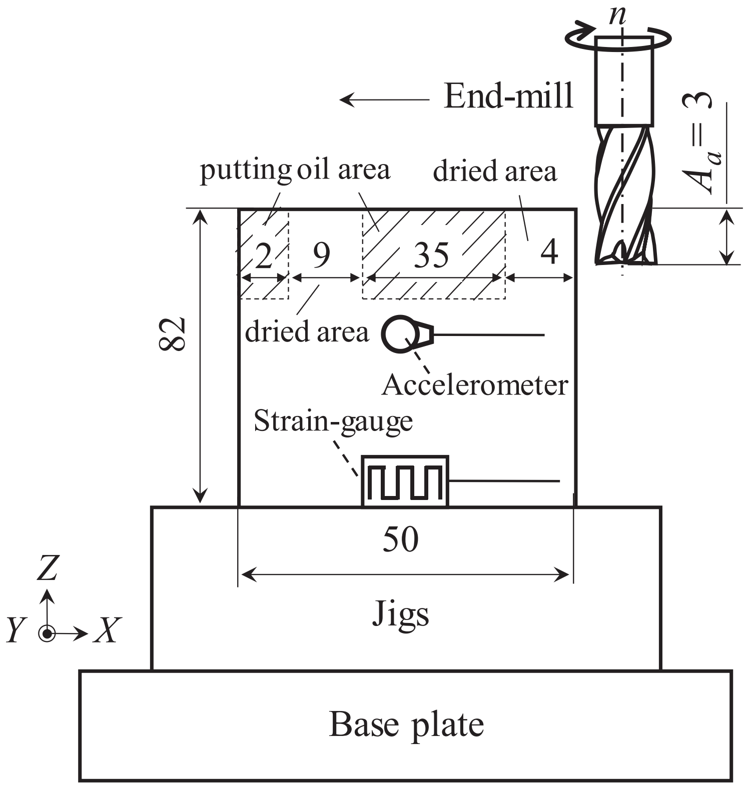

Fig. 5.11. Milling test setup for observing sudden change of machining stability caused by lubrication.

Table 5.8. Cutting conditions for observing sudden change of machining stability caused by lubrication.

Spindle rotation n (min^{-1})	Feed rate V_f (mm/min)	Depth of cut (mm)	
		Axial A_a	Radial A_r
1200	30	1	0.5

5.4.3. Sudden change of machining stability caused by obstacle in thin-walled milling

Similar to the sudden change in lubricant condition, the cutting stability can also be disturbed by the biting different material such as work-hardened chips, inclusions in metal and so on. Therefore, we tested a milling for materials including an obstacle. The goals are to demonstrate the reliability of HHT to detect the obstacle in milling and to observe the sudden change of machining stability caused by milling with obstacle.

In this test, to simulate a milling process that facing an obstacle during operation, the workpiece was set up for activating the obstacle in thin-walled milling as shown **Fig. 5.13**. Here, the main work material is aluminum and an M4 screw bolt of steel is put in the middle of cutting path and stand out to above little. As can be seen from the **Fig. 5.13**, at the middle of cutting path, the tool encounters the steel suddenly, then the cutting stability drastically changes because of the difference in cutting force coefficient for two kinds of materials. From the **Fig. 5.13**, vibration is measured using accelerometer and strain-gauge sensors and then were acquired by data storage system of Yokogawa oscilloscope. Test was conducted in the stable region just below the SLD shown in **Fig. 5.12,** which is marked with the symbol "⊙". And the cutting conditions are presented in **Table 5.9**.

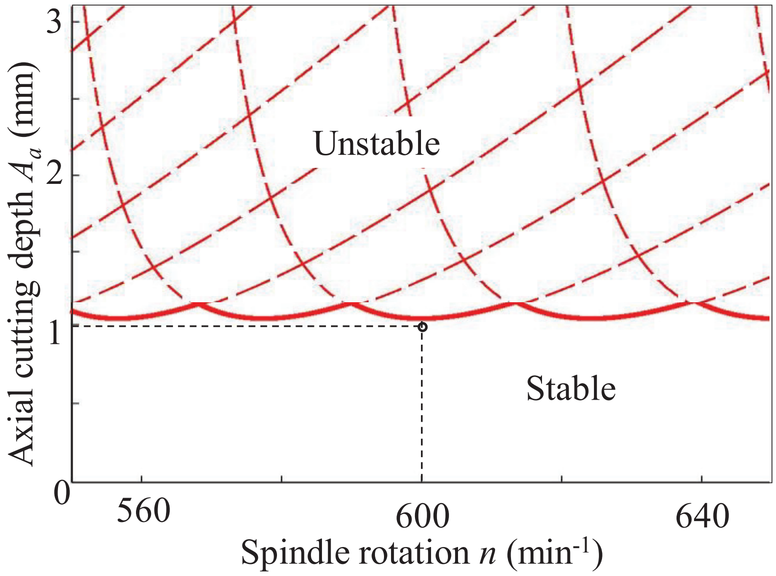

Fig. 5.12. Stability lobe diagram for selecting cutting conditions.

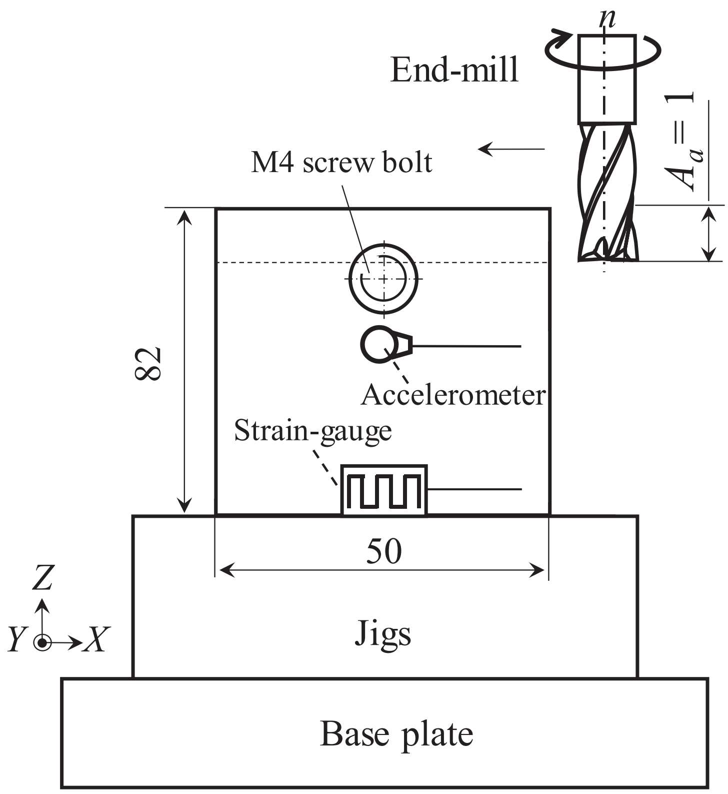

Fig. 5.13. Workpiece condition for activating obstacle in milling.

Table 5.9. Cutting conditions for observing sudden change of machining stability caused by obstacle in thin-walled milling.

Spindle rotation n (min^{-1})	Feed rate V_f (mm/min)	Depth of cut (mm)	
		Axial A_a	Radial A_r
600	120	1	0.5

5.4.4. Tool condition monitoring

In the following test, we monitored the tool condition. Because, tool is one of important elements in machining operation. In these tests, three kinds of end-mills with different cutting-edge conditions were used and the influence of those conditions was investigated. **Figure 5.14** shows the microscopic photograph of end-mill cutting edges. **Figure 5.14(a)** is the end-mill body with four flutes in normal condition. The magnified cutting edge of this tool is shown in **Fig. 5.14(b)**. **Figure 5.14(c)** shows the cutting edge of worn tool which was simulated by grinding-down the one of teeth but retaining cutting ability of the tooth. The condition of worn tool was similar to flank wear. It means that the grinding-down cutting edge was contacting with the workpiece during milling. **Fig. 5.14(d)** shows chipped tool. The chipped tool was simulated by grinding one of the teeth completely, and the ground tooth was unable to cut the workpiece. Milling tests were conducted in stable area of the SLD shown in **Fig. 5.12** with same feed rate v_f (120 mm/min) and radial cutting depth A_r and cutting conditions are shown **Table 5.10** in detail. As can be seen from the table, axial cutting depth $A_a = 1$ mm corresponds to spindle rotation $n = 600$ min^{-1} was chosen as the cutting condition. On the other hand, setup for these milling tests is shown in **Fig. 5.15**. Here, vibration was measured using strain gauge.

Table 5.10. Cutting conditions for tool condition monitoring.

No.	Spindle rotation n (min^{-1})	Feed rate V_f (mm/min)	Depth of cut (mm)		Tool condition
			Axial A_a	Radial A_r	
1	600	120	1	0.5	Normal
2	600	120	1	0.5	Wear
3	600	120	1	0.5	Chipping

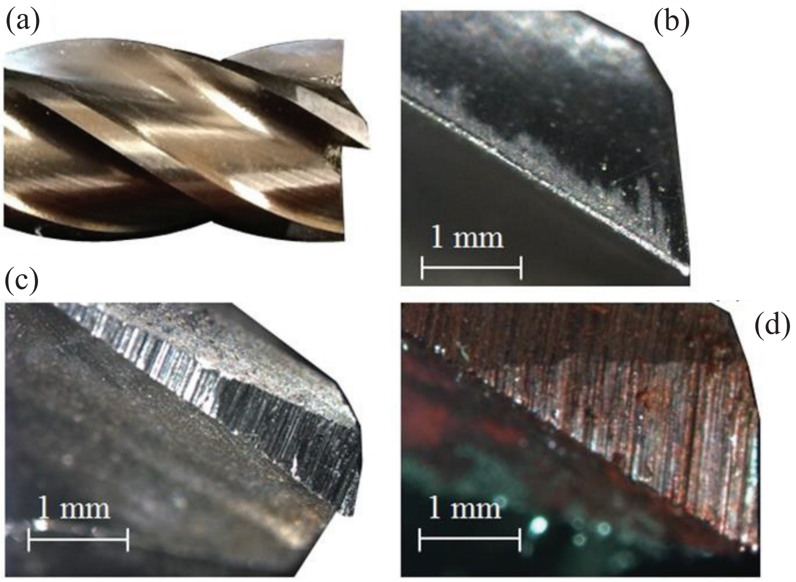

Fig. 5.14. Microscopic photograph of different cutting edges; (a) full end-mill body (b) normal, (c) worn, (d) chipped tools.

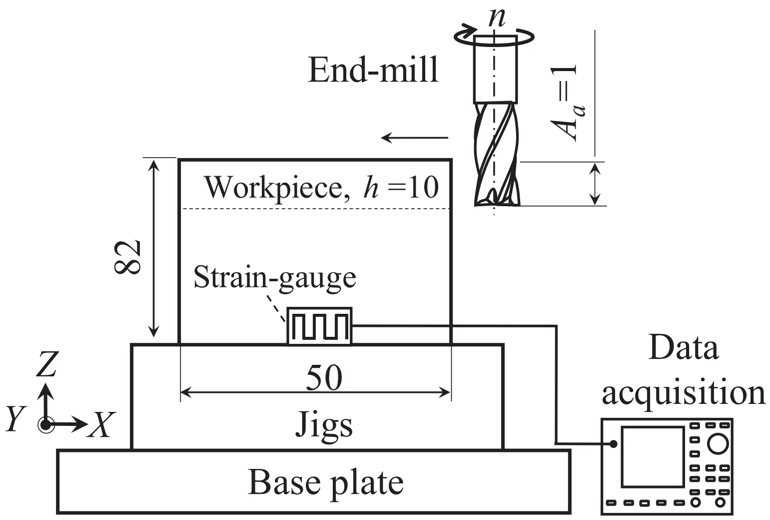

Fig. 5.15. Milling test setup for observing tool condition.

5.5. Summary

In this section, the experimental methods are explained, and they are summarized as follows;

- Machine tools, workpieces, and cutting tools are explained including for lathe and CNC milling machine tools. Steel, aluminum alloys work materials, and their dimension are explained. High-speed-steel cutting tool material and the specification is also explained.
- The procedures of hammering test for turning and milling process are provided. Wokrpieces are considered as the flexible part of machine structures, so that the workpieces are excited by hammer.
- For extracting the dynamic modal parameters; damping and stiffness, experimental modal analysis method was used.
- Stability lobe diagrams are generated for each turning and milling process to determine cutting conditions prior to machining tests.
- Cutting tests for turning and milling are also explained.

Chapter 6

Result and Discussion

The vibrations obtained in machining tests were analyzed in frequency-domain using Fast Fourier (FFT) and time-frequency domain using short-time Fourier (STFT) and Hilbert-Huang (HHT) transforms. The results are discussed in each section.

6.1. Chatter Detection in Turning of Thin-Tubular Workpieces

6.1.1. Time-domain signals obtained in turning tests

Figure 6.1.1 and **Fig. 6.1.3** show vibrations which were measured in turning under cutting parameter given in **Table 5.6**. **Figure 6.1.1** shows vibrations obtained in turning of thin-tubular workpieces with wall-thickness t = 3 mm and using different pair of axial cutting depth and spindle rotation. As can be seen from the figures, the vibration amplitudes are varying over the cutting period. **Figure 6.1.1(a)** is vibration obtained in stable operation and its amplitude is smaller than others and smooth during cutting period. The amplitude of vibrations becomes larger and chaotic in slight chatter and severe chatter operations as shown in **Fig. 6.1.1(b)** and **Fig. 6.1.1(c)**. Stable and chatter vibrations was imprinted in the machined surface of turning tests as shown in **Fig. 6.1.2**.

On the other hand, **Fig. 6.1.3(a)** shows transient vibration obtained in turning of thin-tubular workpieces with wall-thickness t = 5 mm. The transient vibration was caused by gradually increasing axial cutting depth (A_a = 0.5 – 2.5 mm) during the operation. As shown in the figure, the amplitude is small at beginning till 13 seconds of cutting period. This amplitude represents stable cutting (see magnified figure in **Fig. 6.1.3(b)**). And, the amplitude becomes transition and it is increasing as the cutting depth increase. The increasing amplitude indicates occurrence of chatter (see magnified figure in **Fig. 6.1.3(c)**). Furthermore, FFT, STFT, and HHT were utilized for analyzing vibrations shown to show the capability of these signal processing techniques for chatter identification.

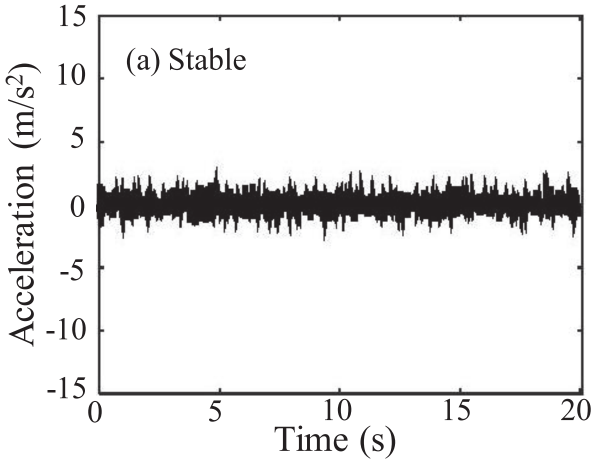

$A_a = 0.5$ mm, $n = 550$ min^{-1}

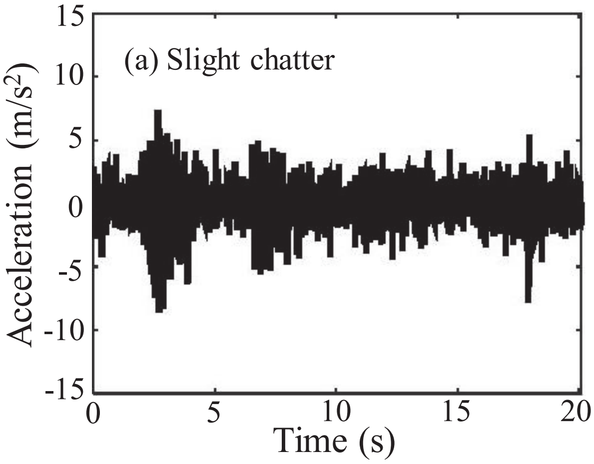

$A_a = 0.8$ mm, $n = 550$ min^{-1}

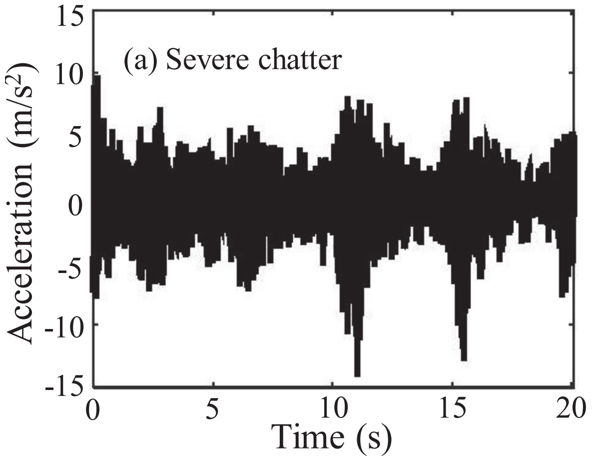

$A_a = 1.2$ mm, $n = 550$ min^{-1}

Fig. 6.1.1. Effect of different axial cutting depths on vibration in turning of thin-tubular workpieces with wall-thickness $t = 3$ mm.

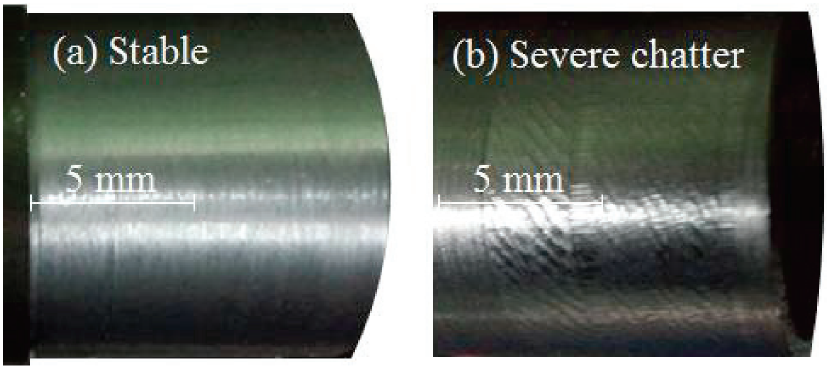

Fig. 6.1.2. Machined surfaces obtained in turning of thin-tubular workpieces for wall-thickness *t* = 3 mm.

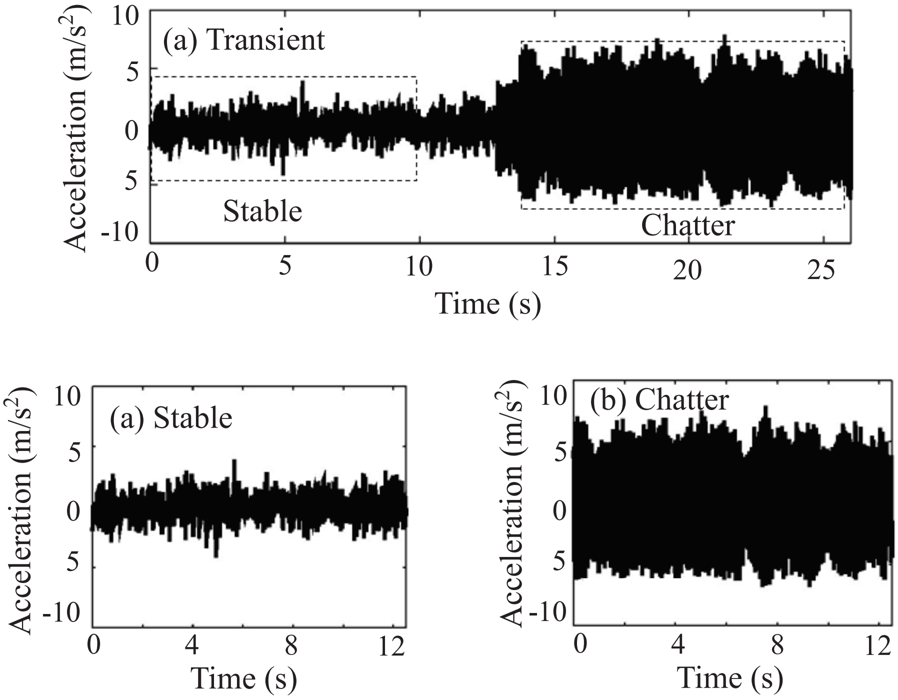

Fig. 6.1.3. Transient acceleration signal caused by gradually increasing of axial cutting depth in turning of thin-tubular workpiece with wall-thickness *t* = 5 mm.

6.1.2. Vibration analysis using FFT

Fast Fourier transform (FFT) was used to observe the frequency contents whether chatter occurs. The frequency spectrum obtained by FFT is shown in **Fig. 6.1.4** and **Fig. 6.1.5**. In **Fig. 6.1.4(a)**, rotational spindle frequency ($f_{sp} = n/60 = 9.2$ Hz) appears in this spectrum with small amplitude when stable turning using $A_a = 0.5$ mm. When the axial cutting depth was increasing with slight chatter turning operation, chatter frequency f_c appears at 49 Hz together with f_{sp} as shown in **Fig. 6.1.4(b)**. here, f_{sp} also appears in the spectrum when the turning operation is in severe chatter as shown in **Fig. 6.1.4(c)**, the chatter amplitude increases with largest amplitude at same chatter frequency and high amplitude and f_{sp} disappears in this case.

On the other hand, **Fig. 6.1.5** represents the frequency spectrum associated with transient acceleration signal shown in **Fig. 6.1.3**. **Fig. 6.1.5(a)** is the frequency spectrum for full vibration which is associated with signal shown in **Fig. 6.1.3(a)**. As shown in the figure, the chatter frequency f_c appears in this spectrum at 80 Hz. Besides, **Fig. 6.1.5(b)** is the frequency spectrum for stable cutting which is associated with signal shown in **Fig. 6.1.3(b)**. As shown in this figure, chatter frequency is vanished in this frequency spectrum. In addition, **Fig. 6.1.5(c)** is frequency spectrum for unstable operation which is associated with signal shown in **Fig. 6.1.3(c)**. As can be seen, chatter frequency f_c also appears in this frequency spectrum with higher amplitude than ones in **Fig. 6.1.5(a)**.

These results showed that FFT is unable to detect the frequency changes of transient signal. Therefore, FFT is not suitable for analyzing transient acceleration signal which its frequency changes over cutting period.

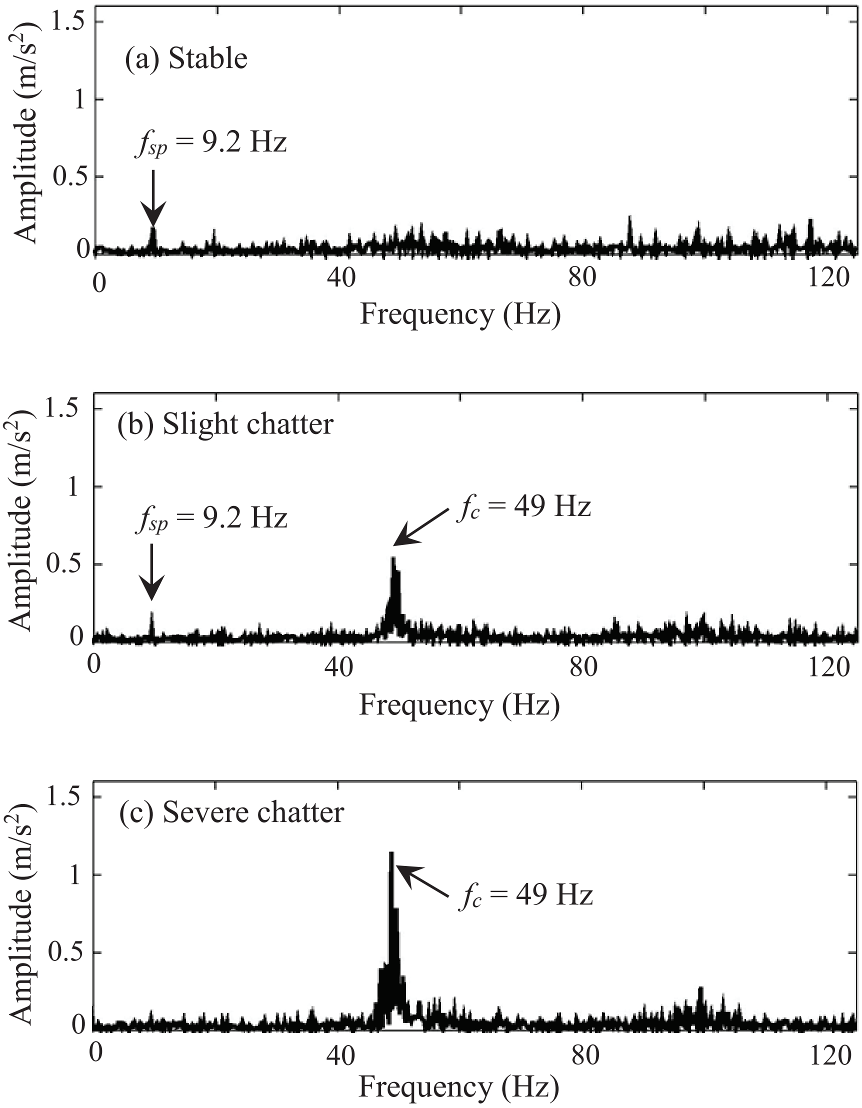

Fig. 6.1.4. Frequency spectra for three kinds of acceleration signals which correspond to vibrations in **Fig. 6.1.1**.

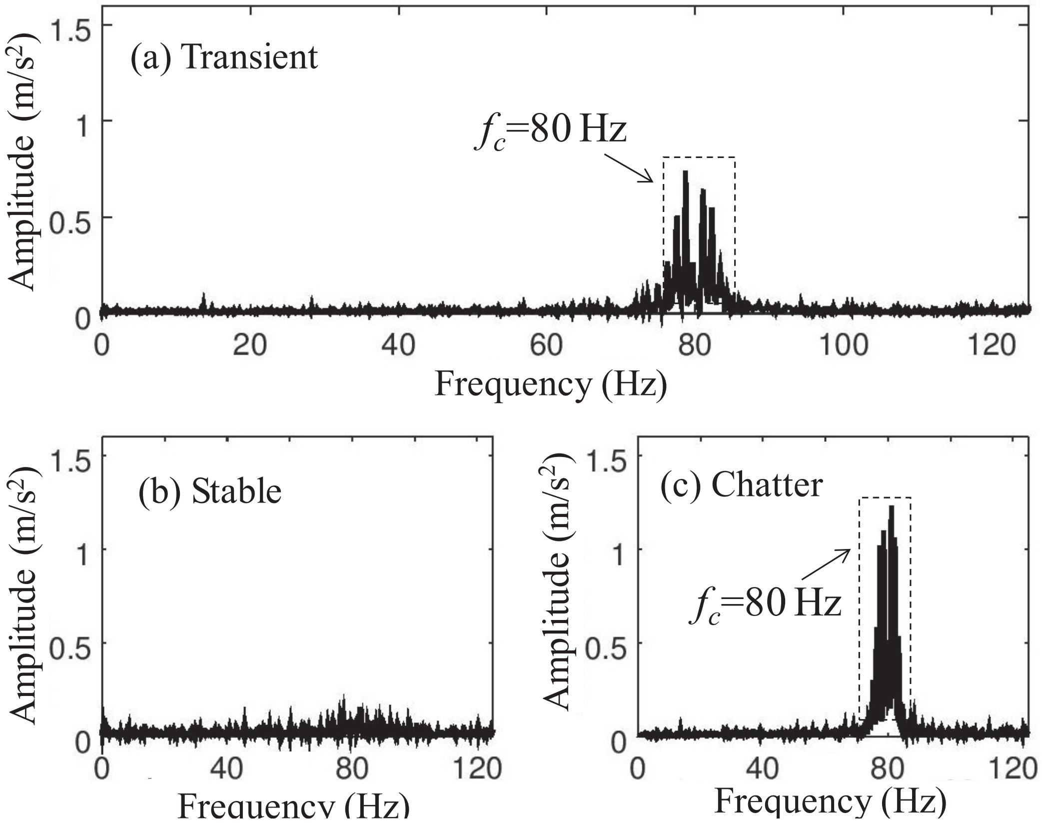

Fig. 6.1.5. Frequency spectra for transient signal obtained which correspond to vibrations in **Fig. 6.1.3.**

6.1.3. Vibration analysis using HHT and comparing with STFT results

The first step of HHT is applying EMD process to decompose raw signal to be a set of IMF components and some of the results are shown in **Fig. 6.1.6** and **Fig. 6.1.7**. **Figure 6.1.6(a)** and **Fig. 6.1.6(b)** are IMF components for stable and severe chatter vibrations which correspond to signals in **Fig. 6.1.1(a)** and **Fig. 6.1.1(c)**, respectively. Eight IMF components and a monotonic-residue were obtained for these cases. On the other hand, **Fig. 6.1.7** is a set of IMF components for transient acceleration signal which corresponds to signal in **Fig. 6.1.3(a)**. Here, Nine IMF components and a monotonic-residue were obtained for this case.

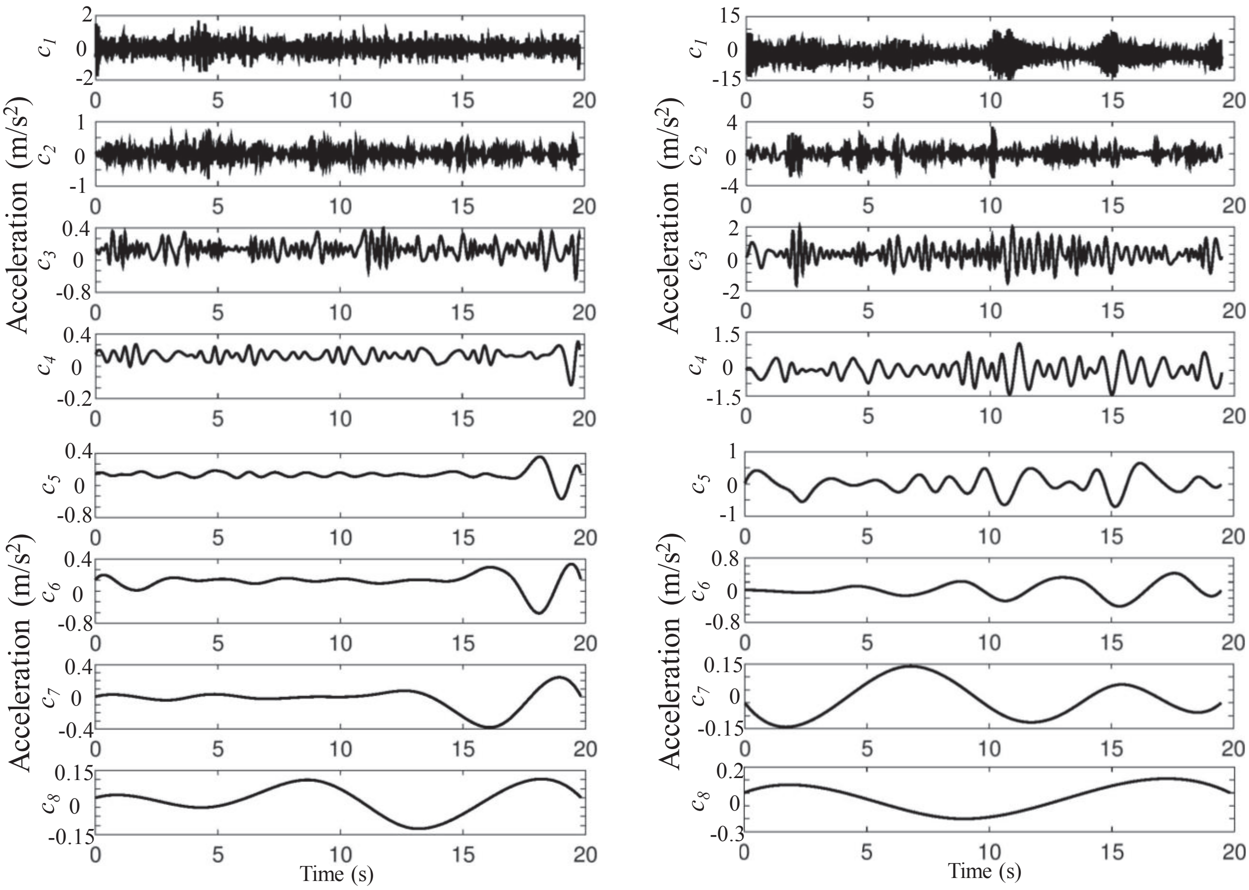

(a) IMF components for stable cutting corresponding to vibration in **Fig. 6.1.1(a)**

(b) IMF components for severe chatter corresponding to vibration in **Fig. 6.1.1(c)**

Fig. 6.1.6. IMF components in time-domain obtained by EMD process.

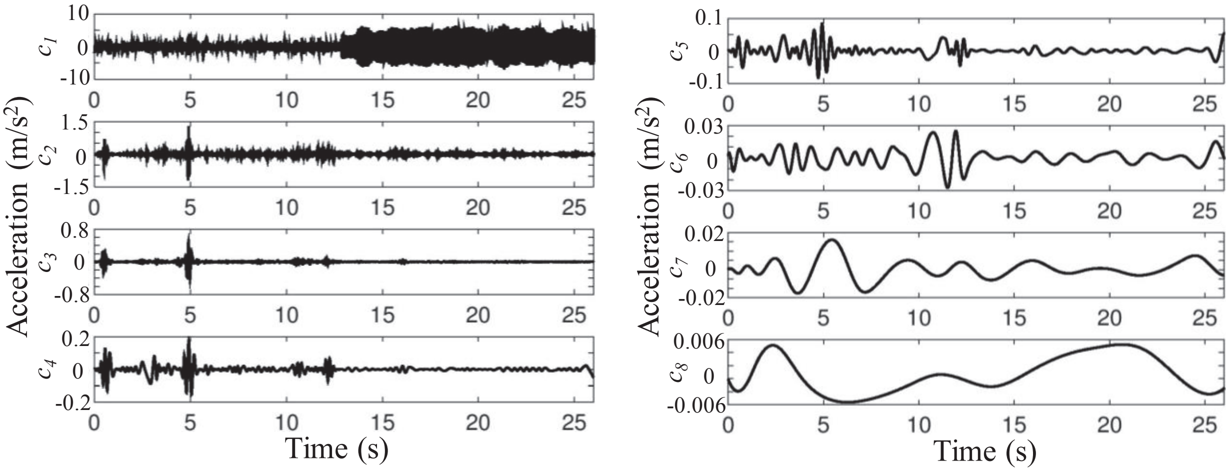

Fig. 6.1.7. IMF components for transient signal which correspond to vibration in **Fig. 6.1.3(a).**

As can be seen from the figures, each IMF component contains different oscillation and amplitude. For example, the first IMF c_1 contains the most oscillations, otherwise, the last IMF c_9 contains the least oscillations. Therefore, c_1 contains the highest frequency and c_8 contains the lowest frequency among all IMFs. And, monotonic-residue is just residual of the process so that it did not include significant vibration. Therefore, we did not show the monotonic-residue.

Next, we will inspect the first IMF c_1 for each case. As shown in the figures, first IMF c_1 captures the highest amplitude and oscillation among IMF components in turning test. The first IMF c_1 is in **Fig. 6.1.7**, especially. This IMF captures the transient signal. Therefore, the first IMF c_1 in each case contained a unique information of vibration mode obtained in experimental tests. To confirm that, the first – fourth IMF components in **Fig. 6.1.6** and **Fig. 6.1.7** both were examined by FFT to observe frequency content, and the results are shown in **Fig. 6.1.8** and **Fig. 6.1.9**. All the symbols in these figures have the same denotations as in **Fig. 6.1.4**.

Every characteristic frequency appears in particular IMF of **Fig. 6.1.8** and **Fig. 6.1.9** with different amplitude. It also should be noted that each IMF component contains one unique frequency, which means that the sifting process by EMD decomposed the complex vibration into simple components. In **Figure 6.1.8(a)** which is associated with stable cutting, the first IMF c_1 just contains rotational spindle frequency. Besides, **Figure 6.1.8(b)** which is associated with severe chatter, the first IMF c_1 and the forth IMF include the chatter and rotational spindle frequencies at f_c = 49 Hz and f_{sp} = 9.2 Hz, respectively. On the other hand, **Figure 6.1.9** represents the IMF in frequency domain which associated with IMFs in **Fig. 6.1.7**. As shown in figure, chatter frequency appears in the first IMF c_1 and was separated from others.

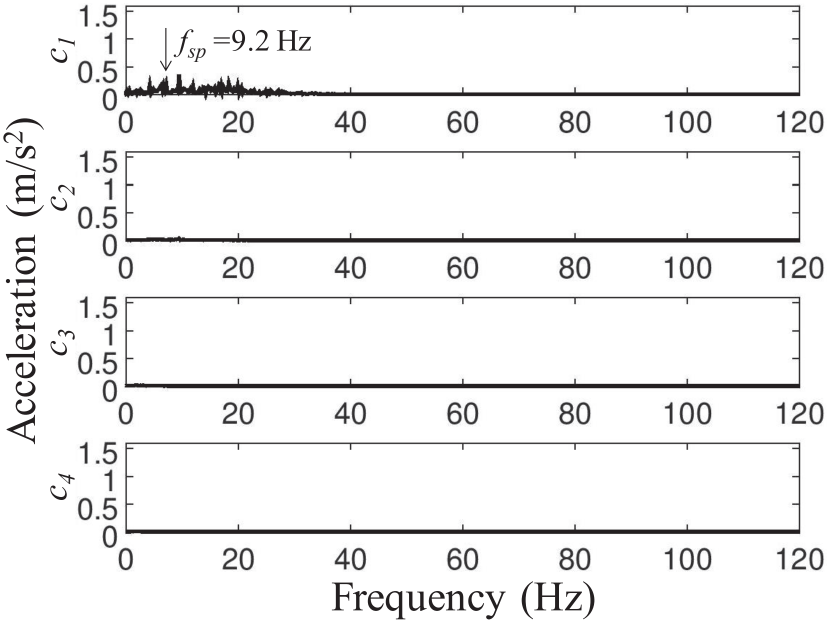

(a) IMFs spectra for stable cutting corresponding to IMFs in **Fig. 6.6(a)**

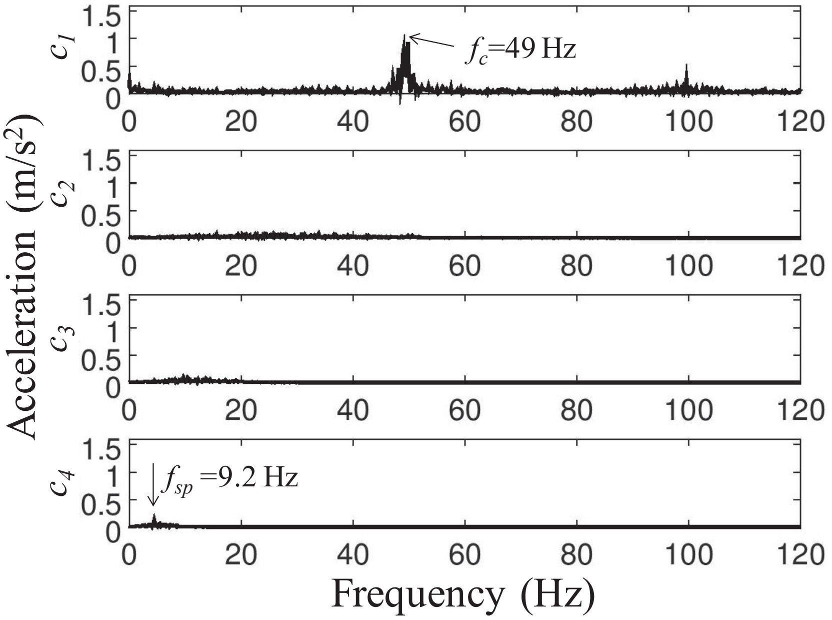

(b) IMFs spectra for severe chatter corresponding to IMFs in **Fig. 6.6(c)**

Fig. 6.1.8. Frequency spectrum for each IMF obtained by FFT.

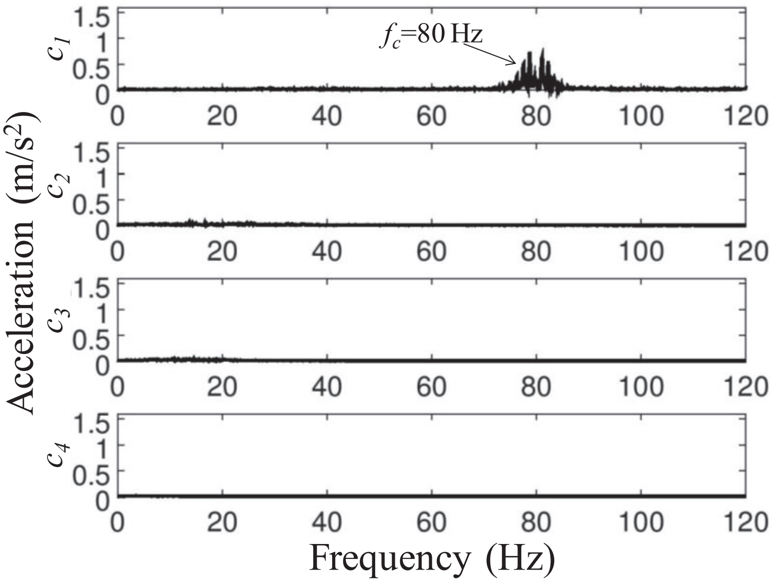

Fig. 6.1.9. IMFs in frequency-domain for transient signal which correspond to IMFs in **Fig. 6.1.7**.

Above results showed that the EMD process separated complex vibrations into simple components, and each one of them contained a unique vibration mode caused in machining. EMD also sifted out the chatter from the others. In our study, the first IMF c_1 in **Fig. 6.1.8(b)** and **Fig. 6.1.9** was IMF containing chatter and other IMFs are signal without chatter. Thus, IMFs obtained by EMD process made it easy for chatter identification when was combined with FFT.

The second step of HHT is applying the Hilbert transform to all IMFs for generating time-frequency distribution which is represented in Hilbert spectrum shown in **Fig. 6.1.10(a)-(c)** and **Fig. 6.1.11(a)**. The resulted Hilbert spectra were compared to other time-frequency (TF) spectrum; namely STFT spectrum obtained by short-time Fourier transform (STFT) shown in **Figs. 6.1.10(d)- 6.1.10(f)** and **Fig. 6.1.11(b)**. According to both Hilbert and STFT spectra, we can monitor turning states both in time and frequency domains for all cases.

Represented in **Figs. 6.1.10(a)-6.1.10(c)** are Hilbert spectra for stable, slight chatter and severe chatter which were associated with the IMFs components given in **Fig. 6.6**. Besides, represented in **Figs. 6.1.10(d)- 6.1.10(f)** are STFT spectra which correspond to the vibrations shown in **Fig. 6.1.1**. Actually, the vibrations obtained in turning of thin-tubular workpieces with wall-thickness $t = 3$ mm.

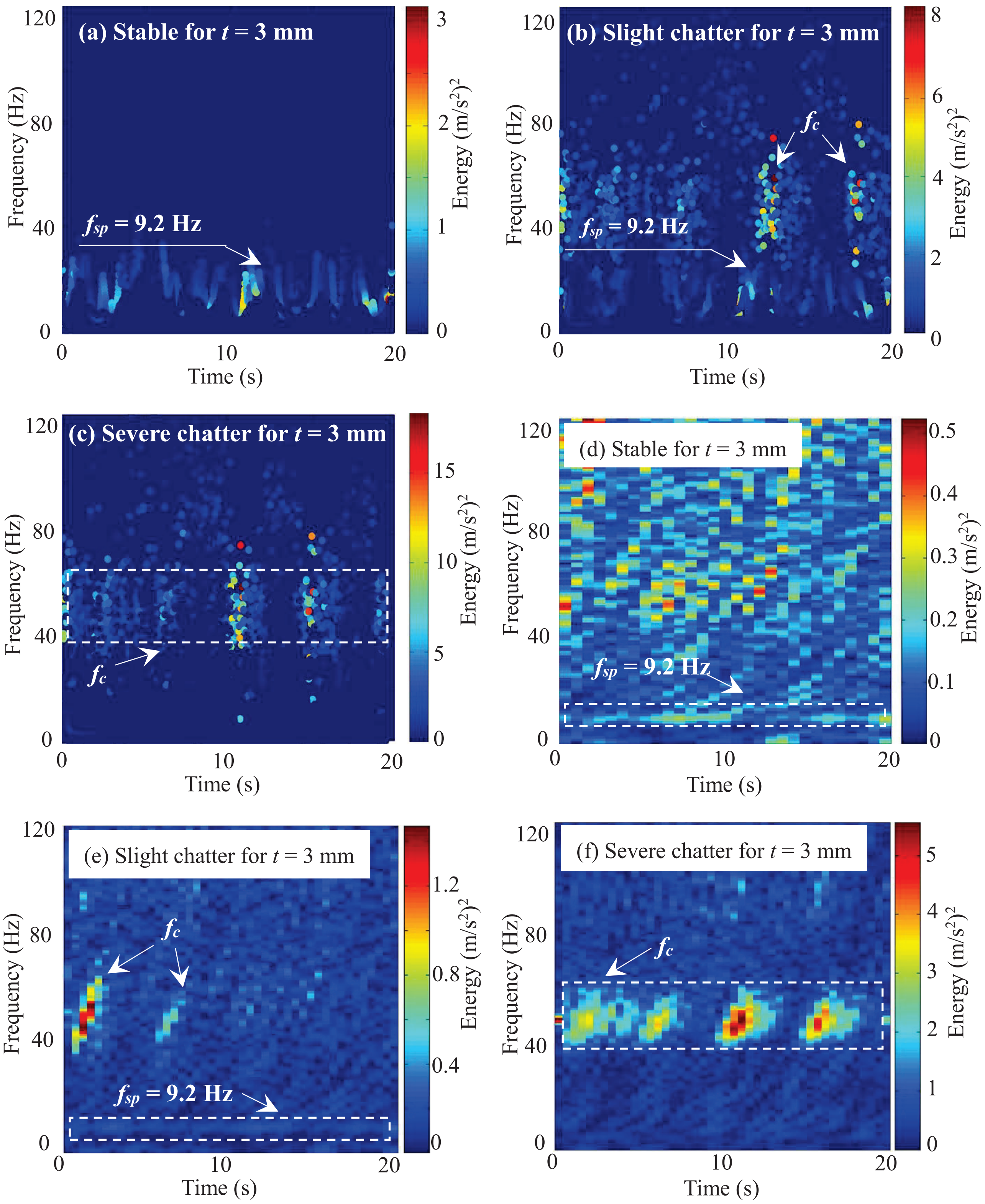

Fig. 6.1.10. Chatter detection in turning using Hilbert spectra and STFT spectra: (a-c) Hilbert spectra, (d-f) STFT spectra.

As shown in the figures, both Hilbert and STFT spectra show good correlation with raw acceleration signals shown in **Fig. 6.1.1**. This leads the conclusion that they have the capability to capture the turning states among stable, slight chatter and severe chatter on acceleration signal obtained with different axial cutting depths. From visual investigation of **Fig. 6.1.10(a)** and **Fig. 6.1.10(d)** which are corresponding to stable cutting, the energy just appears in rotational spindle frequency, at f_{sp} = 9.2 Hz with lowest energy level. And the energy level was increasing when operation is in unstable operation and the chatter frequency f_c is appearing as shown in **Figs. 6.1.10(b), 6.1.10(c), 6.1.10(e)** and **6.1.10(f)**.

Following, we need to compare the Hilbert and STFT spectra by identifying the time-frequency patterns. The comparison was carried out on the resolution of TF spectra and the efficiency of TF spectra to monitor the turning states.

STFT spectra obtained by STFT give blurry time-frequency spectra. Otherwise, Hilbert spectra shows a significant improvement of the frequency resolution making the frequency components easier to be identified. The Hilbert spectra obtained by HHT are clearer than STFT spectra. Unlike STFT method, HHT does not involve the concept of frequency resolution or time resolution but introduces the concept of instantaneous frequency as discussed in Section 2. Consequently, a uniform high resolution is obtained in the full frequency range which makes it suitable to be utilized into a machining process monitoring.

On the other hand, **Fig. 6.1.11(a)** and **Fig. 6.1.11(b)** are Hilbert and STFT spectra for vibration obtained in turning of thin-tubular workpiece t = 5 mm with respect to gradually increasing depth of cut. As previously mentioned, HHT give better frequency resolution and a clearer display of transient acceleration signal. As shown in **Fig. 6.1.11(a)**, the moment when frequency change from rotational spindle frequency f_{sp} to chatter frequency f_c, as any dynamic frequency patterns characteristic to the cutting process, are well captured. However, this moment cannot not be captured in STFT spectrum shown in **Fig. 6.1.11(b)**. Here, STFT has trouble for capturing the moment of frequency change for the unsteady signal.

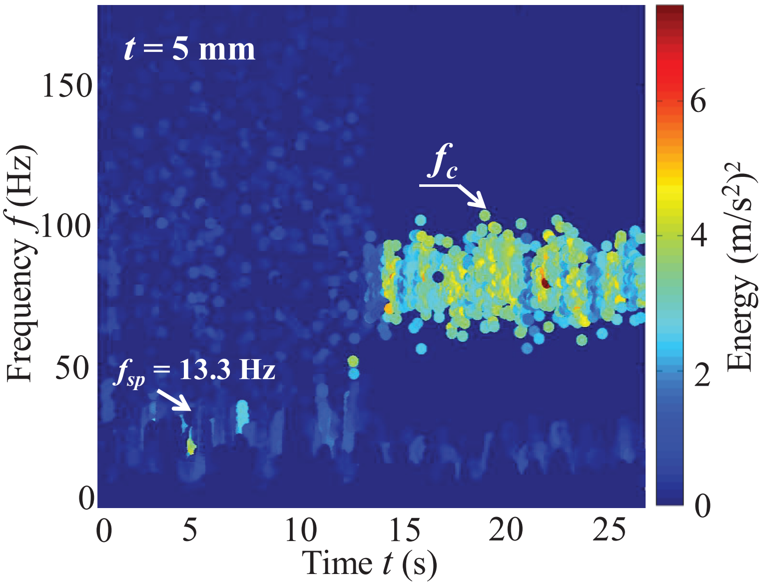

(a) Hilbert spectrum

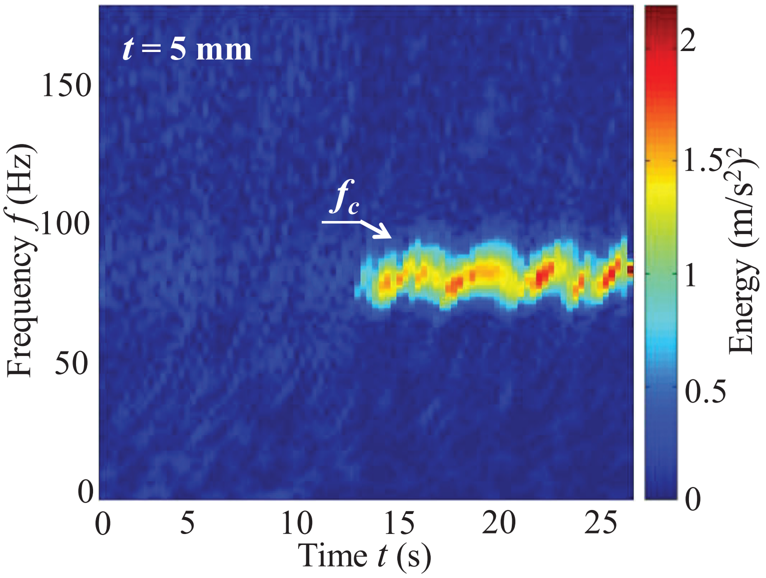

(b) STFT spectrum

Fig. 6.1.11. Chatter detection in turning using Hilbert and STFT spectra for transient acceleration signal.

Therefore, using HHT on the transient signal in turning can improve time-frequency spectrum and helps to correctly identify the characteristics of the cutting process through various frequency components. Any changing frequency events appeared in Hilbert spectrum in the form of changes in patterns of frequency components. From these results, it might be said that HHT clearly shows an advantage over STFT by producing a better time-frequency spectrum resolution for the presented transient signals.

6.1.4. Summary

In this section, the vibrations obtained in turning tests were analyzed in frequency-domain using Fast Fourier transform (FFT) and time-frequency domain using short-time Fourier transform (STFT) and Hilbert-Huang transform (HHT) to reveal chatter in turning. The results are summarized as follows;

1. Vibrations obtained in turning of thin-walled with thickness $t = 3$ mm and $t = 5$ mm and they are analyzed by FFT, STFT, and HHT.
2. The EMD process of HHT decompose complex vibration into simple components and each one of them contains a unique vibration mode caused in machining. EMD also sifted out the chatter from the others and EMD also decomposed signals containing stable, slight chatter and severe chatter obtained in turning with different axial cutting depths.
3. FFT is not suitable for analyzing transient vibration obtained in turning and milling which means its frequency changes over cutting period.
4. STFT spectra provided blurry block spectra and it was trouble for capturing the moment of frequency change for the transient vibration.
5. Besides, Hilbert spectra showed significant improvement of the frequency resolution making the frequency components easier to be identified.

6.2. Chatter Detection in Thin-walled Milling

6.2.1. Time-domain signals obtained in milling test

Figure 6.2.1 shows acceleration signals measured in milling under cutting conditions given in **Table 5.7**. The data length *N* was 5000 points, and the sampling rate was 100 kHz. The data length was twice longer than data length used by Peng [43] and close to the data length used by Zhong et al. [80]. **Figure 6.2.1(a)** is the signal obtained in stable milling, and **Fig. 6.2.1(b)** is one in unstable milling (occurring chatter). As can be seen from the figures, acceleration signals have periodic peaks whose height are fluctuating. Because the peak interval was equal to the tooth passing interval, the fluctuation of signal peak might be caused by change of chip thickness during milling.

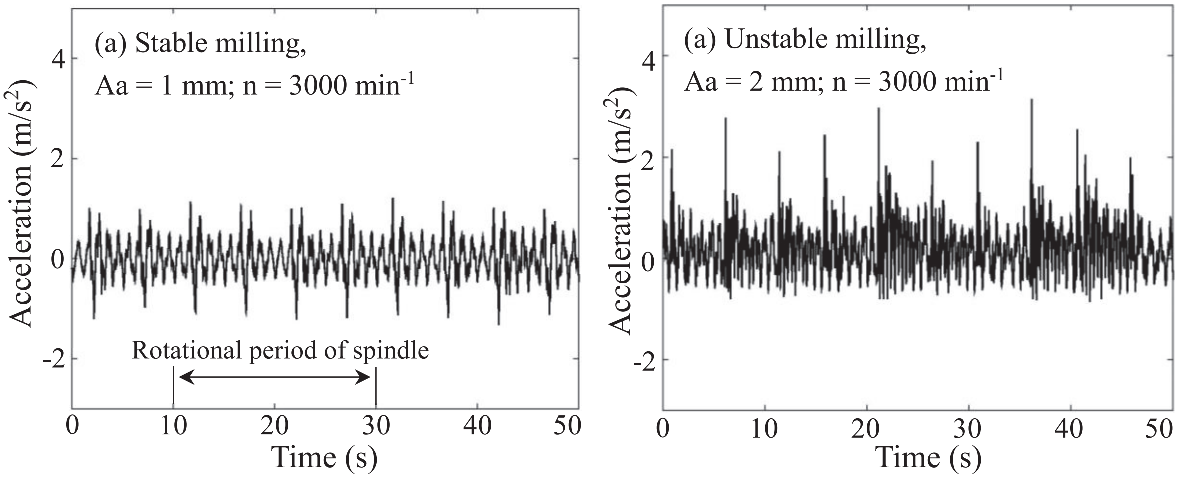

Fig. 6.2.1. Time-domain of acceleration signals obtained in thin-walled milling.

6.2.2. Vibration analysis using FFT for chatter detection

Figure 6.2.2 is the waterfall diagram of frequency spectra obtained by FFT corresponding to signals in **Fig. 6.2.1**. In this figure, symbols of f_n and f_c denote natural and chatter frequencies, respectively. And the arrows denote spindle rotational frequency ($f_s = n/60 = 50$ s^{-1}), tooth passing frequency ($f_p = N_t f_s = 200$ s^{-1}) and the harmonic of frequencies.

As can be seen from **Fig. 6.2.2**, the spectrum of stable milling ($A_a = 1$ mm) shows spindle rotational, natural, tooth passing frequencies and the harmonics with small amplitude. Besides, the spectrum of unstable milling ($A_a = 2$ mm) shows spindle, natural, tooth passing frequencies and the harmonics with amplitude is greater than ones in stable milling. Chatter frequency f_c (940 Hz) also appears with larger amplitude in this frequency spectrum.

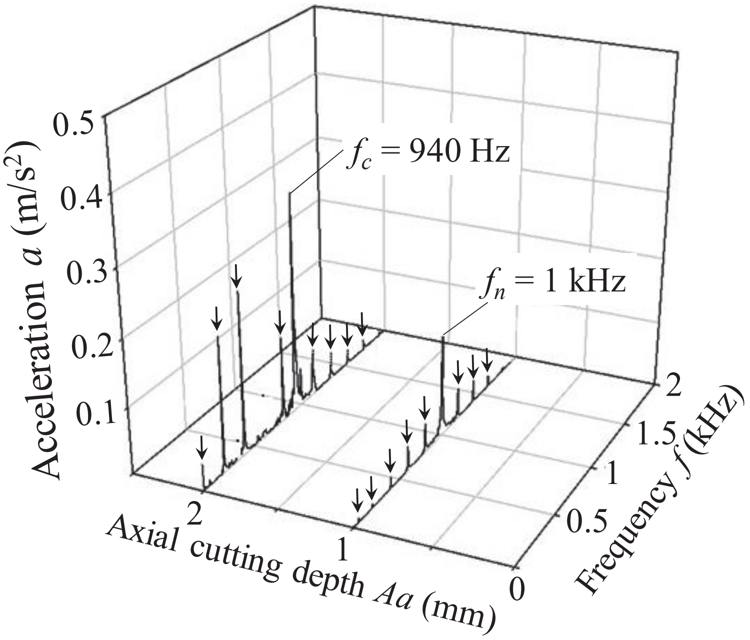

Fig. 6.2.2. Waterfall diagram of frequency spectrum obtained by FFT for stable (A_a = 1 mm), and unstable (A_a = 2 mm) milling.

6.2.3. Vibration analysis using HHT for chatter detection

Figure 6.2.3 shows IMF components c_j resulted by EMD process. Nine components of IMF and a monotonic-residue were obtained for both (a) stable and (b) unstable milling. However, the ninth IMF just showed spindle rotational frequency but did not include significant vibration, and the monotonic-residue was just a residual of the last process in EMD which also did not include significant vibration. Therefore, the first eight IMFs (c_1 to c_8) are shown in these tests for both machining conditions as shown in **Fig. 6.2.3**.

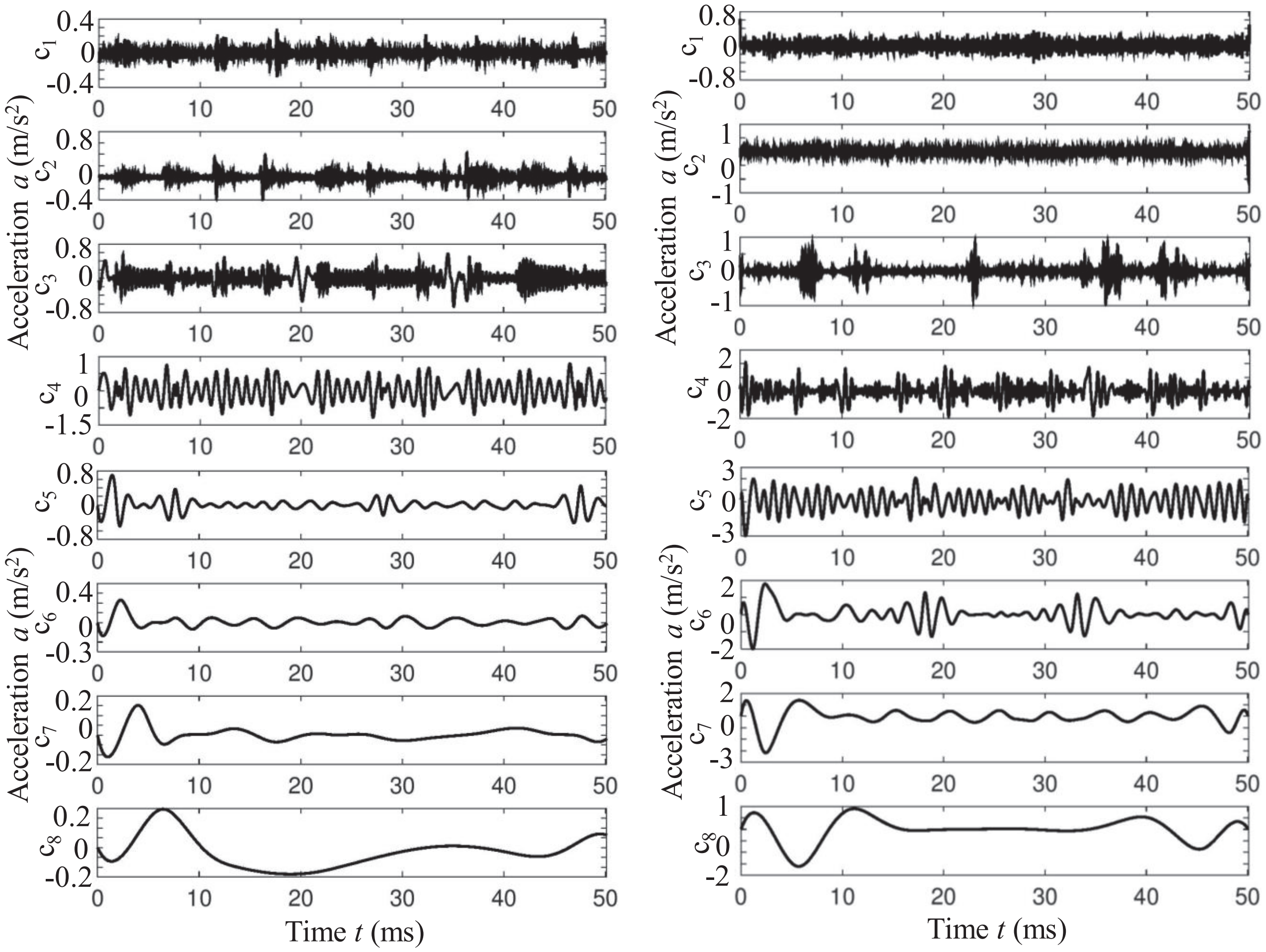

(a) IMFs for stable milling. (b) IMFs for unstable milling.

Fig. 6.2.3. IMF components obtained by EMD process for (a) stable and (b) unstable milling.

As can be seen from **Fig. 6.2.3**, obvious differences of oscillations and amplitudes can be seen among IMFs. For example, the first IMF c_1 contains the most oscillations, otherwise the last IMF c_8 contains the least oscillations among all IMFs. Moreover, c_1 and c_8 contain the highest and the lowest frequency, respectively. Now, let us inspect fourth IMF c_4 of **Fig. 6.2.3(a)** and c_5 in **Fig. 6.2.3(b)**. As can be seen from the figures, they capture the smooth oscillation of signals in these tests. Furthermore, c_4 in **Fig. 6.2.3(a)** contains the highest amplitude among IMF components for stable milling and c_5 in **Fig. 6.2.3(b)** is the highest one for unstable milling. Therefore, each IMF contains a unique information about the vibration mode in the experimental tests.

To confirm above deduction, each IMF in **Fig. 6.2.3** was examined in frequency-domain to observe frequency content of each IMF, and the results are shown in **Fig. 6.2.4**. The cutting period of 50 ms was used to get frequency spectra in **Fig. 6.2.4**. All symbols in these figures denote same as in **Fig. 6.2.2**. As can be seen from **Fig. 6.2.4**, the characteristic frequency with different amplitude appears in each IMF. It also should be noted that each IMF component contains one unique frequency which means that the sifting process by EMD separated the complex vibration into simple components properly. For example, high mode components of IMF (c_1 to c_3) include harmonic of tooth passing frequency with small amplitude for both of stable and unstable milling conditions. In **Fig. 6.2.4(a)**, c_4 includes the natural frequency (1 kHz) of cutting system and lower mode components c_5 and c_6 display tooth passing frequency and the harmonics. In **Fig. 6.2.4(b)**, c_4 and c_6 show the tooth passing frequency and the harmonics, however chatter frequency appears in c_5. Here, chatter frequency (940 Hz) also appears with the larger amplitude.

Above results showed that EMD process decomposed the complex raw signal into simple components, and each one of them contained a unique vibration mode caused in machining. EMD process also sifted out the chatter from other signals. In our study, fifth IMF c_5 shown in **Fig. 6.2.4(b)** is the signal containing chatter and other IMFs in **Fig. 6.2.4(b)** are signal without chatter. Thus, IMFs obtained by EMD process made it easy to recognize the chatter growing as cutting depth was increased.

The next step of HHT is applying the Hilbert transform to all IMFs for generating energy-time-frequency distribution, which are presented in Hilbert spectrum. And **Fig. 6.2.5** shows Hilbert spectra obtained by Hilbert transform. **Fig. 6.2.5(a)** is Hilbert spectrum corresponding to IMFs for stable milling, and **Fig. 6.2.5(b)** is one for unstable milling (occurring chatter). These Hilbert spectra provide energy-time-frequency distribution, which made it easy to detect chatter at any time and frequency. It is different from frequency spectra obtained by FFT as given in **Fig. 6.2.2,** which just provided frequency-domain for chatter detection over sampled cutting period.

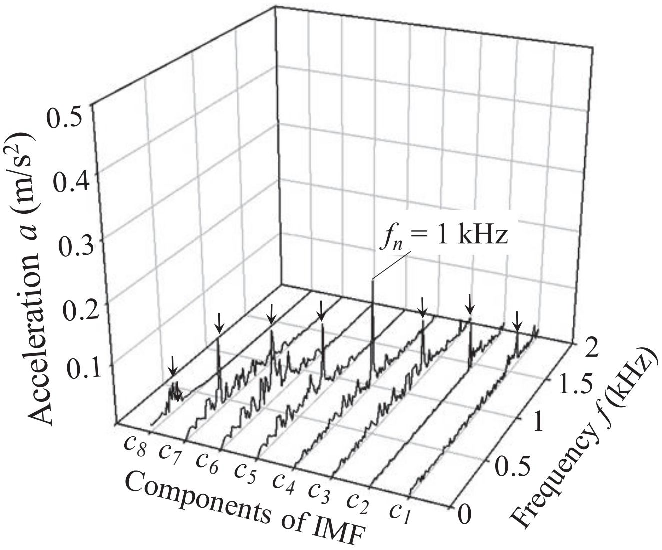

(a) IMFs for stable milling.

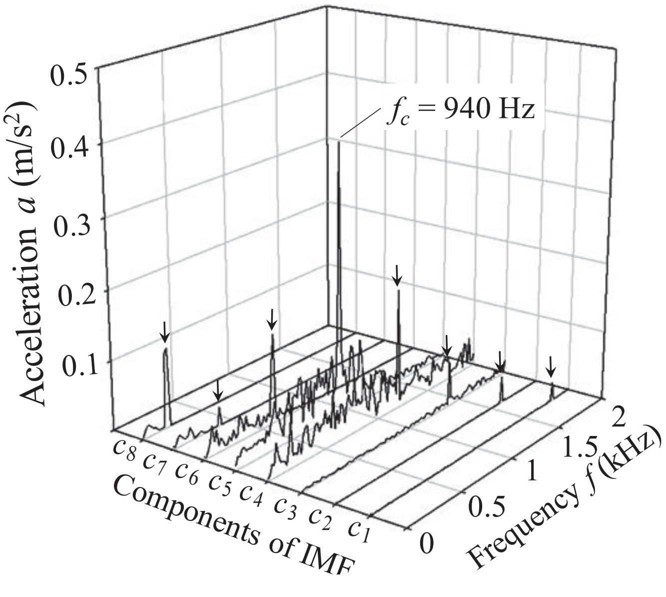

(b) IMFs for unstable milling.

Fig. 6.2.4. FFT spectra of all IMFs to examine frequency content of each IMF.

As can be seen from **Fig. 6.2.5**, the energy level for unstable milling was greater than stable milling. This is because of the occurrence of chatter vibration. In **Fig. 6.2.5(a)**, the energy is concentrated in particular frequency (1 kHz). Besides, the energy in unstable milling is chaotic and the frequency is not constant over sampled cutting period as shown in **Fig. 6.2.5(b)**. According to the color bar of Hilbert spectrum for unstable milling condition, the spectrum contains different magnitude of energy. It was caused by cutting with fluctuating radial cutting depth. And from **Fig. 6.2.5(b)**, the energy level fluctuating during short time range and each cutting edge excited the vibration of the workpiece. In this figure, first cutting edge contains the largest effect on the vibration. And, these results showed that HHT could reveal the difference excitation among cutting edges.

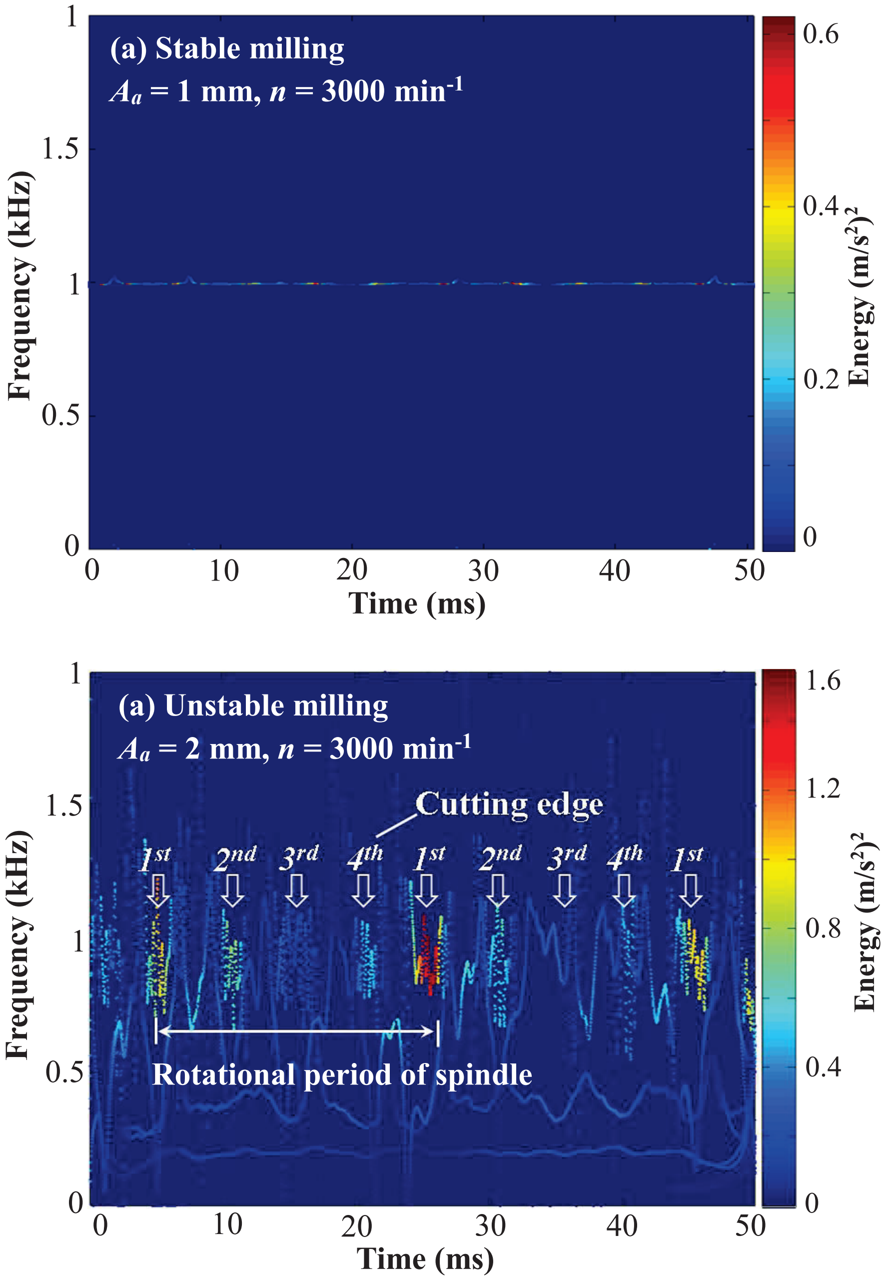

Fig. 6.2.5. Hilbert spectra for (a) stable and (b) unstable milling.

6.2.4. Summary

In this section, the vibrations obtained in milling tests were analyzed in frequency-domain using Fast Fourier transform (FFT) and energy-time-frequency domain using Hilbert-Huang (HHT) transform to reveal chatter in milling. The results are summarized as follows;

1. Each IMF obtained by EMD process contained a unique vibration mode caused in milling process.
2. EMD separated chatter from other signals. Thus, EMD process made it easy to identify chatter growing up as the cutting depth was increased.
3. In Hilbert spectrum of stable milling, the energy of cutting was concentrated in certain frequency. Besides, the energy for unstable milling was chaotic and the frequency was not constant over the time.
4. HHT could reveal the difference excitation among cutting edges during milling process.

6.3. Sudden Change of Machining Stability caused by Lubrication

6.3.1. Time-domain signals obtained in milling

In this section, the effect of cutting fluid on the vibration are discussed. These tests were conducted under unstable conditions of SLD given in **Fig. 5.7** and using cutting parameters shown in **Table 5.8**. In addition, some lubrication was put on the cutting path of workpiece shown in **Fig. 5.11**.

Transition of signals obtained in milling tests are shown in **Fig. 6.3.1**. **Figure 6.3.1(a)** and **Fig. 6.3.1(c)** represent; acceleration and strain signals, which were measured using accelerometer and strain-gauge sensors, respectively. As can be seen from these figures, both acceleration and strain signals have different amplitudes over the cutting period. The amplitudes increase at cutting period 16–35 seconds and 111–114 seconds. The increasing of amplitude occurred in dry cutting and under unstable milling. On the other hand, the amplitudes decrease at cutting period 0–15 seconds and 36–110 seconds. These decreasing of amplitudes are caused by the cutting fluid which was put on the workpiece. In this case, the cutting fluid allowed the reducing of cutting resistance during milling to inhibit chatter, i.e., the effect of the cutting fluid can be attributed to reduction of cutting coefficients in dynamic model of milling. So that, the cutting fluid influenced on the stability in milling of thin-walled workpieces.

To explore other important information about acceleration and strain signals both, the signals in solid boxes of **Fig. 6.3.1(a)** and **Fig. 6.3.1(c)** were sampled, and the magnified ones are displayed in **Fig. 6.3.1(b)** and **Fig. 6.3.1(d)**. As can be seen from these figures, the amplitudes decrease at cutting period 1.7 seconds for all signals, but the amplitude of acceleration signal is greater than strain signal. Further, the signals in **Fig. 6.3.1(b)** and **Fig. 6.3.1(d)** were analyzed in detail in the following section.

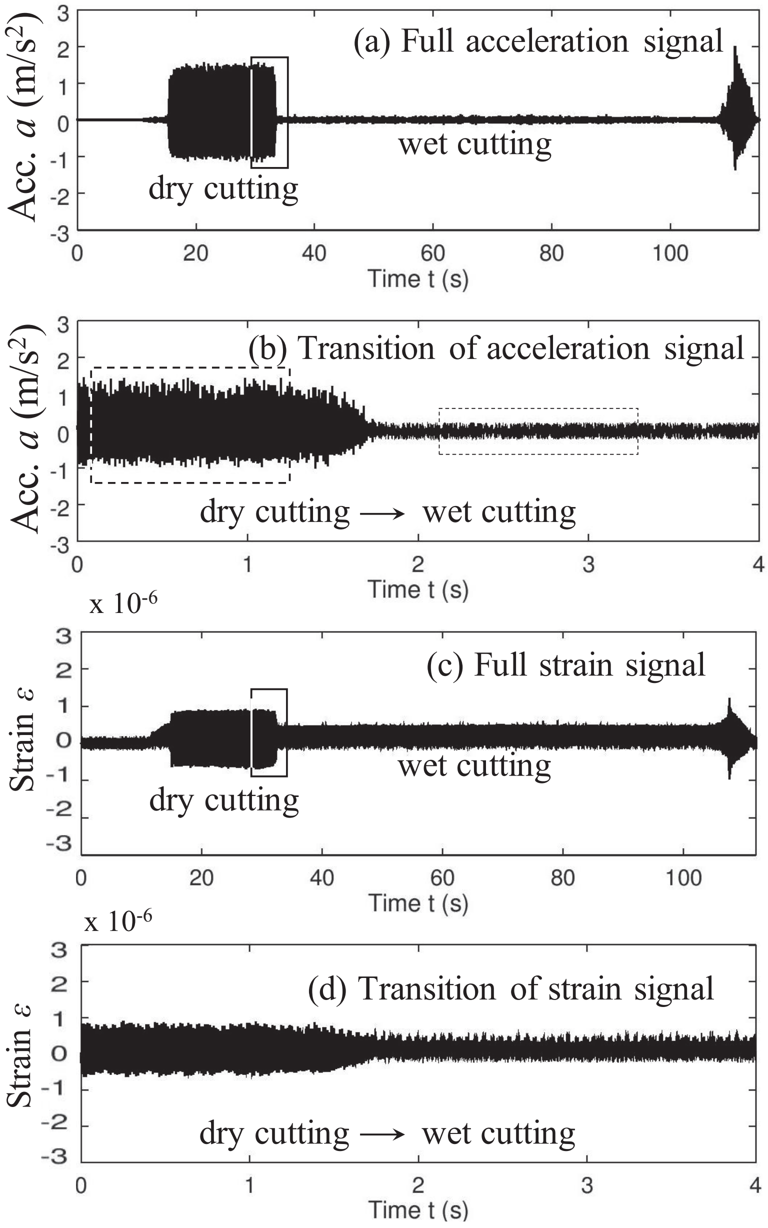

Fig. 6.3.1. Time-domain of acceleration and strain signals obtained in milling Caused by lubrication; (a) and (c) are full signals, (b) and (d) are transition of signals from dry to wet milling.

6.3.2. Vibration analysis for observing sudden change of machining stability using FFT

The frequency contents of both acceleration and strain signals are observed using FFT and the results are shown in **Fig. 6.3.2**. The cutting period of 4 seconds was used to get those frequency spectra. **Fig. 6.3.2(a)** shows frequency spectrum for a transient acceleration signal, which corresponds to signal in **Fig. 6.3.1(b)**. Besides, **Fig. 6.3.2(b)** is ones for transient strain signal, which corresponds to signal in **Fig. 6.3.1(d)**. According to these figures, the frequencies appear in certain frequency range. **Fig. 6.3.2(a)** for instance, the frequency is distributed in 1.2-2 kHz. In this figure, chatter frequency f_c and harmonics of tooth passing frequency (arrows symbol) appear in the high frequency. On the other hand, in **Fig. 6.3.2(b)**, the frequency is distributed in two frequency bands; in 80 Hz and 1.2-2 kHz. In this figure, tooth passing frequency appears in low frequency. Besides, harmonics of tooth passing frequency and chatter frequency f_c appears in the high frequency.

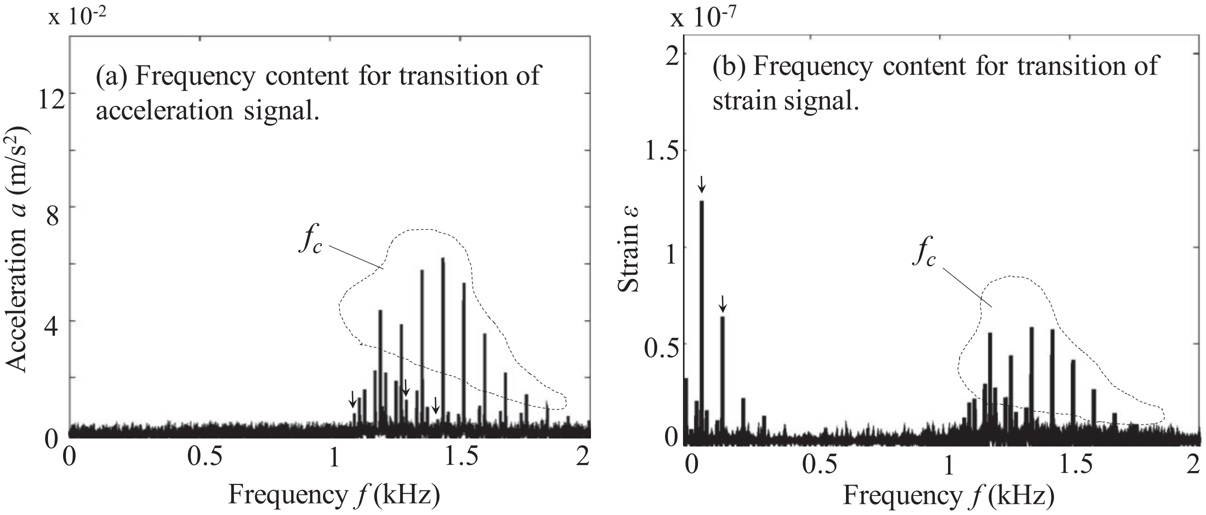

Fig. 6.3.2. Frequency spectra for transition signals from dry to wet cutting; (a) acceleration, and (b) strain signals.

To analyze the effects of cutting fluid to frequency content, the acceleration signal in the **Fig. 6.3.1(b)** was analyzed. First, from **Fig. 6.3.1(b)**, the dry cutting period of 1.6 seconds (dotted box) was chosen for FFT analysis to obtain the spectrum, then the wet cutting period (dotted box) was also chosen to do same procedure. **Fig. 6.3.3** shows the frequency obtained spectra and analyzed acceleration signals are also displayed as the inserted figures.

By comparing **Fig. 6.3.3(a)** with **Fig. 6.3.3(b)**, the amplitude in the frequency range of 1.2–2 kHz decreases and the chatter frequencies are vanished. Thus, the cutting fluid affected on the frequency content in the wide range of frequencies.

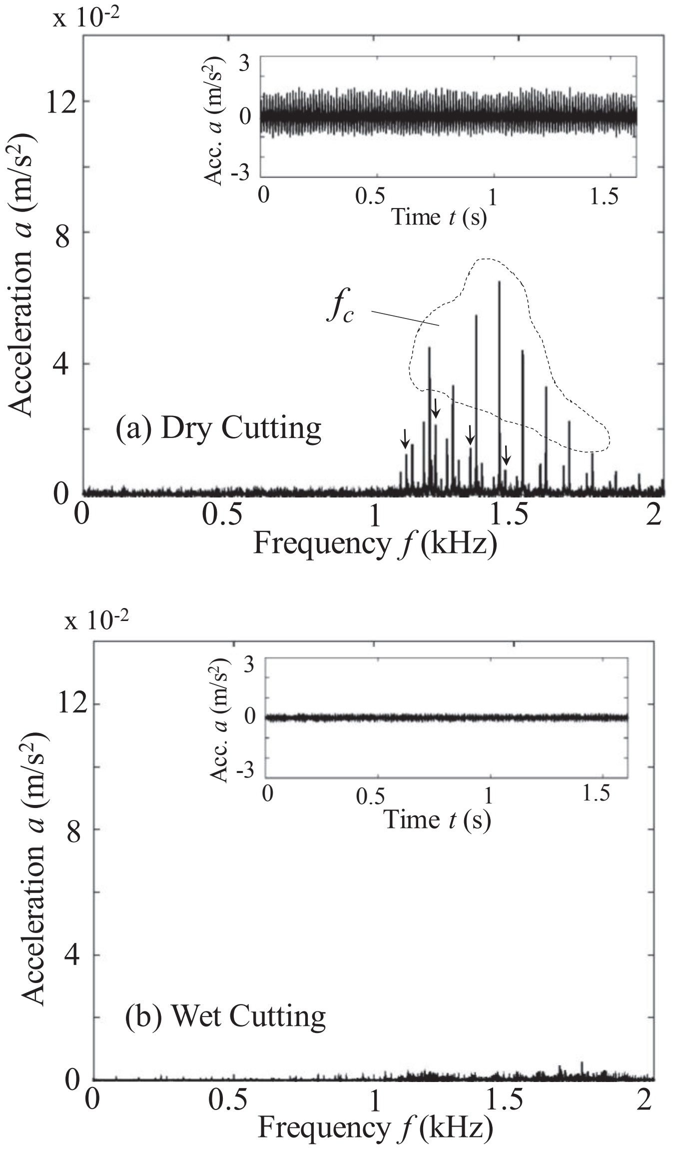

Fig. 6.3.3. Effect of cutting fluid on frequency content of acceleration signals obtained in (a) dry cutting, and (b) wet cutting.

6.3.3. Vibration analysis for observing sudden change of machining stability using HHT

Figure 6.3.4 shows IMF components in time-domain obtained by EMD process for both acceleration and strain signals. **Fig. 6.3.4(a)** is IMFs corresponding to signal in **Fig. 6.3.1(b)**, and **Fig. 6.3.4(b)** is IMFs corresponding to signal **Fig. 6.3.1(d)**. In this process, twelve IMF components and a monotonic-residue were obtained. And the important information of those IMFs were examined using Hilbert transform and the results are shown in **Fig. 6.3.5**. **Figure 6.3.5(a)** is the Hilbert spectrum of acceleration signal corresponding to IMFs in **Fig. 6.3.4(a)**. Besides, **Fig. 6.3.5(b)** is Hilbert spectrum of strain signal corresponding to IMFs in **Fig. 6.3.4(b)**.

According to **Fig. 6.3.5(a)** and **Fig. 6.3.5(b)**, the milling states is unstable at the beginning of process during the 0-1.7 seconds. The machining process in this period was dry milling. As can be seen from the figures, the energy with high magnitude is distributed in the frequency range of 1.2-2 kHz. The energy with high magnitude of these Hilbert spectra indicated that chatter is occurring at that frequency range and time period. However, after the tool enters the wet area; time of 1.8 seconds until finish, the cutting process is stable. The energy decreases quickly by the cutting fluid and chatter frequency is vanished.

Comparing the frequency spectra in **Fig. 6.3.2** with Hilbert spectra in **Fig. 6.3.5**, we can see that both FFT and HHT informed the chatter frequency. Especially, the Hilbert spectra informed all of we need completely; the occurrences of chatter frequency, period, energy and vanished of them.

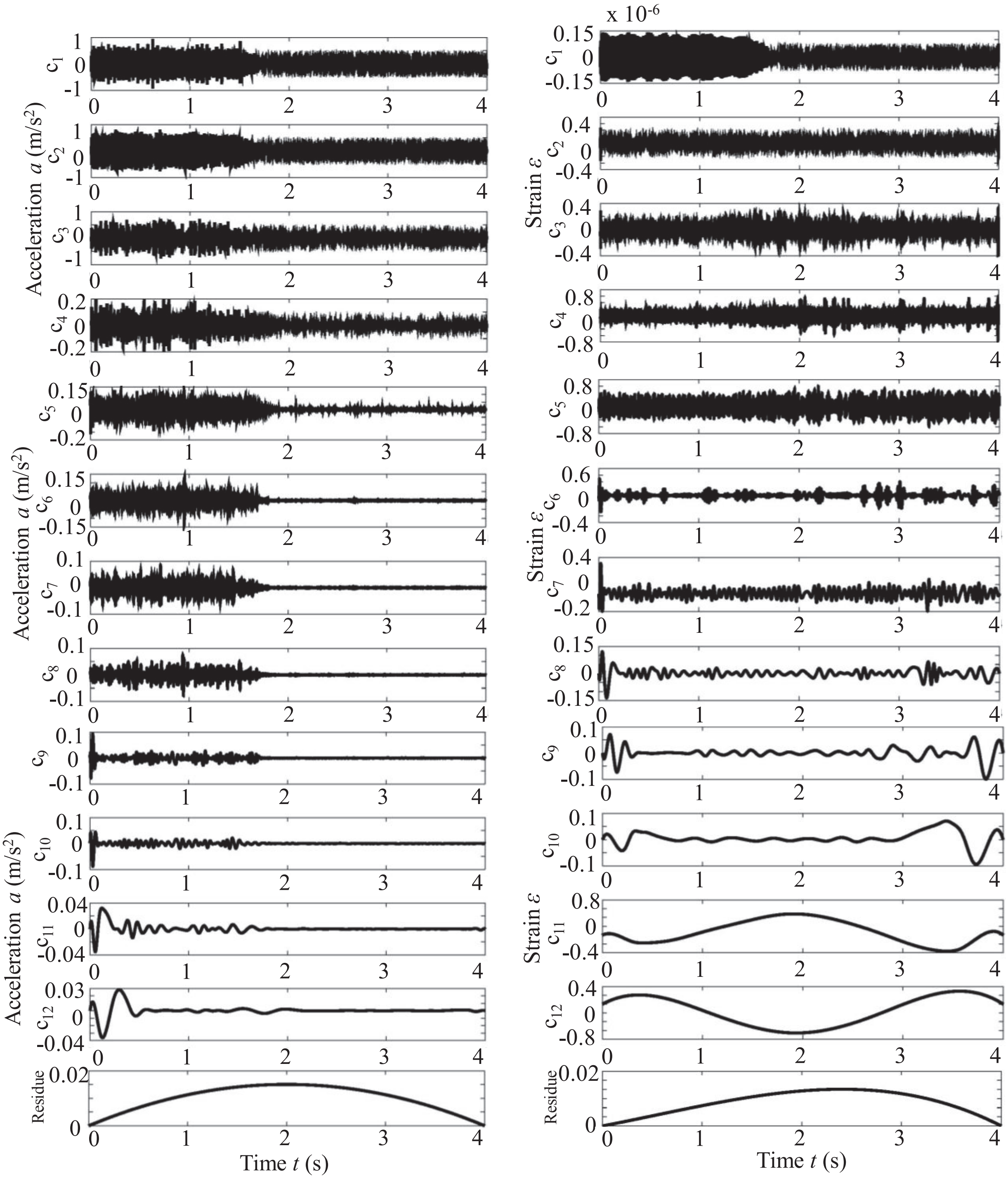

(a) IMFs correspond to acceleration signal.

(b) IMFs correspond to strain signal.

Fig. 6.3.4. A set of IMF components obtained by EMD process.

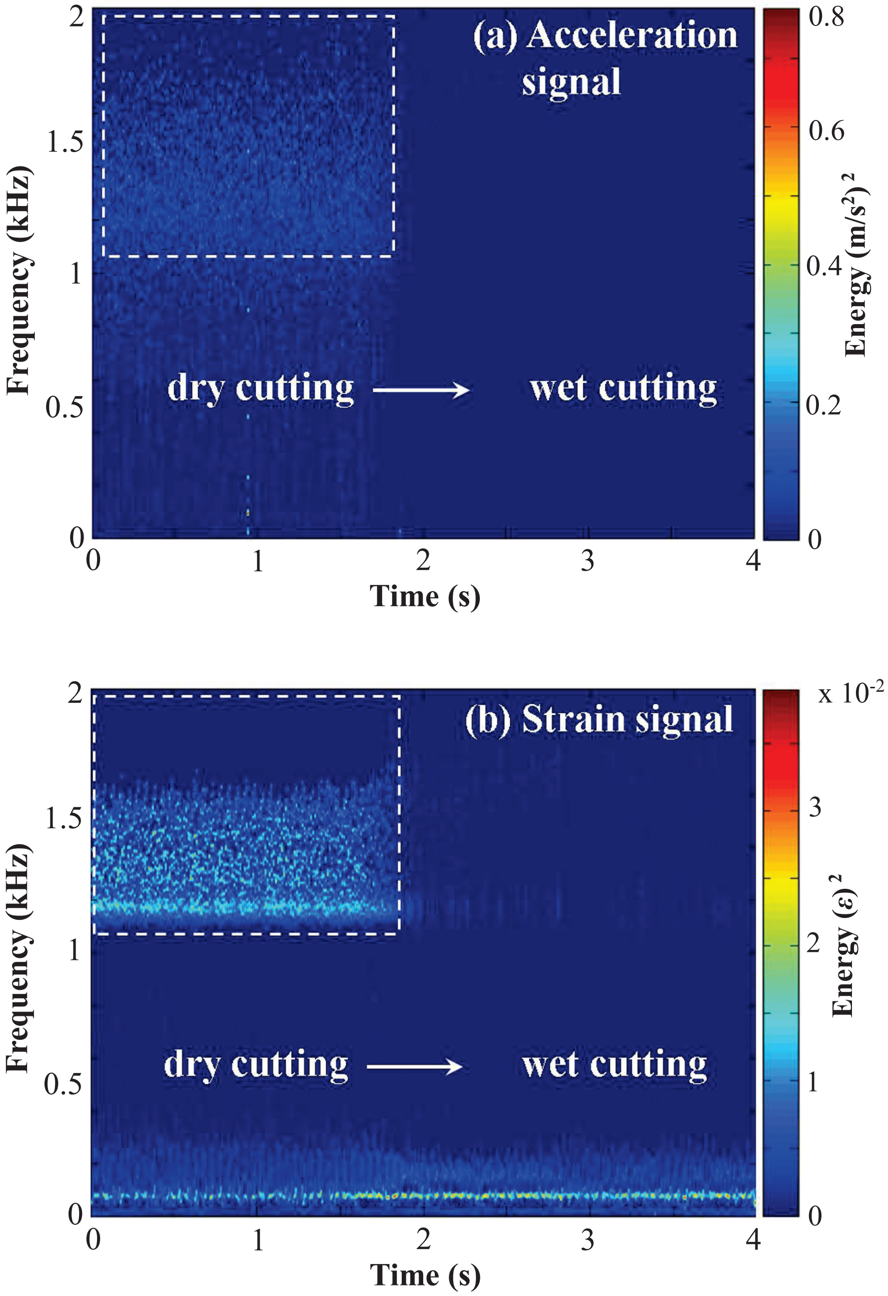

Fig. 6.3.5. Transition energy in Hilbert spectra obtained in dry and wet milling.

In addition, in **Fig. 6.3.5(b)**, there are two main frequencies appear in this Hilbert spectrum, those frequencies are 80 Hz and the frequency of 1.2-2 kHz. The frequency of 80 Hz was tooth passing frequency, which was calculated by $f_p = N_t f_s$, where number of teeth N_t is 4, and spindle rotational frequency f_s is 20 seconds^{-1}). In order to observe clearly about low frequency in **Fig. 6.3.5**, then the frequency in **Fig. 6.3.5(b)** is magnified as shown in **Fig. 6.3.6**.

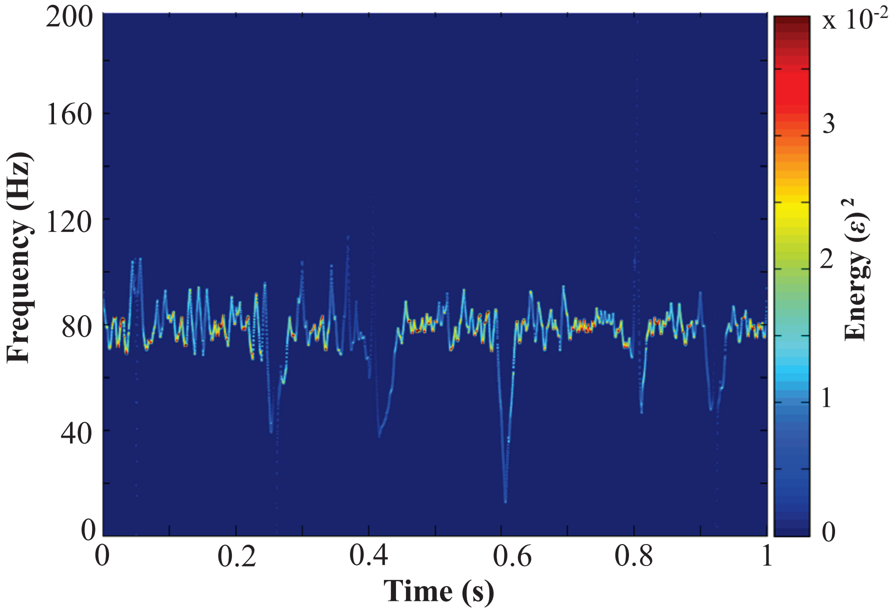

Fig. 6.3.6. Magnified Hilbert spectrum of **Fig. 6.3.5(b)**.

Based on the above results, the strain-gauge sensor worked better than accelerometer sensor in the signal measurement. Because it captured all vibration modes rather than accelerometer sensor. The frequency corresponds to strain signal appeared both low and high frequencies in the frequency spectrum of FFT and Hilbert spectra of HHT and **Fig. 6.3.6**). Otherwise, the signal measured using accelerometer did not capture the low frequency but just captured high frequency as shown in **Fig. 6.3.2(a)** and **Fig. 6.3.5(a)**. Other important information that the cutting fluid enhanced the attenuation of vibration in milling. And the surface topographies for dry and wet milling can be compared as in **Fig. 6.3.7**. As can be seen from those figures, the surface finish in dry cutting is poorer than one in wet cutting. The surface roughness R_a in dry milling was 0.721 µm, and in wet milling one is $R_a = 0.187$ µm.

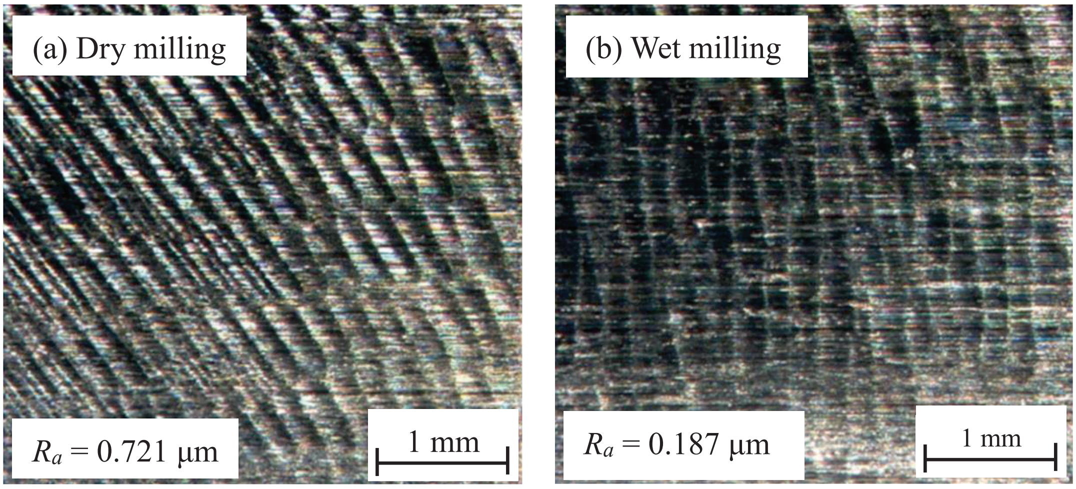

Fig. 6.3.7. Surface topography of machined surface.

6.3.4. Summary

In this section, the vibrations obtained in milling test were analyzed in frequency-domain using Fast Fourier transform (FFT) and energy-time-frequency domain using Hilbert-Huang (HHT) transform to analyze sudden change of machining stability caused by lubrication. The results are summarized bellows;

1. The cutting fluid enhanced the attenuation of vibration in milling which was pointed out in Hilbert spectrum.
2. In Hilbert spectrum, the energy appeared in the certain frequency range for dry cutting, and energy vanished when tool entered in the wet area.
3. Hilbert spectra obtained by HHT provided useful information compared the frequency spectra obtained by FFT for machining process monitoring.
4. The Hilbert spectrum provided complete information about the occurrence of chatter on time-frequency with indicated by the energy and the vanished of chatter caused by a lubricant.

6.4. Sudden Change of Machining Stability Caused by Obstacle in Thin-walled Milling

6.4.1. Time-domain signals obtained in milling test

Figure 6.4.1 is acceleration and strain signals measured in milling under cutting conditions given in **Table 5.9** and milling setup shown in **Fig. 5.13**. **Figs. 6.4.1(a)-(c)** are acceleration signals, and **Figs. 6.4.1(d)-(f)** are strain signals. In detail, **Figures 6.4.1(a)-(d)** show a full time-domain of acceleration and strain signals. From the figures, the cutting tool removes the workpiece in stable milling at the cutting period of 0-12.5 seconds. This cutting process was associated to cut the aluminum material. And then the amplitude of signal grows up suddenly at cutting period of 12.6-14 seconds. This cutting process was associated to cut the aluminum material and crash the steel material. The increasing of amplitude was attributed to the enhancement of cutting coefficients in the dynamic model of milling, which affects on the machining stability. Because the aluminum and steel have different cutting coefficients. According to the amplitude in these figures, it indicates that not all of machining process runs smoothly or always in stable condition during milling process, but sometimes get an obstacle. And in this study, we called it as the bumping milling for the amplitude of signal grows up suddenly. The acceleration signals obtained in bumping and stable milling are shown in the boxes of **Fig. 6.4.1(a)** and the magnified ones are shown in **Fig. 6.4.1(b)** and **Fig. 6.4.1(c)**. Besides, strain signals in **Fig. 6.4.1(d)-(f)** show the magnified ones. To get important information about acceleration and strain signals both, the signals were analyzed in detail in the following section.

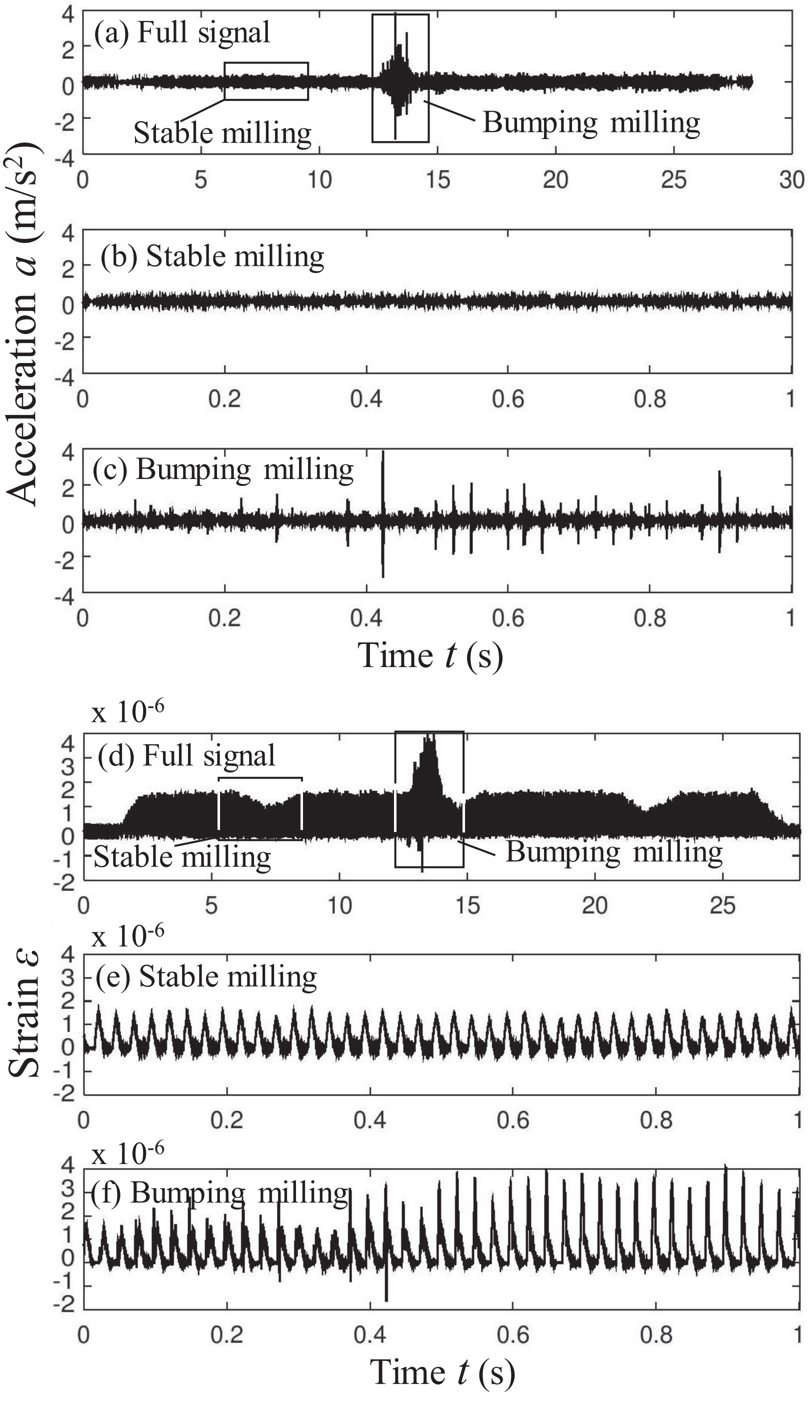

Fig. 6.4.1. Time-domain of acceleration and strain signals. (a) and (d) full signals, (b) and (e) signals obtained in stable milling, and (c) and (f) signals obtained in bumping milling.

6.4.2. Vibration analysis for observing sudden change of machining stability using FFT

Figure 6.4.2 shows frequency spectra obtained by FFT for stable and bumping milling. The cutting period of 1 second was used to get these frequency spectra. These figures were used to describe the effect of stable and bumping milling on the frequency content. **Figure 6.4.2(a)** and **Fig. 6.4.2(c)** are frequency spectra for acceleration and strain signals obtained in stable milling. These frequency spectra are corresponding to time-domain signals shown in **Fig. 6.4.1(b)** and **Fig. 6.4.1(e)**. As can be seen from **Fig. 6.4.2**, frequency of acceleration signal appears in the high frequency (1-1.3 kHz), and frequency of strain signal appears in low frequency (0-40 Hz).

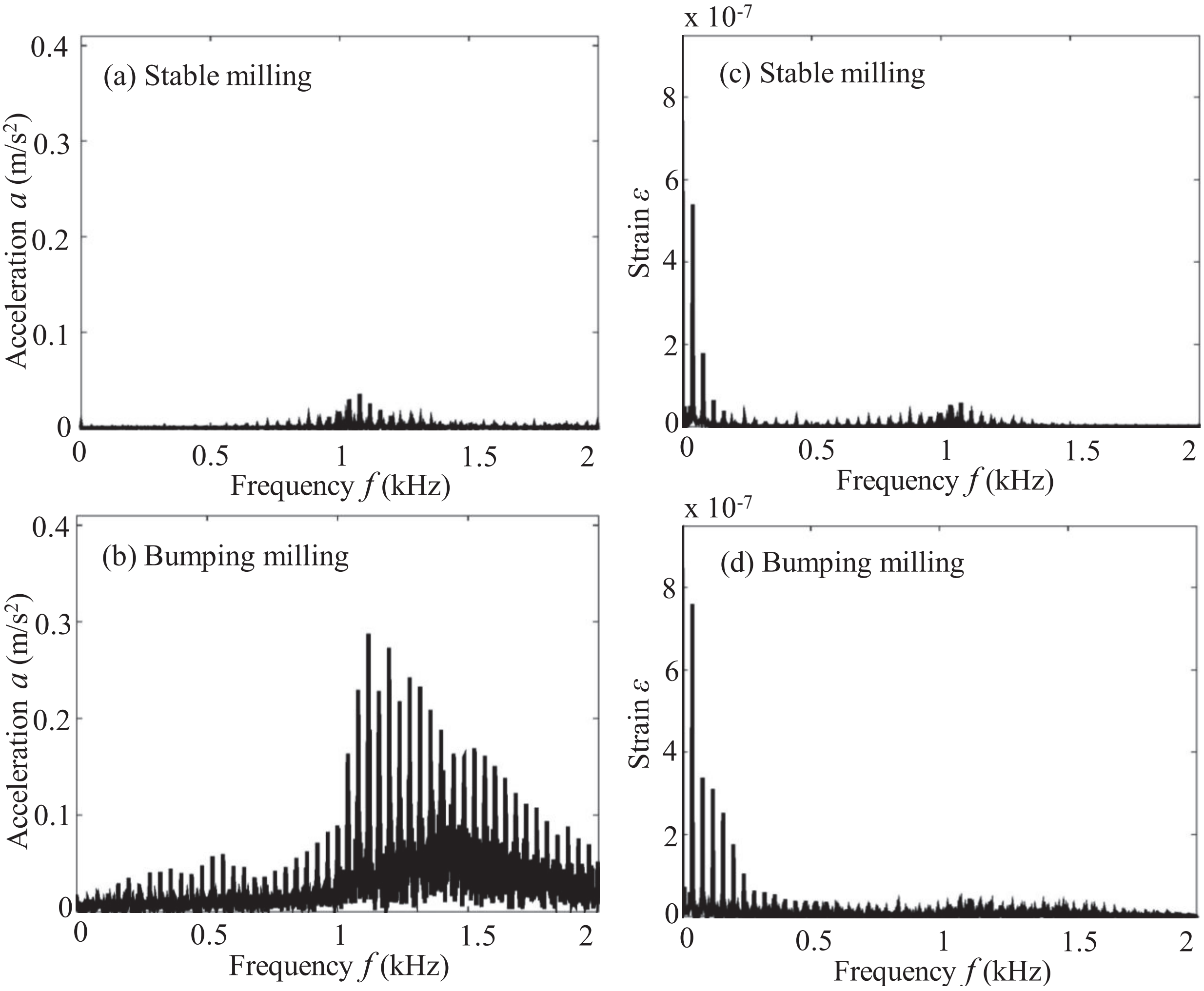

Fig. 6.4.2. Effect of obstacle on frequency content for acceleration, and strain signals. (a) and (b) are acceleration signals, (b) and (d) are strain signals.

On the other hand, **Fig. 6.4.2(b)** and **Fig. 6.4.2(d)** are frequency spectra for acceleration and strain signals obtained in bumping milling. These frequency spectra are corresponding to time-domain signals shown in **Fig. 6.4.1(c)** and **Fig. 6.4.1(f)**. The figures show that frequency of the acceleration signal spreads out over a wider frequency range, namely in 1-2 kHz. Besides, the frequency of the strain signal appears in the low frequency (0-80 Hz).

6.4.3. Stability analysis for observing sudden change of machining stability using HHT

Figure 6.4.3 shows IMF components c_j obtained by EMD process. **Figure 6.4.3(a)** and **Fig. 6.4.3(c)** are IMF components of acceleration and strain signals obtained in stable milling, **Fig. 6.4.3(b)** and **Fig. 6.4.3(d)** are ones obtained in bumping milling. For each milling condition, EMD process resulted nine IMFs and a monotonic-residue. However, these tests showed the first four IMFs (c_1 to c_4) for each milling condition because these IMFs contain vibration modes that we need to be observed in this section. IMF components of acceleration signals is represented in **Fig. 6.4.3(a)** and **Fig. 6.4.3(b)**, and IMF components of strain signals is represented in **Fig. 6.4.3(c)-(d)**.

According to **Fig. 6.4.3**, there is obvious change of the amplitudes in each IMF. The signal obtained in stable milling contain smaller amplitude than the signals obtained in bumping milling. These IMF components were observed in energy-time-frequency domain using Hilbert transform and the results are Hilbert spectra shown in **Fig. 6.4.4**. The Hilbert spectra corresponding to stable milling are shown in **Fig. 6.4.4(a)** and **Fig. 6.4.4(d)**. As can be seen from these figures, the energy was distributed in particular frequency (1 kHz). Besides, the Hilbert spectra correspond to bumping milling shown in **Fig. 6.4.4(b)** and **Fig. 6.4.4(d)**. In these spectra, the energy is messy and there is no frequency characteristic belongs to the energy distribution or the Hilbert spectrum displayed a chaotic spectrum of energy.

Let us examine Hilbert spectra corresponding to strain signal shown in **Fig. 6.4.4(c)** and **Fig. 6.4.4(d)**. As can be seen from these spectra, there are two main frequencies for stable milling, at the low and high frequencies. And, during machining with obstacle, the energy is distributed only at low frequency. Besides, the change of energy was clearly shown in Hilbert spectrum which was generated using strain signal than acceleration signal. It can be seen in **Fig. 6.4.5**. In this figure, the cutting process is analyzed with a longer time to obtain full machining process, from stable to bumping milling. From this figure, we find clear information that milling with obstacle occurs at 2–2.5 seconds.

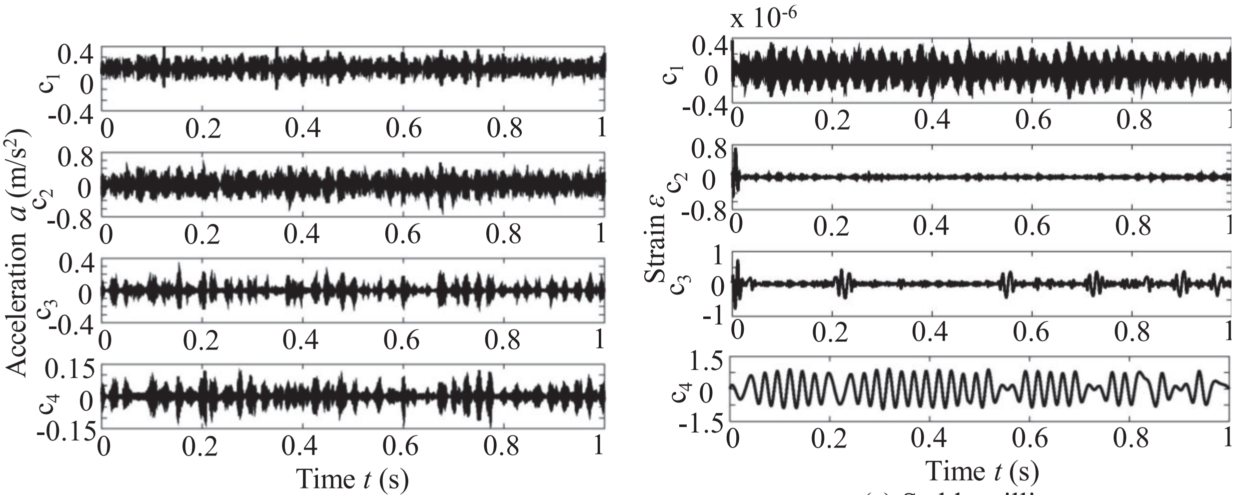

(a) Stable milling

(c) Stable milling

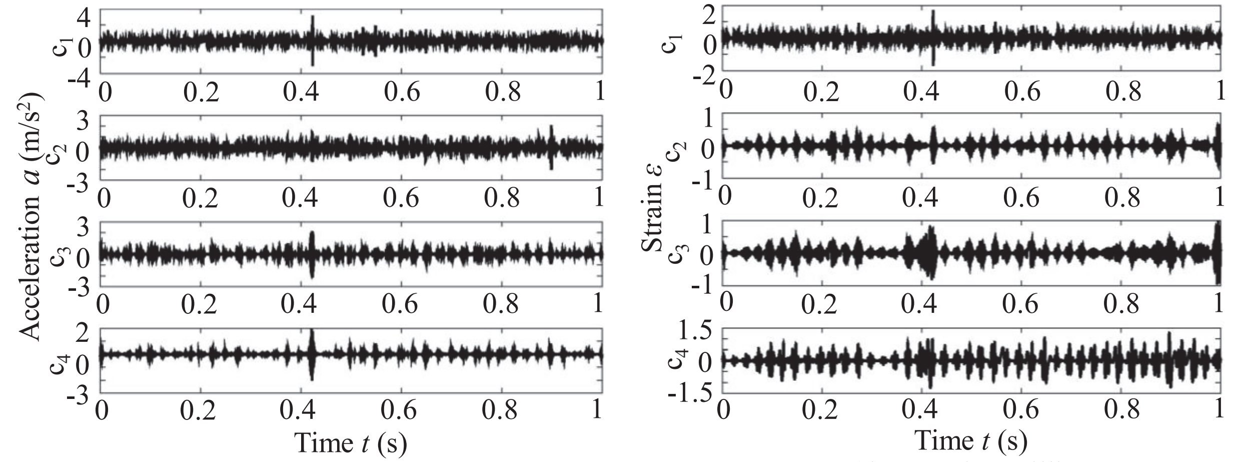

(b) Bumping milling

(d) Bumping milling

Fig. 6.4.3. A set of IMF components for acceleration and strain signals corresponding to obtained in stable and bumping milling.

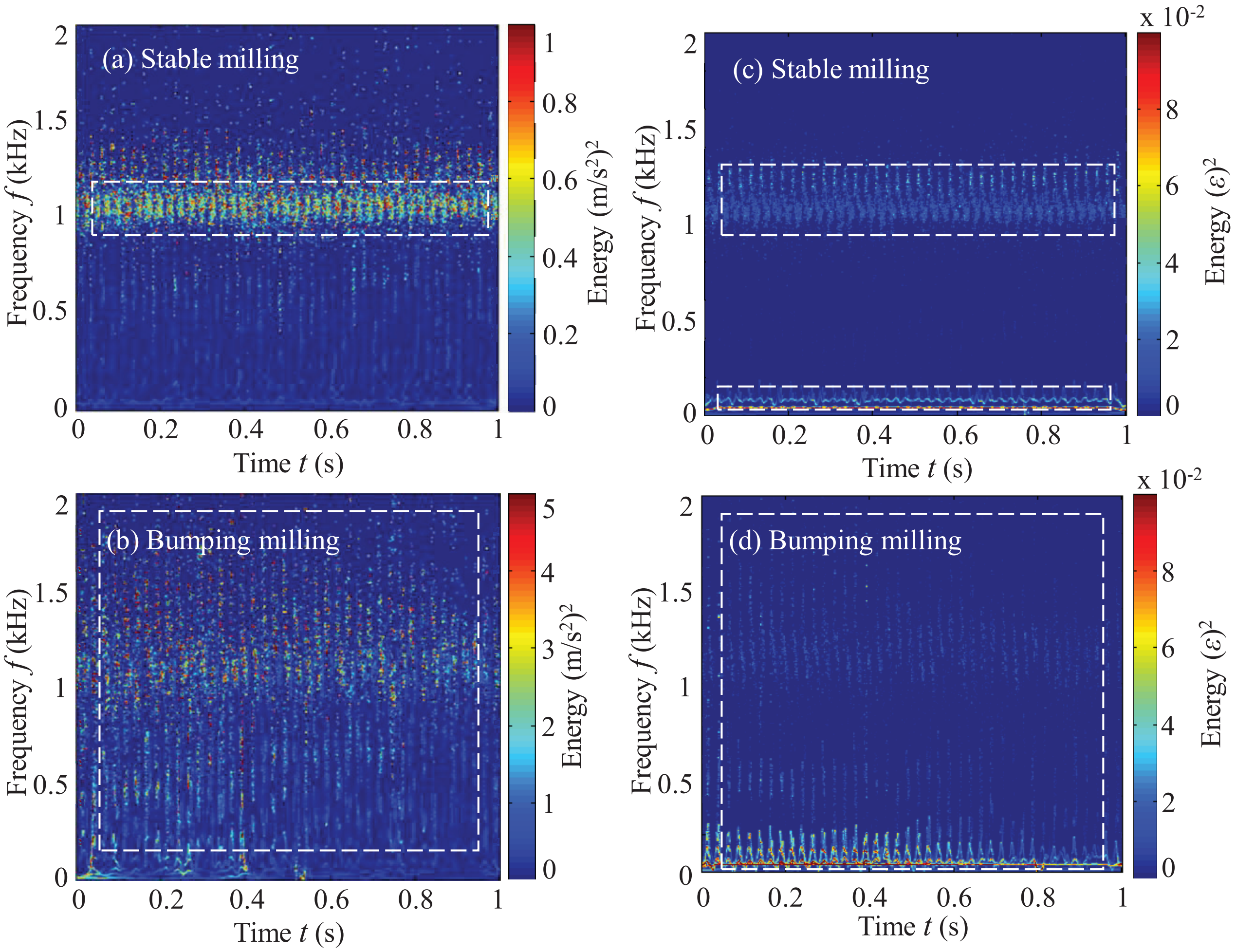

Fig. 6.4.4. Hilbert spectrum for acceleration (left column) and strain (right column) signals corresponding to stable and bumping milling.

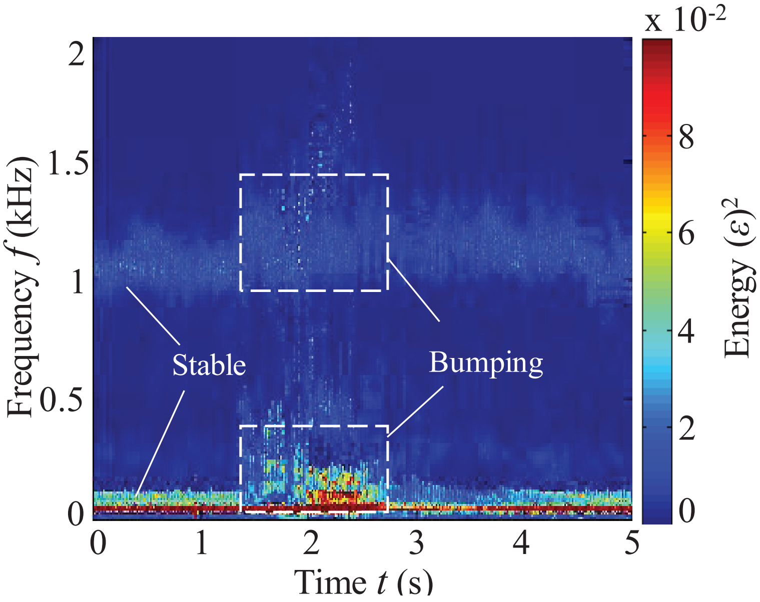

Fig. 6.4.5. Hilbert spectrum from stable to bumping milling.

6.4.4. Summary

In this section, the vibrations obtained in milling test were analyzed in frequency-domain using Fast Fourier transform (FFT) and energy-time-frequency domain using Hilbert-Huang (HHT) transform to analyze sudden change of machining stability caused by obstacle in thin-walled milling. The results are summarized as follows;

1. Hilbert spectra in stable milling showed that the energy was distributed in particular frequency.
2. Hilbert spectra in bumping milling showed that the energy was chaotic and spread out over the spectrum. And there is no frequency characteristic in bumping milling.
3. Hilbert spectra which correspond to strain signal provided the change of energy clearly, therefore the strain signal measured using strain gauge sensor worked well with HHT.

6.5. Tool Condition Monitoring Using HHT

6.5.1. Time-domain signals obtained in milling tests

Figure 6.5.1 shows strain signals obtained in milling under cutting conditions given in **Table 5.10** and using different tool conditions shown in **Fig. 5.14**. **Figure 6.5.1(a)** is strain signal obtained in milling using normal tool. As can be seen from the figure, shapes of the peak are mostly uniform, and the amplitude is smaller than others. Based on the figure, the period of one spindle rotation is approximately 0.1 seconds. It is associated to spindle rotation n = 600 min^{-1} and there are four peaks within one spindle rotation, and one peak of signal was performed by one individual cutting edge of tool.

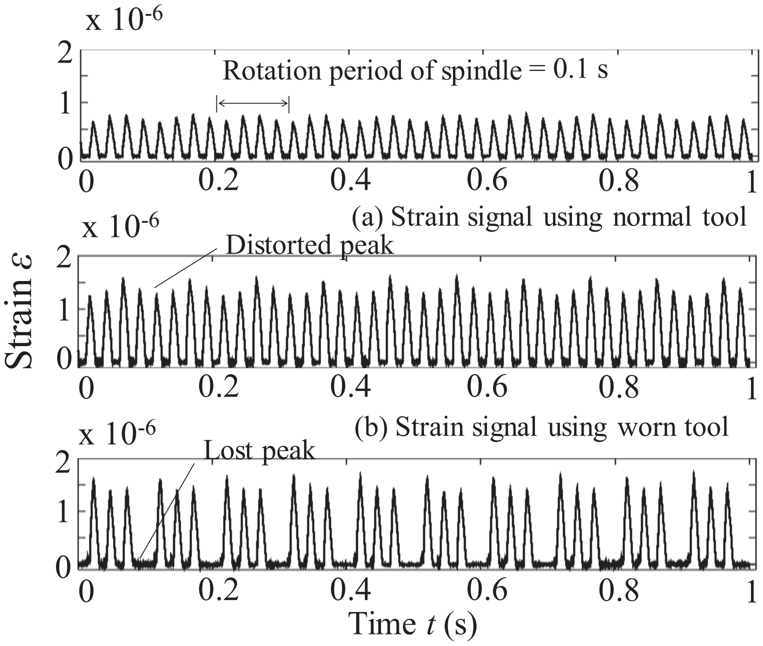

Fig. 6.5.1. Strain signals measured in milling using different tool conditions; (a) normal, (b) wear, (c) chipping tool.

Figure 6.5.1(b) shows strain signal measured in milling using worn tool. As can be seen from the figure, one of signal peaks is distorted within one spindle rotation. The distorted signal was caused by milling using worn tool. **Figure 6.5.1(c)** is strain signal measured in milling using chipped tool. As can be seen from this figure, one of signal peaks is lost within one spindle rotation. The loss of the signal peak was due to the end-mill tool lost one of the cutting edges. As the result, within one spindle rotation is found three peaks of signals.

6.5.2. Vibration analysis for tool condition monitoring using HHT

Figure 6.5.2 shows IMF components obtained by EMD process. Using EMD process twelve IMFs and a monotonic-residue were resulted. However, four IMF components c_5 to c_8 are shown for each milling condition because these IMFs include mode vibration that we need to be observed in this discussion. **Figs. 6.5.2(a)-(c)** are IMF components corresponding to milling using normal, worn and chipped tool, respectively. As can be seen from **Fig. 6.5.2**, there are obvious change of the amplitudes among of IMFs. The IMFs signals obtained in milling using normal tool contain smaller amplitude than milling using worn and chipped tool.

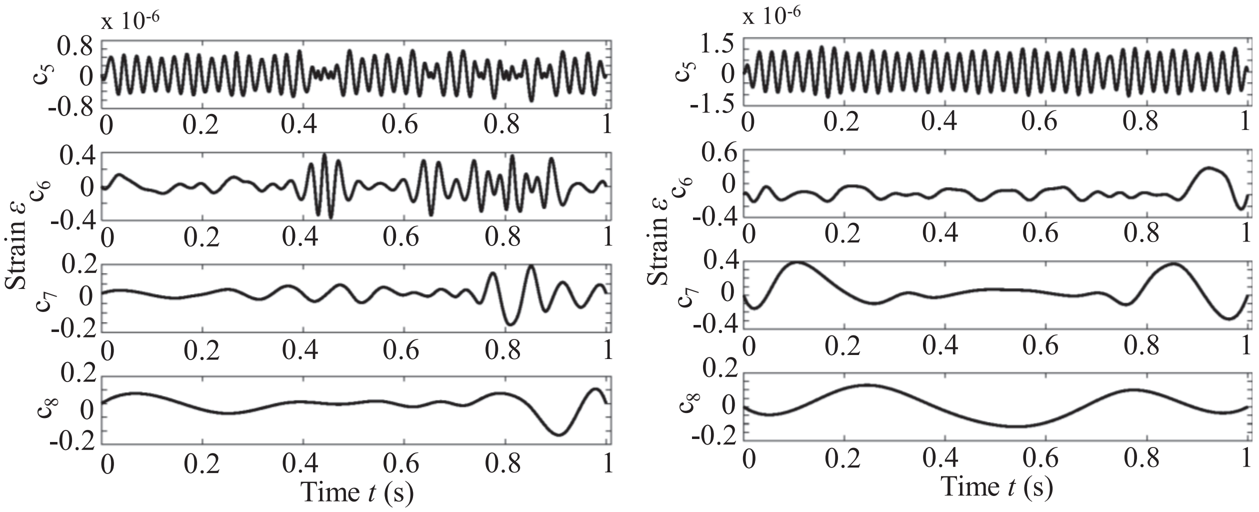

(a) IMFs corresponding to milling using normal tool.

(b) IMFs corresponding to milling using worn tool.

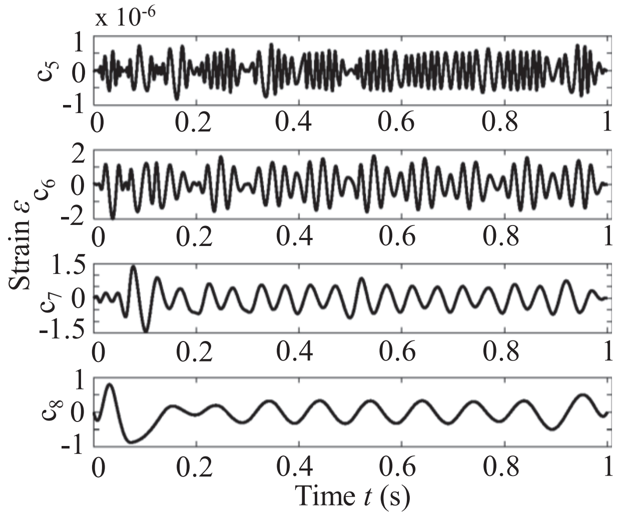

(c) IMFs corresponding to milling using chipped tool.

Fig. 6.5.2. IMF components obtained by EMD process corresponding to milling using different tool conditions.

The intrinsic meaning of each IMF was explored in energy-time-frequency domain using Hilbert transform for tool condition monitor. The result is represented in Hilbert spectrum. As can be seen from **Fig. 6.3.5**, the energy just appears at low frequency, the frequency band, therefore, was narrowed to be 0-80 Hz for each figure to analyze the vibrations more detail.

Figure 6.5.3(a) shows Hilbert spectrum corresponding to strain signal measured in milling using normal tool. As can be seen from this figure, the energy is consentrated at the frequency of 40 Hz over the cutting period. This frequency was tooth passing frequency ($f_p = N_t f_s = 40$ Hz). Besides, **Fig. 6.5.3(b)** shows Hilbert spectrum corresponding to milling using worn tool. In this figure, the energy appears both in the tooth passing frequency of 40 Hz and at new frequency of 10 Hz. The new frequency was spindle rotational frequency ($f_s = n/60 = 10$ Hz). On the other hand, **Fig. 6.5.3(c)** shows Hilbert spectrum corresponding to milling using chipped tool. According to this figure, the energy appears in three frequency components, i.e.; 10, 20, and 40 Hz.

Based on the above results, HHT can be used to monitor tool condition because milling using normal tool can be distinguished from milling using worn tool or chipped tool based on the Hilbert spectrum of HHT. Therefore, we can identify that when the tool was getting wear, the energy in Hilbert spectrum appears at spindle rotation frequency. When end-mill was getting chipping, the energy appears in spindle rotation, tooth passing, and new frequencies. Besides, other important note that strain signal provided a useful signal for tool contition monitoring with HHT.

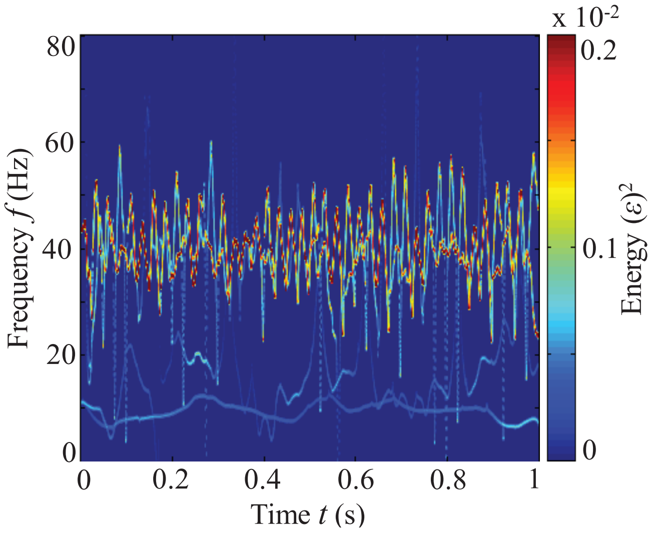

(a) Hilbert spectra corresponding to milling using normal tool.

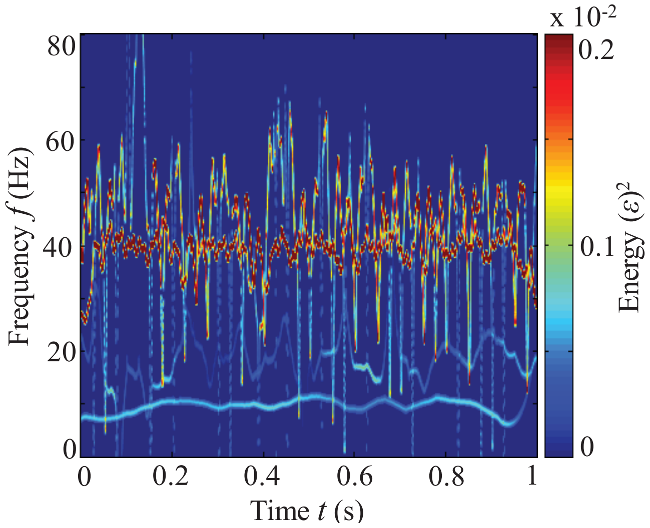

(b) Hilbert spectra corresponding to milling using worn tool.

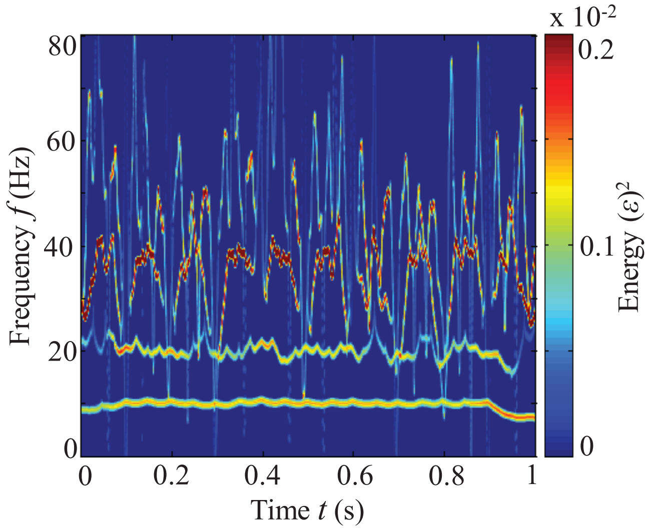

(c) Hilbert spectra corresponding to milling using chipped tool.

Fig. 6.5.3. Hilbert spectra for tool condition monitoring in milling.

6.5.3. Summary

In this section, the vibrations obtained in milling test were analyzed in energy-time-frequency domain using Hilbert-Huang transform (HHT) for tool condition monitoring. The results are summarized as follows;

1. Based on Hilbert spectrum, milling using normal tool can be distinguished from milling using worn tool and milling using chipped tool.
2. From Hilbert spectrum, when end-mill is getting wear, the energy in Hilbert spectrum appears at spindle rotation frequency. When end-mill is getting chipping, the energy appears in spindle rotation, tooth passing, and new frequencies.
3. In this study, strain signal measured using strain gauge sensor can work well with HHT for tool condition monitoring.

Chapter 7
Conclusions

This research presented here focused on machining process monitoring by vibration analysis. Machining process monitoring was to detect; chatter vibration, sudden change of machining stability caused by lubrication, sudden change of machining stability caused by obstacle in thin-walled milling, and to monitor tool condition. Hilbert-Huang transform (HHT) was employed for analyzing signals and the results of HHT analysis were compared with fast Fourier transform (FFT) and short-time Fourier (STFT) transform results. For each signal obtained in turning and milling tests, HHT decomposed the signals to be intrinsic mode function (IMF) components by Empirical Mode Decomposition (EMD) process, and each one of them contains a unique vibration mode caused in machining. Hilbert transform is then applied for all IMFs to generate Hilbert spectrum which represent energy-time-frequency distribution of signals. Following is some important conclusions:

1. The EMD process decomposed complex vibration into simple components, and each one of them contained a unique vibration mode caused in machining. EMD also sifted out the chatter from the others.
2. In turning process, Hilbert and STFT spectra were capable to capture turning states among stable, slight, and severe chatter. However, STFT spectra provided blurry and blocked spectra and STFT spectrum was trouble to capture the moment of frequency change for the transient vibration. Besides, Hilbert spectra showed a significant improvement of time-frequency resolution making the turning states was easier to be identified.
3. For chatter detection in milling process using HHT, the energy of stable milling was concentrated in particular frequency. Besides, the energy of unstable milling was chaotic, and the frequency was not constant. And, HHT have revealed the difference excitation among cutting edges.
4. HHT can reveal the effect of cutting fluid on the stability of milling which was pointed out in Hilbert spectrum. In Hilbert spectrum, the energy appeared in the certain

frequency range for dry cutting, and energy vanished when tool entered in the wet area.

5. Besides, the energy in Hilbert spectrum displayed a chaotic spectrum when milling was unstable caused by machining with obstacle. And, Hilbert spectrum of the stable milling showed that the energy was distributed in particular frequency.
6. HHT can be used for tool condition monitoring. Based on the Hilbert spectrum, milling using worn and chipped tools can be distinguished from milling using normal tool.

REFERENCES

[1]. O. B. Adetoro, W. M. Sim, and P. H. Wen, An improved prediction of stability lobes using nonlinear thin wall dynamics, J. of Materials Processing Technology, Vol. 210, 2010, Pages 969-979.

[2]. M. A. Butt, Y. Yang, X. Pei, and Q. Liu. Five-axis milling vibration attenuation of freeform thin-walled part by eddy current damping, Precision Engineering, Vol. 51, 2018, Pages 682–690.

[3]. K. Kolluru, and D. Axinte, Coupled interaction of dynamic responses of tool and workpiece in thin wall milling, J. of Materials Processing Technology, Vol. 213, 2013, Pages 1565-1574.

[4]. A. Gerasimenkoa, M. Guskova, J. Duchemina, P. Loronga, and A. Gouskov. Variable compliance-related aspects of chatter in turning thin-walled tubular Parts. Proceeding of 15th CIRP Conference on Modelling of Machining Operations, 2015, Pages 58 – 63.

[5]. A. Chanda, and S. K. Dwivedy. Nonlinear dynamic analysis of flexible workpiece and tool in turning operation with delay and internal resonance. Journal of Sound and Vibration, Vol. 434, 2018, Pages 358–378.

[6]. M. R.Khoshdarregi & Y. Altintas. Dynamics of multipoint thread. Turning-Part II: Application to thin-walled oil pipes. Journal of Manufacturing Science and Engineering, Vol. 14, 2018, Pages 1-11.

[7]. P. L. Huang, J. F. Li, J. Sun, and X. M. Jia. Cutting signals analysis in milling titanium alloy thin-part components and non-thin-wall components. Int. J. Adv. Manufacture Technology, Vol. 84, 2016, Pages 2461–2469.

[8]. X. Zuo, C. Zhang, H. Li, X. Wu, and X. Zhou. Error analysis and compensation in machining thin-walled workpieces based on the inverse reconstruction model. The International Journal of Advanced Manufacturing Technology, Vol. 95, 2018, Pages 2369–2377.

[9]. S. Wimmer and M. F. Zaeh. The Prediction of Surface Error Characteristics in the Peripheral Milling of Thin-Walled Structures. J. of Manufacturing and Materials Processing, Vol. 2, 2018, Pages 1-11.

[10]. J. Fei, B. Lin, J. Xiao, M. Ding, S. Yan, X. Zhang, and J. Zhang. Investigation of moving fixture on deformation suppression during milling process of thin-walled structures. Journal of Manufacturing Processes, Vol. 32, 2018, Pages 403–411.

[11]. J. Shi, Q. Song, Z. Liu, and Y. Wan. Formulating a numerically low-cost method of a constrained layer damper for vibration suppression in thin-walled component milling and experimental validation. International Journal of Mechanical Sciences, Vol. 128-129, 2017, Pages 294–311.

[12]. R. Izamshah R.A, J. P.T Mo, and S. Ding. Finite element analysis of machining thin-wall parts. Key Engineering Material, Vol. 458, 2010, Pages 1-8.

[13]. J. Feng, Z. Sun, Z. Jiang, and L. Yang. Identification of chatter in milling of Ti-6Al-4V titanium alloy thin-walled workpieces based on cutting force signals and surface topography. Int. J. Adv. Manufacture Technology, Vol. 82, 2016, Pages 1909–1920.

[14]. S. Ren, X. Long, and G. Meng. Dynamics and stability of milling thin-walled pocket structure. Journal of Sound and Vibration, Vol. 429, 2018, Pages 325-347.

[15]. Kolluru K, Axinte D. Novel ancillary device for minimizing machining vibrations in thin wall assemblies. Int. J. of Machine Tools & Manufacture 2014, Vol. 85, Pages 79–86.

[16]. J. Shi, Q. Song, Z. Liu, X. Ai. A novel stability prediction approach for thin-walled component milling considering material removing process. Chinese Journal of Aeronautics, Vol. 30(5), 2017, Pages 1789–1798.

[17]. M.R. Khoshdarregi. Mechanics and Dynamics of Multi-Point Threading of Thin-Walled Oil Pipes. Doctoral Thesis. The University of British Columbia. 2017.

[18]. Mitsubishi Materials Corporation. Ultra-High Productivity for Nickel Based Heat Resistant Alloys.

[19]. Mitsubishi Materials Corporation. Aerospace applications. A613G.

[20]. Mitsubishi Materials Corporation. Automotive applications. B248G.

[21]. Altintas Y, Stepan G, Merdol D, Dombovari Z. Chatter stability of milling in frequency and discrete time domain. CIRP Journal of Manufacturing Science and Technology, Vol. 1, 2008, Pages 35–44.

[22]. Comak A, Budak E. Modeling dynamics and stability of variable pitch and helix milling tools for development of a design method to maximize chatter stability. Precision Engineering, Vol. 47, 2017, Pages 459-468.

[23]. E. Govekar, J. Gradisek, I. Grabec. Analysis of acoustic emission signals and monitoring of machining processes. Ultrasonic, Vol. 38, 2000, Pages 598–603.

[24]. H. Li and Y. Chen. Machining Process Monitoring. Springer-Verlag London 2014.

[25]. Kalvoda T, Hwang YR. Analysis of signals for monitoring of nonlinear and non-stationary machining processes. Sensors and Actuators A, Vol. 161, 2010, Pages 39-45.

[26]. Lamraoui M, Thomas M, El Badaoui M. Cyclostationarity approach for monitoring chatter and tool wear in high speed milling. Mechanical Systems and Signal Processing, Vol. 44, 2014, Pages 177-198.

[27]. Kamarthi SV, Pittner S. Fourier and Wavelet transform for flank wear estimation-A comparison. Mechanical Systems and Signal Processing, Vol. 11(6), 1997, Pages 791–809.

[28]. Xu J, Yamada K, Sekiya K, Tanaka R, Yamane Y. Effect of different features to drill-wear prediction with backpropagation neural network. Precision Engineering, Vol. 38, 2014, Pages 791–798.

[29]. Gu S, Ni J, Yuan J. Non-stationary signal analysis and transient machining process condition monitoring. Int. J. of Machine Tools & Manufacture, Vol. 42, 2002, Pages 41–51.

[30]. Cao H, Zhou K, Chen X. Chatter identification in end milling process based on EEMD and nonlinear dimensionless indicators. Int. J. of Machine Tools & Manufacture, Vol. 92, 2015, Pages 52–59.

[31]. Huang N, Shen S. Hilbert-Huang Transform and Its Applications. World Scientific Publishing, USA, 2005.

[32]. Fu Y, Zhang Y, Zhou H, Li D, Liu H, Qiao H, Wang X. Timely online chatter detection in end milling process. Mechanical Systems and Signal Processing, Vol. 75, 2016, Pages 668–688.

[33]. Cheng, G., Cheng Y., Shen, L., Qiu, J., Zhang, S. Gear fault identification based on Hilbert–Huang transform and SOM neural network. Measurement, Vol. 46, 2013, Pages 1137–1146.

[34]. M. Amarnath, I. R. P. Krishna. Local fault detection in helical gears via vibration and acoustic signals using EMD based statistical parameter analysis. Measurement, Vol. 58, 2014, Pages 154–164.

[35]. Lei, Y., He, Z., Zi, Y. Application of the EEMD method to rotor fault diagnosis of rotating machinery. Mechanical Systems and Signal Processing, Vol. 23, 2009, Pages 1327–1338.

[36]. Z. K. Peng, Peter W.Tse, F. L. Chu. A comparison study of improved Hilbert–Huang transform and wavelet transform: Application to fault diagnosis for rolling bearing. Mechanical Systems and Signal Processing, Vol. 19, 2005, Pages 974-988.

[37]. Y. Zhang, B. Tang, and X. Xiao. Time–frequency interpretation of multi-frequency signal from rotating machinery using an improved Hilbert–Huang transform. Measurement, Vol. 82, 2016, Pages 221-239.

[38]. L. Saidi, J. B. Ali, F. Fnaiech. Bi-spectrum based-EMD applied to the non-stationary vibration signals for bearing faults diagnosis. ISA Transactions, Vol. 53, 2014, Pages 1650–1660.

[39]. C. Y. Yang and T. Y. Wu. Diagnostics of gear deterioration using EEMD approach and PCA process. Measurement, Vol. 61, 2015, Pages 75-87.

[40]. Cao H, Lei Y, He Z. Chatter identification in end milling process using wavelet packets and Hilbert–Huang transform. Int. J. of Machine Tools & Manufacture, Vol. 69, 2013, Pages 11–19.

[41]. Kalvoda T, Hwang YR. A cutter tool monitoring in machining process using Hilbert–Huang transform. Int. J. of Machine Tools & Manufacture, Vol. 50, 2010, Pages 495-501.

[42]. Bassiuny AM, Li X. Flute breakage detection during end milling using Hilbert–Huang transform and smoothed nonlinear energy operator. Int. J. of Machine Tools & Manufacture, Vol. 47, 2007, Pages 1011–1020.

[43]. Peng Y. Empirical model decomposition based time-frequency analysis for the effective detection of tool breakage. J. of Manufacturing Science and Engineering, Vol. 128, 2006, Pages 154-166.

[44]. Cao H, Lei Y, He Z. Chatter identification in end milling process using wavelet packets and Hilbert–Huang transform. Int. J. of Machine Tools & Manufacture, Vol. 69, 2013, Pages 11–19.

[45]. H. Q. Liu, Q. H. Chen, B. Li, X. Y. Mao, K. M. Mao, and F. Y. Peng. On-line chatter detection using servo motor current signal in turning. Science China Technological Sciences. Vol. 54, 2011, Pages 3119–3129.

[46]. Elsevier B.V. Scopus® [Database on the Internet]. Available at: http://www.scopus.com.

[47]. F.W. Taylor, On the art of cutting metals, Transactions of ASME 28 (1907) 31–248404.

[48]. R. N. Arnold, The mechanism of tool vibration in the cutting of steel, Proceedings of the Institution of Mechanical Engineers 154 (1946) 261–284.

[49]. F. Koenigsberger J. Tlusty. Machine Tool Structures. Vol. 1. Pergamon. 1970.

[50]. H.E. Meritt, Theory of self-excited machine–tool chatter, Transactions of the ASME Journal of Engineering for Industry 87 (1965) 447–454.

[51]. Schmitz TL, and Smith KS. Mechanical Vibrations: Modeling and Measurement. Springer, New York, 2012.

[52]. G. Quintana and J. Ciurana. Chatter in machining processes: A review. Int. Journal of Machine Tools & Manufacture 51 (2011) 363–376.

[53]. J. Tlusty, “Dynamics of high-speed milling,” J. of Engineering Industry for Trans. of ASME, Vol.108, pp. 59-67, 1986.

[54]. Y. Altintas. Manufacturing Automation: Metal Cutting Mechanics, Machine Tool Vibration, CNC Design. Cambridge University Press. 2012.

[55]. Altintas Y, Budak E. Analytical prediction of stability lobes in Milling. Annals of the CIRP, Vol. 44(1), 1995, Pages 357-362.

[56]. U. Bravo, O. Altuzarra, L. N. L. Lacalle, J. A. Sánchez, and F. J. Campa, “Stability limits of milling considering the flexibility of the workpiece and the machine,” Int. J. of Machine Tools and Manufacture, Vol.45, No.15, pp. 1669-1680, 2005.

[57]. F. J. Campa, L. N. L. Lacalle, and A. Celaya, “Chatter avoidance in the milling of thin floors with bull-nose end mills: Model and stability diagrams,” Int. J. of Machine Tools and Manufacture, Vol.51, No.1, pp. 43-53, 2011.

[58]. S. Alan, E. Budak, and H. N. Ozgüven, “Analytical prediction of part dynamics for machining stability analysis,” Int. J. Automation Technol., Vol.4. No.3, pp. 259-267, 2010.

[59]. Y. Altintas, M. Eynian, H. Onozuka, Identification of dynamic cutting force coefficients and chatter stability with process damping, CIRP Annals—Manufacturing Technology 57 (2008) 371–374.

[60]. Y. Kurata, S.D. Merdol, Y. Altintas, N. Suzuki, E. Shamoto, Chatter stability in turning and milling with in process identified process damping, Journal of Advanced Mechanical Design, Systems, and Manufacturing 4 (2010) 1107–1118.

[61]. L.T. Tunc -, E. Budak, Effect of cutting conditions and tool geometry on process damping in machining, International Journal of Machine Tools and Manufacture 57 (2012) 10–19.

[62]. N. Hanna, S. Tobias, A theory of nonlinear regenerative chatter, ASME Journal of Engineering for Industry 96 (1974) 247–255.

[63]. C.K. Chen, Y.M. Tsao, A stability analysis of turning a tailstock supported flexible work-piece, International Journal of Machine Tools and Manufacture 46 (2006) 18–25.

[64]. C.K. Chen, Y.M. Tsao, A stability analysis of regenerative chatter in turning process without using tailstock, The International Journal of Advanced Manufacturing Technology 29 (2006) 648–654.

[65]. G. L. Huyett. Engineering Handbook: Technical Information. Expressway. Kansas. USA. 2004.

[66]. N. Senthilkumar and T. Tamizharasan. Effect of Tool Geometry in Turning AISI 1045 Steel: Experimental Investigation and FEM Analysis. Arabian Journal for Science and Engineering, Vol. 39, 2014, Pages 4963–4975.

[67]. Starke EA. Jr., Staley JT. Application of modern aluminum alloys to aircraft. Progress of Aerospace Science, Vol. 32, 1996, Pages 131-172.

[68]. Heinz A, Haszler A, Keidel C, Moldenhauer S, Benedictus R, Miller WS. Recent development in aluminum alloys for aerospace applications. Materials Science and Engineering A, Vol. 280, 2000, Pages 102–107.

[69]. Miller WS, Zhuang L, Bottema J, Wittebrood AJ, De Smet P, Haszler A, and Vieregge A. Recent development in aluminum alloys for the automotive industry. Materials Science and Engineering A, Vol. 280, 2000, Pages 37–49.

[70]. Fridlyander IN, Sister VG, Grushko OE, Berstenev VV, Sheveleva LM, and Ivanova LA. Aluminum alloys: Promising materials in the automotive industry. Metal Science and Heat Treatment, Vol. 44(9-10), 2002, Pages 365–370.

[71]. Catalog of Shizuoka ST-NR of 3 axes knee type CNC milling machine.

[72]. Rambabu P, Prasad NE, Wanhill R.J.H. Aerospace materials and material technologies. Springer, 2017.

[73]. Schmitz, T. L., and Smith, K. S. Machining Dynamics: Frequency Response to Improved Productivity. Springer, New York, 2009.

[74]. Jin X, Sun Y, Guo Q, and Guo D. 3D Stability lobe considering the helix angle effect in thin-wall milling. Int. Journal Advance Manufacture Technology, Vol. 82, 2016, Pages 2123–2136.

[75]. G. Quintana and J. Ciurana. Chatter in machining processes: A review. Int. Journal of Machine Tools and Manufacture, Vol. 51, 2011, Pages 363-376.

[76]. T. Childs, K. Maekawa, T. Obikawa, and Y. Yamane. Metal Machining. Elsevier. 2013.

[77]. Wang MY, Chang HY. Experimental study of surface roughness in slot end milling AL2014-T6. Int. Journal of Machine Tools & Manufacture, Vol. 44, 2004, Pages 51–57.

[78]. Dhar NR, Ahmed MT, Islam S. An experimental investigation on effect of minimum quantity lubrication in machining AISI 1040 steel. Int. Journal of Machine Tools & Manufacture, Vol. 47, 2007, Pages 748–753.

[79]. Tsao CC. An experiment study of hard coating and cutting fluid effect in milling aluminum alloy. Int. Journal Advance Manufacture Technology, Vol. 32, 2007, Pages 885–891.

[80]. Zhong W, Zhao D, Wang X. A comparative study on dry milling and little quantity lubricant milling based on vibration signals. Int. Journal of Machine Tools & Manufacture, Vol. 50, 2010, Pages 1057–1064.

ACKNOWLEDGMENTS

I want to first thank to my academic supervisor Prof. Dr. Eng. Keiji Yamada for all of his encouragements, advices, and supports over the past three and half years of doctoral study at the Machining and Machining Systems Laboratory. This work would not be possible without him. He has created an environment in laboratory where everyone feels safe, valued, and motivated.

I also thank to the members of my academic supervisors, Prof. Dr. Eng. Ryutaro Tanaka and Prof. Dr. Eng. Gen Sasaki, for their valuable input in this dissertation.

This research has been partly supported by Prof. Yamada's research members, actually thanks to Mr. Chia-Hung Liu (deputy of Industrial Technology Research Institute, ROC Taiwan) and Mr. Kyosuke Mani for helping me in experimental tests. I thank to Prof. Yean-Rean Hwang (Department of Mechanical Engineering, National Central University, Taiwan) and Prof. Katsuhiko Sekiya for helping me in another technical aspect and also to MEXT-Japan for covering my live expenses during my study.

Last but not least, I am indebted to my family for their unconditional support, for believing in me, and for allowing me to go after my dreams no matter where they take me. Specially thank you to my beloved wife Ismiyati, S.Pd., for her love, kindness, and praying. She has always created joy in my life. And for our three children, just five juz we can teach you. Thank you to my parents, Bpk. Mukani and Ibu Lunawati, Bpk. Abdurahman and Ibu Kolayati, for a childhood which provided the pathway to success. Foremost *Alhamdulillahirobilalamin*.

List of Publications

The following scientific papers have been published as a result of this dissertation:

1. Study of Chatter Characteristics on Thin-Walled Turning. International Conference in 8th Leading Edge Manufacturing 21st century (8th LEM 21), Kyoto Research Park, Kyoto, Japan, October 2015.
   DOI: https://doi.org/10.1299/jsmelem.2015.8._0509-1_

2. Vibration Analysis in Milling of Thin-Walled Workpieces using Hilbert–Huang Transform. International Conference in 9th Leading Edge Manufacturing 21st century (8th LEM 21), Hiroshima Peace Memorial Park, Hiroshima, Japan, September 2017.
   DOI: https://doi.org/10.1299/jsmelem.2017.9.031

3. Application of Hilbert–Huang Transform for Vibration Signal Analysis in End-milling. Precision Engineering, Vol. 53, July 2018, Pages 263-277.
   DOI: https://doi.org/10.1016/j.precisioneng.2018.04.008

4. Milling Process Monitoring Based on Vibration Analysis using Hilbert-Huang Transform. International Journal of Automation Technology. Vol. 12, No. 5, September 5, 2018, Pages 688 – 698.
   DOI: 10.20965/ijat.2018.p0688

Appendix A. Hilbert-Huang Transform

```
%%%%%%%%%%%%%
%This coding is generated for analysis signal obtained in machining using Hilbert-Huang transform.
%Under Prof. Keiji Yamada, Ph.D. in Eng
%Agus Susanto
clear; close all;clc;
pkg load signal
fs=100000.0;        % sampling frequency (samples/second)
Ts=1/fs;            %
N=1200000;           % full sampling point (samples)
NN=N+0;             %
xx=csvread("Acc_&_SG_FullSignal.csv"); % load war data
x=xx(325000:NN-835000,2)*10;     % sampling point (samples) will be analysis (samples)
Ny=length(x)           % data length
t=0:Ts:Ts*(N-1160000);  % time vektor (s)
t11=t*10;
t1=t11';
Nt1=length(t1)

% Plot time domain of raw data
figure(1) % time domain signal
plot(t1,x,'linewidth',1, 'k');
set(gca,'FontName', 'Times New Roman','FontSize',30);
xlabel('Time t (s)'), ylabel('Amplitude a (m/s^2)');
hold on;
stem3_hht(x,Ts);        % Function to perform EMD process. Result is a set IMFs components;
                        % The function as follows;
function stem3_hht(x,Ts)
N = length(x);
c = linspace(0,(N-2)*10*Ts,N-1);
imf = emd(x);
% plots of Set IMF in time-domain.
M = length(imf);
N = length(x);
c = linspace(0,(N-1)*10*Ts,N);   % c = linspace(0,(N-1)*1000*Ts,N);
for k1 = 0:4:M-1
  figure
  for k2 = 1:min(4,M-k1), subplot(4,1,k2), plot(c,1.2*imf{k1+k2}, 'linewidth',3, 'k');
     set(gca,'FontName', 'Times New Roman','FontSize',13,'XLim',[0 4.001]);
```

```
    %set(gca,'FontName', 'Times New Roman','FontSize',30,'XLim',[0 c(end)]);
    %xlabel('Time t (ms)');
    %ylabel({['IMF',num2str(k1+k2)],'Amplitude a (m/s^2)'});
    ylabel({['IMF',num2str(k1+k2)]});
  end
end

emd_power_plot_hht(x,Ts);          % Function to perform Hilbert tranform process. Result is a Hilbert spectrum;
                                   % The function as follows;
function emd_power_plot_hht(x,Ts)
N = length(x);
% c = linspace(0,(N-2)*Ts,N-1);
c = linspace(0,(N-2)*10*Ts,N-1);
imf = emd(x);
% Set time-frequency plots.
for k = 1:length(imf)-1
  b{k} = abs(hilbert(imf{k})).*abs(hilbert(imf{k}));
  b{k} = b{k}(1:N-1);%power
  th{k}= angle(hilbert(imf{k}));
  d{k} = diff(th{k})/Ts/(2*pi);%frequency
end

%find max instant amplitude to make color map
for k = 1:length(imf)-1
  m(k)=max(b{k});
end
  bmax = max(m);
  B    = colormap(jet);
  i    = bmax/63;
for k = 1:length(imf)-1
  bn{k}= round(b{k}/i)+1;%a nunmer of color band
  for a=1:length(b{k})
  cm{a}=B(bn{k}(a),:);
  end

  for n = 1:length(b{k}),
    figure(2)
    plot(c(n),0.1*d{k}(n),'.','color',cm{n},'markersize',10);
    %plot(c(n),d{k}(n),'.','color',cm{n},'markersize',10);
    set(gca,'FontName', 'Times New Roman','FontSize',30,'XLim',[0 c(end)],'YLim',[0 10000]);
    xlabel('Time [s]'), ylabel('Frequency [Hz]');
```

```
     hold on;
   end
end

whitebg([0 0 0.56250])
colormap(jet)
c = colorbar;
ylabel(c,'Energy')
set(gca,'Clim',[0,bmax], 'FontName', 'Times New Roman','FontSize',30);
d=get(c,'position')
d(3)=0.5*d(3)
set(c,'position',d)
```

Appendix B. Experimental modal analysis (EMA)

The dynamic modal parameters, such us; mass *m*, damping *c*, and stiffness *k* of a machine tool structure needs to be measured to predict cutting condition in a well-known as stability lobe diagram. The dynamic modal parameters of machine tool structures are determined from a so-called hammering test.

In hammering test, the machine tool structure is excited by hitting it with an impulse force hammer. This impact will excite the structure over a certain frequency range. The structure will show a response after the impact, which characterizes the dynamics of the structure. This response can then be measured using a displacement sensor, a velocity sensor, or an accelerometer sensor (in our study, we used accelerometer sensor). The dynamic characteristics of the structure are determined by combining the Fourier spectrum of both the impact force measurement and the displacement measurement. When using an accelerometer, the signal needs to be integrated twice in frequency domain, to get the displacement measurement. The combination of these two measurements results is called Frequency Response Function (FRF).

In our study, we considered the workpieces as the flexible part, more flexible than cutting tool because the workpieces were thin-walled structure, for both turning and milling. Therefore, we excited the workpiece using the modal hammer. Please refers Chapter 5 to get experimental method of hammering tests in turning and milling.

To minimize errors during the hammering testing, we always conducted several measurements. After each hitting, we examined the signals to identify whether it was bad or good hitting. A hitting is considered bad if a multiple hitting occurred (the hammer bounces, loses contact and hits the structure again), this phenomenon is called bouncing effect. A bouncing effect can be detected in DL750 Yokogawa oscilloscope or in screen of personal computer which was already installed with Pico Scope oscilloscope. Enough good hits need to be collected and then they will be examined the FRF.

After the hammering test is performed, we analyzed the measured frequency response function. **Figure 1** shows a couple of impact force and time domain data obtained in hammering test of thin-tubular workpieces with wall thickness *h* 3 and 5 mm, respectively. **Figures 1(a)** and **Fig. 1(b)** are a couple of impact force and acceleration response which were measured for thin-tubular workpieces with wall thickness *h* 3 mm. Besides, **Fig. 1(c)** and **Fig. 1(d)** are a couple of impact force and acceleration response which were measured for thin-tubular workpieces with wall thickness *h* 5 mm. As can be seen from impact signal in **Fig. 1,** the black signals are obtained in *x* direction and the red signals are obtained in *y* direction. The impact signals show no second hit, therefore no bouncing effect has occurred, and they will be good hits.

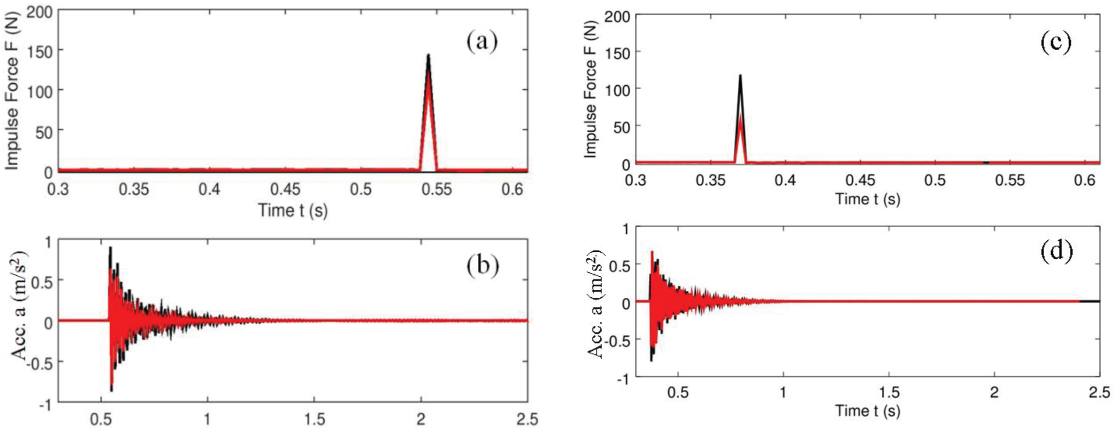

Figure 1. Time domain data of hammering test; (a) and (c) impact forces, and (b) and (d) acceleration responses.

Next step is transformed the time domain data shown in **Fig. 1** to frequency domain using fast Fourier transform (FFT) and the result is shown in **Fig. 2**. **Figure 2(a)** and **Fig. 2(b)** are a couple of frequency spectra of impact force and acceleration response which were obtained by FFT for thin-tubular workpieces with wall thickness *h* 3 mm. Besides, **Fig. 2(c)** and **Fig. 2(d)** are frequency spectra for thin-tubular workpieces with wall thickness *h* 5 mm. The black signals are obtained in *x* direction and the red signals are obtained in *y* direction.

As can be seen from **Fig. 2(b)** and **Fig. 2(d)**, large peaks are at 53, 55, 78, and 84 Hz, respectively. These peaks are natural frequencies of each workpiece. These peaks represent the weakest points of machine tool structure that we observe. Therefore, we should keep these frequencies in mind as a critical location in our analysis.

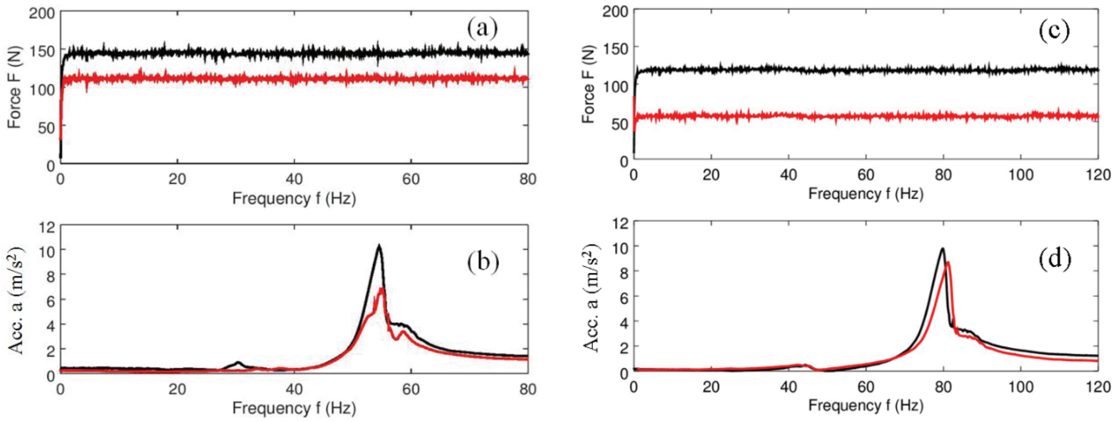

Figure 2. Frequency spectra of hammering test; (a) and (c) impact forces and (b) and (d) acceleration responses which were obtained by FFT.

Following step, we can observe the real & imaginary parts of the FRF of the work-pieces by combining the Fourier spectrum of both the impact force and the displacement and the FRF results are shown in **Fig. 3**. **Figure 3(a)** and **3(b)** show a couple of the real and imaginary parts of FRF for thin-tubular workpiece with wall thickness h 3 mm. Besides, **Fig. 3(c)** and **Fig. 3(d)** are a couple of the real and imaginary parts of FRF for thin-tubular workpieces with wall thickness h 5 mm. The black signals are obtained in x direction and the red signals are obtained in y direction. As can be seen from **Fig. 3(a)** and **Fig. (c)**, they contain two the highest peaks at specific frequencies f_1 and f_2, and f_3 and f_4. Besides, **Fig. 3(b)** and **Fig. 3(d)** contain the negative peak value A and B for each natural frequency f_n. According to these values; f_1, f_2, f_3, f_4, f_n, A and B, the modal parameters can be determined, including modal damping ratio ζ, stiffness k, mass m, and damping coefficient c of the workpiece.

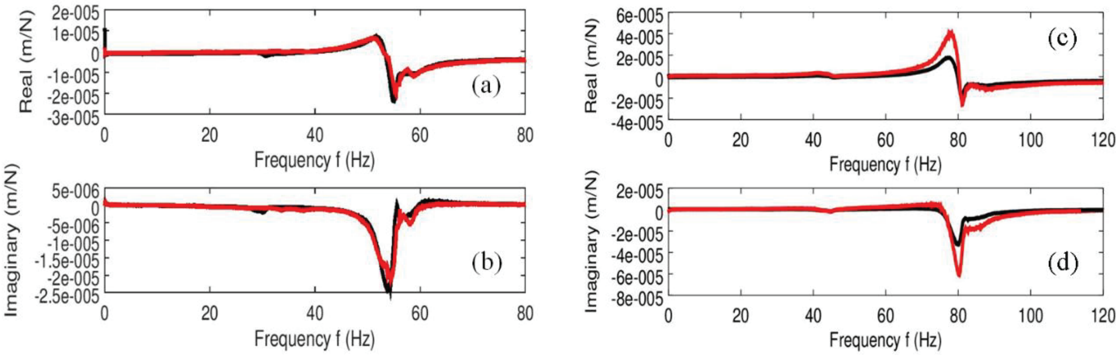

Figure 3. Transfer function; Real-Imaginary parts.

Following, the dynamic modal parameters are determined using some formulas. And these formulas were referred in ref. [51] as follows;

The modal damping ratio ζ can be determined using;

$$\zeta = \frac{f_2 - f_1}{2fn} \tag{1}$$

The negative peak value A in the imaginary part of the FRF is then used to find the modal stiffness value k;

$$k = \frac{-1}{2\zeta A} \tag{2}$$

Next, the modal mass m can be determined using modal stiffness and the natural frequency;

$$m = \frac{k}{f_n^2} \tag{3}$$

The modal damping coefficients c are calculated using the modal damping ratio, stiffness, and mass values as follows;

$$c = 2\zeta\sqrt{km} \tag{4}$$

And the dynamics modal parameters for or thin-walled tubular workpieces are shown in following table and OCTAVE coding for generate EMA is shown in bellow of table.

Table 1. Dynamic modal parameters of thin-turbular workpieces.

Wall thickness t (mm)	FRF Direction	Natural frequency f_n (Hz)	Damping ratio ζ (%)	Stiffness k (N/μm)
3	G_{xx}	55	6.6	0.25
	G_{yy}	53	1.1	0.266
5	G_{xx}	78	5.6	0.355
	G_{yy}	84	1.05	0.28

OCTAVE Coding for Experimental modal analysis (EMA)

```
%%%%%%%%%%%%
%This coding is generated for machine tool structure identification -
%by using experimental modal analysis (EMA).
%Under Prof. Keiji Yamada, Ph.D. in Eng
%Agus Susanto
clear all, clc
close all;
pkg load signal
% Loading the raw data for Gxx
h3xx = csvread('20150305-0001V_01.csv');
h3yy = csvread('20150305-0003H_01.csv');
Colom1xx = h3xx(:,1);     % time (ms)
Colom2xx = h3xx(:,2);     % Impulse force (V)
Colom3xx = h3xx(:,3);     % Acceleration response(V)
% Loading the raw data for Gyy
Colom1yy = h3yy(:,1);     % time (ms)
Colom2yy = h3yy(:,2);     % Impulse force (V)
Colom3yy = h3yy(:,3);     % Acceleration response(V)
% Sensor sensitifity
FSen = 2.3;               % Hammering force sensitifity = 10 mV/lbf = 2.3 mV/N
AccSen = 1;               % Accelerometer sensitifity = 1.0 mV/ms^-2
% Generate a time vector
```

```
N1xx = length(Colom1xx);     % Data length
N2xx = length(Colom2xx);     % Data length
N3xx = length(Colom3xx);     % Data length

N1yy = length(Colom1yy);     % Data length
N2yy = length(Colom2yy);     % Data length
N3yy = length(Colom3yy);     % Data length

t1 = 0:1/180:1/180*(N1xx-1); % Time vector (s)
f1xx = (Colom2xx/FSen);      % Impulse force (N)
a1xx = (Colom3xx/AccSen);    % Acceleration response (m/s^-2)
f1yy = (Colom2yy/FSen);      % Impulse force (N)
a1yy = (Colom3yy/AccSen);    % Acceleration response (m/s^-2)

% Plot impulse force and acceleration response in time domain
figure (1);
subplot(211);
plot(t1, f1xx,'linewidth',2,'k');         % Impulse force
hold on;
plot(t1, f1yy,'linewidth',2,'r');         % Impulse force
%axis([0.0008 0.0031,  -10, 200]);
axis([0.3 0.61,  -3, 200]);
set(gca,'FontSize', 15);
ylabel('Impulse Force F (N)');
xlabel('Time t (s)');
hold on;
subplot(212);
plot(t1, a1xx,'linewidth',2,'k');         % Accelerotion response
hold on;
plot(t1, a1yy,'linewidth',2,'r');         % Accelerotion response
%axis([0.0008, 0.0031,  -1, 1]);
axis([0.3, 2.5,  -1, 1]);
set(gca,'FontSize', 15);
ylabel('Acc. a (m/s^2)');
xlabel('Time t (s)');
% Calculate Fourier transform of impact force and acceleration
fs = 180;
Axx = [0: N2xx-1].*(fs/N2xx);
Bxx = [0: N3xx-1].*(fs/N3xx);
axx = ceil(N2xx/2);
bxx = ceil(N3xx/2);
```

```
Ayy = [0: N2yy-1].*(fs/N2yy);
Byy = [0: N3yy-1].*(fs/N3yy);
ayy = ceil(N2yy/2);
byy = ceil(N3yy/2);

%FFT untuk raw signal
fftf1xx = (fft(f1xx));
ffta1xx = (fft(a1xx));

fftf1yy = (fft(f1yy));
ffta1yy = (fft(a1yy));

% Plot the frequency spectrum for impact force and acceleration
figure (2);
subplot(211);
plot(Axx(1:axx), abs(fftf1xx(1:axx)), 'linewidth',2,'k');
hold on;
plot(Ayy(1:ayy), abs(fftf1yy(1:ayy)), 'linewidth',2,'r');
%axis([0,5000,  0,200]);
axis([0,80,  0,200]);
set(gca,'FontSize', 15);
ylabel('Force F (N)'); xlabel('Frequency f (Hz)');
hold on;

subplot(212);
plot(Bxx(1:bxx), abs(ffta1xx(1:bxx)), 'linewidth',2, 'k');
hold on;
plot(Byy(1:byy), abs(ffta1yy(1:byy)), 'linewidth',2, 'r');
%axis([0,2000,  0,100000]);
axis([0,80,  0,12]);
set(gca,'FontSize', 15);
ylabel('Acc. a (m/s^2)'); xlabel('Frequency f (Hz)');
hold on;

% Transfer function
tfxx = ffta1xx(1:bxx)./fftf1xx(1:axx);
tfyy = ffta1yy(1:byy)./fftf1yy(1:ayy);
Omega = 50;
TFxx = -tfxx/(Omega^2);
TFyy = -tfyy/(Omega^2);

figure (3);
```

```
subplot (311);
plot(Axx(1:axx), abs(TFxx(1:bxx)), 'linewidth',3, 'k');
hold on;
plot(Ayy(1:ayy), abs(TFyy(1:byy)), 'linewidth',3, 'r');
%axis([0,2000,  0,5e-6]);
axis([0,80]);
set(gca,'FontSize', 15);
ylabel('Magnitude (m/N)'); xlabel('Frequency f (Hz)');
hold on;

subplot (312);
plot(Axx(1:axx), real(TFxx(1:axx)), 'linewidth',3, 'k');
hold on;
plot(Ayy(1:ayy), real(TFyy(1:ayy)), 'linewidth',3, 'r');
%axis([0,2000,  -3.5e-6,3.5e-6]);
axis([0,80]);
set(gca,'FontSize', 15);
ylabel('Real (m/N)'); xlabel('Frequency f (Hz)');
%title('Real part of TF');
hold on;

subplot (313);
plot(Axx(1:axx), imag(TFxx(1:axx)), 'linewidth',3, 'k');
hold on;
plot(Ayy(1:ayy), imag(TFyy(1:ayy)), 'linewidth',3, 'r');
%axis([0,2000,  -5e-6,3e-6]);
axis([0,80]);
set(gca,'FontSize', 15);
ylabel('Imaginary (m/N)'); xlabel('Frequency f (Hz)');

% Perfor EMA Gxx
%(1) Calculate damping ratio (zetaxx) and (zetayy)
f2axx = 56;         % Frequency in positif peak of real part (Hz)
f1axx = 49.23;      % Frequency in negative peak of real part (Hz)
fnaxx = 55;         % Natural frequency(Hz)
zetaxx = (f2axx-f1axx)/(2*fnaxx)       % Damping ratio (zetaxx)
%(2) Calculate stiffness (kxx) and (kyy)
Aaxx = -0.000031796;   Aayy = -0.00002386;  % Negative value of imaginary part of FRF
kxx = -1/(2*zetaxx*Aaxx)               % Stiffness (kxx)

% Confirm dynamic modal parameter by EMA with hammering test
w = (0:0.2:4000)'*2*pi;   % frequency, rad/s
```

```
% Dynamic modal parameter obtained by EMA
fnaxx = 55;               % Frequency(Hz)
wnaxx = fnaxx*2*pi;       % Frequency (rad/s)
raxx = w/wnaxx;           % Frequency ratio

% Magnitude of FRF
FRF_magn_xx = 1/kxx*sqrt(1./((1-raxx.^2).^2 + (2*zetaxx*raxx).^2));              % m/N
% Real part of FRF
FRF_real_xx = 1/kxx*(1-raxx.^2)./((1-raxx.^2).^2 + (2*zetaxx*raxx).^2);          % m/N
% Imaginary part of FRF
FRF_imag_xx = 1/kxx*(-2*zetaxx*raxx)./((1-raxx.^2).^2 + (2*zetaxx*raxx).^2);    % m/N

figure (4);
subplot (311);
plot(Axx(1:axx), abs(TFxx(1:bxx)),'k', 'linewidth',3);
hold on;
plot(w/2/pi, FRF_magn_xx, 'b','linewidth',3);
hold on;
axis([0,130,  0,3.5e-5]);
set(gca,'FontSize', 15);
ylabel('Magnitude (m/N)'); xlabel('Frequency f (Hz)');

subplot (312);
plot(Axx(1:axx), real(TFxx(1:axx)), 'k','linewidth',3);
hold on;
plot(w/2/pi, FRF_real_xx-0.5e-5, 'b','linewidth',3);
axis([0,130,  -3e-5,2e-5]);
set(gca,'FontSize', 15);
ylabel('Real (m/N)'); xlabel('Frequency f (Hz)');

subplot (313);
plot(Axx(1:axx), imag(TFxx(1:axx)), 'k', 'linewidth',3);
hold on;
plot(w/2/pi, FRF_imag_xx, 'b','linewidth',3);
axis([0,130,  -3.5e-5,3e-6]);
set(gca,'FontSize', 15);
ylabel('Receptance');
xlabel('Frequency, f, (Hz)');

% Perfor EMA Gyy
%(1) Calculate damping ratio (zetaxx) and (zetayy)
f2ayy = 54;        % Frequency in positif peak of real part (Hz)
```

```
f1ayy = 50.5;      % Frequency in negative peak of real part (Hz)
fnayy = 53;        % Natural frequency(Hz)
zetayy = (f2ayy-f1ayy)/(2*fnayy)      % Damping ratio (zetayy)
%(2) Calculate stiffness (kxx) and (kyy)
Aayy = -0.00002386;                   % Negative value of imaginary part of FRF
kyy = -1/(2*zetayy*Aayy)              % Stiffness (kyy)

% Confirm dynamic modal parameter by EMA with hammering test
w = (0:0.2:4000)'*2*pi;   % frequency, rad/s
% Dynamic modal parameter obtained by EMA
fnayy = 55;              % Frequency(Hz)
wnayy = fnayy*2*pi;      % Frequency (rad/s)
rayy = w/wnayy;          % Frequency ratio
% Magnitude of FRF
FRF_magn_yy = 1/kyy*sqrt(1./((1-rayy.^2).^2 + (2*zetayy*rayy).^2));            % m/N
% Real part of FRF
FRF_real_yy = 1/kyy*(1-rayy.^2)./((1-rayy.^2).^2 + (2*zetayy*rayy).^2);        % m/N
% Imaginary part of FRF
FRF_imag_yy = 1/kyy*(-2*zetayy*rayy)./((1-rayy.^2).^2 + (2*zetayy*rayy).^2);    % m/N

figure (5);
subplot (311);
plot(Ayy(1:ayy), abs(TFyy(1:byy)),'r', 'linewidth',3);
hold on;
plot(w/2/pi, FRF_magn_yy, 'b','linewidth',3);
hold on;
axis([0,130,  0,3.5e-5]);
set(gca,'FontSize', 15);
ylabel('Magnitude (m/N)'); xlabel('Frequency f (Hz)');

subplot (312);
plot(Ayy(1:ayy), real(TFyy(1:ayy)), 'r','linewidth',3);
hold on;
plot(w/2/pi, FRF_real_yy-0.3e-5, 'b','linewidth',3);
axis([0,130,  -3e-5,2e-5]);
set(gca,'FontSize', 15);
ylabel('Real (m/N)'); xlabel('Frequency f (Hz)');

subplot (313);
plot(Ayy(1:ayy), imag(TFyy(1:ayy)), 'r', 'linewidth',3);
hold on;
plot(w/2/pi, FRF_imag_yy, 'b','linewidth',3);
```

```
axis([0,130,  -3.5e-5,3e-6]);

set(gca,'FontSize', 15);

ylabel('Receptance');

xlabel('Frequency f (Hz)');
```